

The Effect of Aluminum Cold Spray Coating
on Corrosion Protection and Corrosion Fatigue
Life Enhancement of Magnesium Alloy,
AZ31B

by

Mohammad Waheeb Diab

A thesis
presented to the University of Waterloo
in fulfillment of the
thesis requirement for the degree of
Master of Applied Science
in
Mechanical Engineering

Waterloo, Ontario, Canada, 2015

© Mohammad Waheeb Diab 2015

AUTHOR'S DECLARATION

I hereby declare that I am the sole author of this thesis. This is a true copy of the thesis, including any required final revisions, as accepted by my examiners.

I understand that my thesis may be made electronically available to the public.

Mohammad Waheeb Diab

Abstract

Magnesium alloys are of a recent interest for the transportation industry due to their excellent properties such as high strength and low density which will save energy and reduce gas emission and it will also improve the vehicle performance. However due to their high chemical activity, magnesium and magnesium alloys have unsatisfactory corrosion resistance and high tendency to corrode in humid and aqueous environments. Although alloying elements provides some improvement in magnesium against corrosion, further protection for these alloys is needed against the corrosion in different corrosive environments. Aluminum powder cold spray is a new coating technology with very promising results in corrosion protection of magnesium alloys. The effect of applying pure aluminum cold spray coating on wrought AZ31B Mg alloy from the corrosion and corrosion fatigue point of view is studied. This research comprises two parts. The first part is studying the corrosion behavior of AZ31B cold spray coated and uncoated coupons by performing an accelerated corrosion testing in a corrosion chamber. The results for both types of coupons have been compared to each other. The second part of this research is to study the fatigue strength by rotating bending machine of stress relieved and stress relieved/coated specimens in salt water environment. S-N curves for the two groups of specimens were plotted. After the analysis and comparison of all the testing results, it was revealed that pure Al cold spray coating considerably improved the corrosion resistance of Mg alloy AZ31B in 5% NaCl fog environment. The microstructural analysis revealed the presence of some secondary phases which act as a cathode and accelerate the corrosion of the anode, Mg alloy. Comparison of corrosion-fatigue S-N curves of stress relieved and stress relieved/coated specimens show fatigue life reduction after cold spray coating to a maximum percentage of 87.6%. The reason for that is the fact that the pure Al powder has much lower ultimate tensile strength than Mg alloy AZ31B. This fact will lead to an earlier crack on the Al coating surface during the fatigue cycles, from which the electrolyte will penetrate to the Mg substrate and cause a localized corrosion and failure.

Acknowledgements

First of all, I thank God for all His blessings and grace.

I would like to express my sincere gratitude to my supervisor Professor Hamid Jahed for his invaluable advice, motivation and patience throughout this research work.

The financial support from my employer SABIC, Saudi Basic Industries Corporation is gratefully acknowledged. I am also grateful to my manager Mr. Ali Al-Hazemi and my mentor Dr. Abdulaziz Al-Meshari for their continuous support.

I would also like to thank my thesis committee members, Professors Carolyn Hansson and Grzegorz Glinka, for their aid in this process. Their input was extremely valuable and very much appreciated.

I appreciate the technical support from Dr. Yuquan Ding, Rick Forgett, Neil Griffett and Richard Gordon.

I am thankful to CanmetMATERIALS research center in particular to my co-supervisor Dr. Xin Pang for her help and technical support, Shi Chao, Jennifer Collier.

I would also like to express my sincere gratitude to CenterLine Ltd. and in particular Dr. Julio Villafuerte, Dr. Jianfeng Wang for providing technical support during this research.

I greatly appreciate my colleagues, Dr. Seyed Behzad Behraves, Elfaitori Ibrahim, Ali Roostaei, Mi Chengji, Bahareh Marzbanrad, Amir Yazdanmehr, Andrew Gryguc, Siavash Borhan Dayani for their precious thoughts and discussions.

Finally, I would like to express my extreme gratitude to my family and my friends for their unwavering support and encouragement through my studies.

*To Waheeb the father, who believed in me,
and to Waheeb the son, in whom I believe,
I dedicate this thesis*

Table of Contents

List of Figures	viii
List of Tables	xii
Chapter 1 Introduction.....	1
1.1 Thesis Motivation.....	2
1.2 Thesis Objectives and Methodology	2
1.3 Thesis Organization.....	2
Chapter 2 Background and Literature Review	4
2.1 Magnesium’s Properties and Characterization	4
2.2 Corrosion of Magnesium	9
2.2.1 Galvanic Corrosion.....	12
2.2.2 Stress Corrosion Cracking	15
2.2.3 Pitting Corrosion	15
2.2.4 Intergranular Corrosion	17
2.2.5 Filiform Corrosion.....	18
2.2.6 Crevice Corrosion.....	19
2.2.7 Fatigue and Corrosion Fatigue	19
2.3 Accelerated Corrosion Testing	26
2.4 Corrosion Protection Methods.....	28
2.4.1 Chemical Conversion Coating.....	28
2.4.2 Electrochemical Plating	29
2.4.3 Plasma Electrolytic Oxidation (PEO).....	30
2.4.4 Cold Spray Coating	31
2.5 Literature Review	34
2.5.1 Corrosion of Mg Alloys.....	34
2.5.2 Corrosion of AZ31B.....	37
2.5.3 Corrosion Fatigue of AZ31B.....	39
2.5.4 Cold Spray of Mg Alloys	42
Chapter 3 Materials and Experimental Methodology.....	46
3.1 Materials.....	46
3.1.1 Cold Spraying of Samples	52
3.2 Testing Equipment and Standards	54

3.2.1 Corrosion Salt Spray (Fog) Test.....	54
3.2.2 Fatigue Rotating Bending Machine.....	60
Chapter 4 Experimental Results and Discussion.....	62
4.1 UW Corrosion Testing Results.....	62
4.1.1 Bare AZ31B Coupons Corrosion Testing	63
.....	67
4.1.2 Al Cold Spray AZ31B Coupons Corrosion Testing.....	67
4.2 CanmetMATERIALS Corrosion Testing Results	72
4.2.1 Bare AZ31B Coupons Corrosion Testing	73
4.2.2 Al Cold Spray AZ31B Coupons Corrosion Testing	82
4.3 Corrosion Fatigue Testing	90
4.3.1 Fracture Surface.....	95
Chapter 5 Conclusion and Recommendations for Future Work.....	101
5.1 Conclusion.....	101
5.2 Recommendations for Future Work	102
Appendix A Coated Coupons' Surface Roughness Measurements.....	103
Bibliography	106

List of Figures

Figure 1.1: Global automotive magnesium alloy consumption, 2008-2015E (E: Estimate).....	1
Figure 2.1: Production supply of magnesium in the world in 2012	4
Figure 2.2: Relation between fuel consumption and vehicle mass.....	8
Figure 2.3: Weight reduction resulted from replacing some automotive components by Mg alloy	9
Figure 2.4: Potential-pH (Pourbaix) diagram for a magnesium-water system at room temperature....	10
Figure 2.5: Schematic diagram of magnesium surface film	11
Figure 2.6: Schematic presentation of typical micro-galvanic corrosion of Mg-Al alloys	14
Figure 2.7: Schematic of typical conditions for stress corrosion cracking.....	15
Figure 2.8: Different forms of pits	16
Figure 2.9: Schematic of pitting corrosion mechanisms for magnesium alloy AM60.....	17
Figure 2.10: Intergranular corrosion morphology of AZ80-T5 in a 3.5% NaCl	18
Figure 2.11: Typical filiform corrosion tracks on steel under a polyurethane coating.....	18
Figure 2.12: Schematic diagram of fatigue-testing with rotating bending	20
Figure 2.13: Schematic of the S-N curves of (a) a material that has an endurance limit and (b) a material that does not have an endurance limit	21
Figure 2.14: Schematic macroscopic surface features, (a) single origin and (b) two origins.....	22
Figure 2.15: Fatigue fracture surface showing two origins with progression beach marks	23
Figure 2.16: Schematic showing beach marks and striation marks.....	23
Figure 2.17: Fatigue fracture surface showing (a) two ratchet marks and multiple origins that result from bending force, and (b) ratchet marks resulting from torsion force	24
Figure 2.18: Schematic showing two different angles for ratchet marks caused by (a) tension or bending (b) torsion	24
Figure 2.19: Schematic showing multiple origins and multiple ratchet marks]	25
Figure 2.20: Steps in the conventional conversion coating process using AZ91D Mg alloy.....	29
Figure 2.21: Example of copper plating on Mg AZ31	30
Figure 2.22: Microstructure of plasma electrolytic oxidation ceramic coating with three layers as (I) loose layer, (II) compact layer and (III) contact layer	31
Figure 2.23: Schematic drawing of a typical cold gas spray apparatus.....	32
Figure 2.24: Scanning electron micrographs of cold sprayed copper particles on a copper substrate (a) an overview and (b) a close-up image.....	33

Figure 2.25: S-N curve for extruded AZ31 alloy in air and 3.5% NaCl.....	39
Figure 2.26: S-N curve for extruded AZ31 and AM50 alloys in air (1), AM50 in 3.5% NaCl (2), AZ31 in 3.5% NaCl (3)	40
Figure 2.27: S-N curve for extruded AZ31 alloy (1) in air, (2) in 3.5% sodium chloride, (3) in 0.1N borate, and (4) 0.1N borate solution saturated with magnesium hydroxide	41
Figure 2.28: Potentiodynamic polarization curves in 3.5 wt.% NaCl solution	43
Figure 2.29: Cyclic polarization curves of cold sprayed pure Al coating and bulk pure Al after 1 h of immersion in a 3.5 wt.% NaCl solution	44
Figure 2.30: (a) Cross-section of pure aluminum coating on an AZ91D substrate, and (b) Scanning electron microscope image taken at the coating's top surface revealing the high level of porosity	45
Figure 3.1: AZ31B extrusion (all dimensions in mm).....	46
Figure 3.2: AZ31B bare coupon with dimensions.....	47
Figure 3.3: AZ31B Al cold spray coated coupon.....	47
Figure 3.4: AZ31B (a) bare coupons and (b) an Al cold spray coated coupon for corrosion testing ...	48
Figure 3.5: Optical microscope image showing the hardness indentations at C, I and B.....	49
Figure 3.6: Optical microscope image showing Al coating interface	50
Figure 3.7: Optical microscope image showing Al coating thickness.....	50
Figure 3.8: Cylindrical specimens used for corrosion fatigue testing: (a) schematic and dimensions (b) bare and (c) Al cold spray coated	51
Figure 3.9: Commercial low-pressure cold spray equipment. Picture courtesy of Supersonic Spray Technologies, a division of CenterLine (Windsor) Ltd.....	52
Figure 3.10: Schematic of the high-pressure cold spray booth used by Supersonic Spray Technologies, a division of CenterLine (Windsor) Ltd	53
Figure 3.11: Morphology of aluminum powder used for the cold spray process.....	53
Figure 3.12: In-house corrosion testing apparatus and setup	54
Figure 3.13: Schematic drawing of the salt fog test chamber used for corrosion testing	55
Figure 3.14: The prepared chemical cleaning solution (a) C.5.1 (b) C.5.2	57
Figure 3.15: Mass losses of corroded specimens resulting from repetitive cleaning cycles	58
Figure 3.16: SJ-400 surface roughness tester setup.....	58
Figure 3.17: AltiSurf® 500 laser profilometer for topographic analysis of samples	59
Figure 3.18: Nanovea 3D Imaging equipment	59

Figure 3.19: R.R. Moore Rotational Beam Fatigue Testing Machine: (a) bearing housing, (b) weight pan, and (c) loading harness	61
Figure 3.20: Setup for the corrosion fatigue testing	61
Figure 4.1: Coupons edges protected with silicon resin	62
Figure 4.2: Bare AZ31B coupons before and after 15 days of salt spray exposure: (a) before testing,	63
Figure 4.3: Average weight loss versus the number of tested cycles	64
Figure 4.4: Average roughness measurements versus the number of tested cycles	64
Figure 4.5: Typical sizes of the pits in bare coupons after: (a) 6 cycles, (b) 9 cycles, (c) 12 cycles, and (d) 15 cycles in bare and coated coupons	65
Figure 4.6: Average pit diameter versus the number of tested cycles for bare and coated coupons ...	66
Figure 4.7: Example of surface analysis by Nanovea 3D Imaging showing a pit in a bare coupon ...	66
Figure 4.8: Average pit depth versus the number of tested cycles for bare and coated coupons	67
Figure 4.9 Coated coupons before and after 15 days of salt spray exposure: (a) before testing, (b) after 3 cycles, (c) after 6 cycles, (d) after 9 cycles, (e) after 12 cycles, and (f) after 15 cycles	68
Figure 4.10: Average weight loss versus the number of tested cycles for coated coupons.....	69
Figure 4.11: Average roughness measurements versus the number of tested cycles for coated coupons	69
Figure 4.12: Typical sizes of the pits in coated coupons after: (a) 9 cycles, (b) 9 cycles, (c) 12 cycles, and (d) 15 cycles.....	70
Figure 4.13: Average pits size versus the number of tested cycles	71
Figure 4.14: Average pit depth versus the number of tested cycles for coated coupons.....	71
Figure 4.15: The testing coupons (coated and uncoated) distributed in the rack before testing.....	72
Figure 4.16: The applied mask used for protecting the edges of coated coupons	73
Figure 4.17: Uncoated coupons exposed to 5% salt spray after: (a) 4 cycles, (b) 6 cycles, (c) 8 cycles, (d) 11 cycles, (e) 14 cycles, (f) 17 cycles, (g) 20 cycles, (h) 23 cycles, (i) 26 cycles, and (j) 33 cycles	75
Figure 4.18: Average weight loss versus the number of tested cycles for bare AZ31B coupons	76
Figure 4.19: Corrosion products accumulated on a bare coupon after 6 days of testing	77
Figure 4.20: Optical cross section micrographs showing the microstructure of AZ31B as (a) coated coupon after 11 cycles of corrosion testing, (b) uncoated coupon after 8 cycles of corrosion testing, (c) coated alloy before corrosion testing, and (d) uncoated alloy	79
Figure 4.21: SEM image showing the distributions of particles	80

Figure 4.22: Energy dispersive X-ray analysis of the detected particles as (a) Mg-Al-Mn secondary phase, and (b) Al-Mn secondary phase	80
Figure 4.23: Schematic of the role of the β -phase on corrosion: (a) initial surface and.....	81
Figure 4.24: Coated coupons exposed to 5% salt spray after: (a) 4 cycles, (b) 8 cycles, (c) 11 cycles, (d) 14 cycles, (e) 17 cycles, (f) 20 cycles, (g) 23 cycles, (h) 26 cycles, (i) 33 cycles, (j) 40 cycles, (k) 60 cycles, (l) 90 cycles	84
Figure 4.25: Corrosion products accumulated on a coated coupon after 8 days of testing	85
Figure 4.26: Coated coupon after cleaning/removing edges corrosion products, 40 days of testing ...	85
Figure 4.27: Average weight loss versus the number of tested cycles for coated coupons.....	86
Figure 4.28: Average weight loss versus the number of tested cycles for bare and coated coupons ...	87
Figure 4.29: Surface roughness analysis of coated AZ31B coupons performed by AltiSurf® 500 showing (a) roughness parameters and (b) surface 3D image	88
Figure 4.30: Percentage change of coated coupons surface roughness after corrosion testing	89
Figure 4.31: S-N curves of RBM testing for coated and uncoated specimens under NaCl environment	91
Figure 4.32: S-N curves of RBM testing for coated and uncoated specimens in air.....	92
Figure 4.33: Cracking of Al cold spray coating on the surface at a stress of 60 MPa.....	94
Figure 4.34: Cracking of Al cold spray coating at a stress of 80 MPa.....	94
Figure 4.35: Fracture surfaces of round specimens under different types of loading	95
Figure 4.36: Fracture surfaces of bare sample at a stress of 74 MPa showing: (a) overall fracture surface, (b) initiation with crack, and (c) brittle final fracture.....	96
Figure 4.37: Fracture surfaces of bare sample at a stress of 40 MPa showing: (a) overall fracture surface, (b) mixed mode final fracture, and (c) initiation areas	97
Figure 4.38: Fracture surfaces of a coated sample at a stress of 80 MPa showing: (a) overall fracture surface, (b) initiation with coating crack, and (c) mixed mode final fracture	98
Figure 4.39: Fracture surfaces of a coated sample at a stress of 50 MPa showing: (a) overall fracture surface, (b) brittle final fracture, and (c) initiation area	99

List of Tables

Table 2.1: Most common magnesium alloys, their chemical compositions, uses and properties	6
Table 2.2: Physical properties of magnesium alloy AZ31B.....	7
Table 2.3: Galvanic series in seawater	13
Table 2.4: Summary of the cyclic accelerated corrosion tests that commonly used in automotive industry.....	27
Table 3.1: Chemical composition of the extruded AZ31B (wt.%).....	47
Table 3.2: Micro-indentation Vickers hardness test results at 100 gr.	49
Table 3.3: Chemical cleaning approaches suitable for magnesium and its alloys.....	57
Table 4.1: Uncoated coupons corrosion testing analysis.....	76
Table 4.2: Coated coupons corrosion testing results	86
Table 4.3: Coated coupons' surface roughness analysis	89
Table 4.4: RBM corrosion fatigue testing results in 3.5% NaCl solution	91
Table 4.5: RBM fatigue testing results for AZ31B in air.....	92
Table 4.6: X-ray diffraction results on cylindrical specimens in air	93
Table 4.7: Percentage decrease in the fatigue life after cold spray	95

Chapter 1

Introduction

The low density of magnesium (Mg) and its alloys, 1.74 g/cm^3 – two-thirds that of aluminum (Al) and one-fourth that of iron (Fe) [1]– as well as their other excellent properties such as high strength-to-weight ratio make them attractive candidates for research and development for many different applications. Some of the properties for which Mg and its alloys stand out include their light mass when compared with steel or Al alloys, high specific strength, high thermal conductivity and strong electromagnetic interference resistance. The most prolific users of Mg and its alloys are industries in which strength and weight are very important to their applications mainly in automotive, aerospace, computer and cellular phone industries. Reducing the weight of vehicles is one of the main objectives for the automobile industry; reduced weight results in fewer greenhouse gas emissions, and improved vehicle performance and fuel efficiency. Figure 1.1 shows the growth in the global automotive Mg alloy consumption from 2008 to 2015.

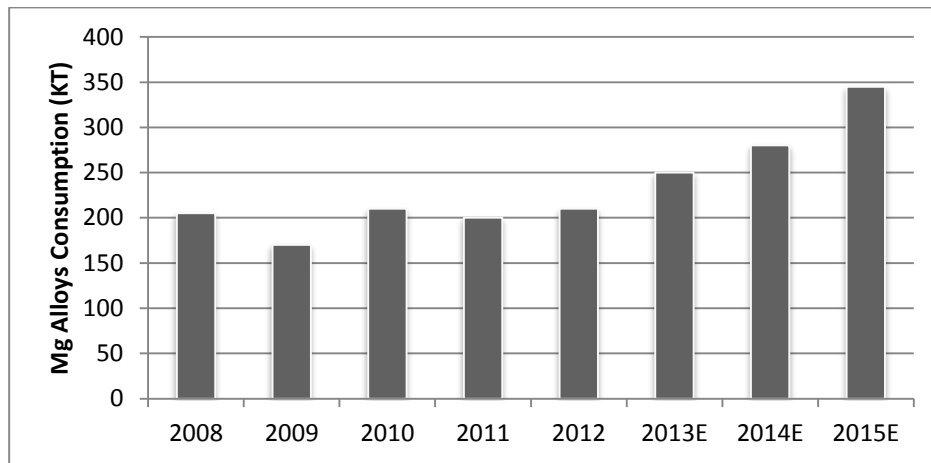


Figure 1.1: Global automotive magnesium alloy consumption, 2008-2015E (E: Estimate) [2]

However, the usage of Mg and its alloys in structural manufacture is still not as popular as other alloys (e.g., Al), despite all of their attractive properties. The reason is that Mg has an unsatisfactory corrosion resistance, resulting from the fact that Mg is one of the most electrochemically reactive materials and is therefore susceptible to corrosion in humid and aqueous environments. For this reason, the applications for Mg and its alloys are considered to be limited [3]-[7]. The protection of Mg structural components from corrosion is essential. Among the protection methods and techniques available [8]-[10], Al powder cold spray is a rather new coating technology, which is a low temperature

process that shows promising results in corrosion protection. In addition, since Mg alloys are often used in structural and mechanical components that are subjected to cyclic loads in different environments and conditions, studying their corrosion fatigue in those different environments is considered to be another important direction for research [11].

1.1 Thesis Motivation

The motivation behind this research is to answer one question: Can cold spray technology be used to provide corrosion protection and enhance the fatigue life of Mg alloys in automotive service environments?

1.2 Thesis Objectives and Methodology

The main objective of this research was to study the effectiveness of cold spray coating on the corrosion protection and the enhancement of fatigue life of wrought Mg alloys. For this, corrosion and corrosion fatigue testing of wrought AZ31B Mg alloy with and without Al cold spray coating was undertaken.

The specific plan to accomplish this objective is summarized in the following steps:

- I. Perform accelerated corrosion testing, based on ASTM B117 salt spray (fog) standard [12], on bare and Al coated AZ31B Mg alloy coupons, in addition to the necessary pre- and post-testing preparations, examinations and analyses, in order to identify the corrosion behavior for both coupons.
- II. Establish the comparative corrosion performance of coated and uncoated AZ31B Mg alloy.
- III. Perform corrosion fatigue testing, using a Rotating Bending Machine (RBM) with a specially designed integrated corrosion chamber, to obtain the S-N curves for bare and Al coated AZ31B Mg alloy cylindrical specimens, in addition to the necessary pre- and post-testing preparations, examinations and analyses to identify the corrosion fatigue behavior for both specimens.
- IV. Quantify the corrosion fatigue results of coated and uncoated AZ31B Mg alloy and establish its comparative corrosion fatigue performance.

1.3 Thesis Organization

This thesis is comprised of five chapters. The current chapter presents the introduction, motivation, objectives, scope and methodology of the research. Chapter 2 provides background information on Mg and Mg alloys, their properties and characterization, the corrosion of Mg, cold spray technology and

corrosion fatigue. This is followed by a literature review on the corrosion of Mg and AZ31B Mg alloy, the corrosion fatigue of AZ31B Mg alloy, and cold spraying of Mg alloys. Chapter 3 defines the materials used in the study including the AZ31B Mg alloy, and cold spray coating powder and parameters. This is followed by a brief introduction to the corrosion testing chambers, the corrosion fatigue testing equipment including the integration of an environmental chamber into the fatigue tester, and the standards and methodology used in this study for quantifying and analyzing the corrosion and corrosion fatigue. Chapter 4 presents the test results and discussion. The following topics will be discussed in detail in this chapter: forms of corrosion, corrosion products and their effects on decelerating the corrosion rate, the role of edges in corrosion initiation and progress, corrosion mechanisms in coated specimens, the role of corrosion pits in impeding crack initiation in uncoated samples, crevice corrosion effects in corrosion fatigue, the formation of multiple cracks, the role of the loading frequency in corrosion fatigue, and corrosion fatigue fracture mechanisms in coated samples. Chapter 5 includes the conclusion of this work and provides recommendations for future work.

Chapter 2

Background and Literature Review

The word ‘Magnesium’ has its roots in the place name of ‘Magnesia’ which is a region of eastern Thessaly in Greece [13]. It was first extracted by Humphrey Davy in 1808. Davy's first name suggestion was ‘magnium’, but it later became ‘magnesium’ [14]. Mg was used widely during World Wars I and II; the US, Britain, France, Canada and Russia started producing Mg for flares and tracer bullets as well as for some niche applications in the nuclear industry. However, while it was being widely used, the worldwide production of Mg dropped off during the World Wars period. After 1945, production efforts were renewed and in 2006, worldwide Mg production reached 726.000 metric tons [15]. Currently, China is the main supplier of Mg to the world as shown in Figure 2.1.

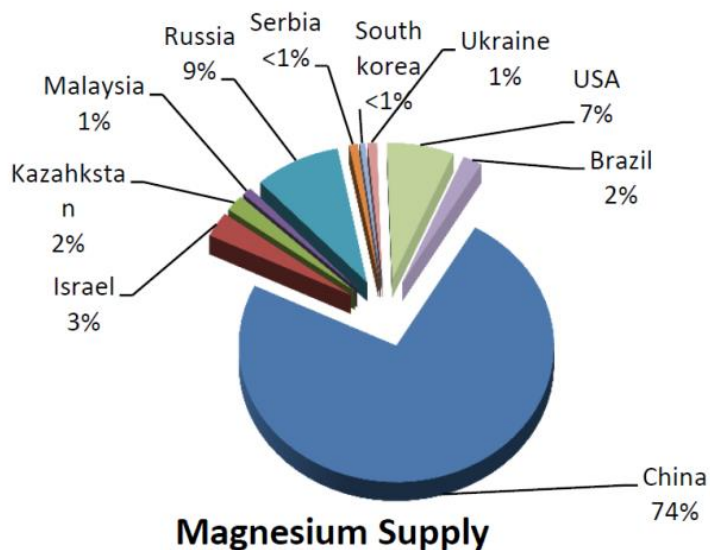


Figure 2.1: Production supply of magnesium in the world in 2012 [15]

2.1 Magnesium's Properties and Characterization

Mg is one of the most ubiquitous elements in the earth; by weight it makes up approximately 1.93% of the mass of the earth's crust and around 0.13% of the mass of the oceans [1]. Mg is plentiful in seawater; it has been reported that each cubic mile of seawater contains around 6 million tons of Mg [16].

The crystal structure of Mg is hexagonal-close-packed (HCP), which leads its specific and complicated mechanical properties. HCP has fewer slip systems as compared to other crystal structures such as face centered cubic crystals (FCC), this fact will results in limited cold workability of the alloy [3].

It is rare for Mg to be used as a pure metal without being alloyed with elements which will enhance its mechanical and metallurgical properties, including improving the corrosion resistance of the Mg [14]. Based on the American Society for Testing Materials (ASTM) standards, it is easy to identify the added alloy elements and their quantity just by looking to the reference name. For example, the Mg alloy AZ31 has around 3% Al and 1% zinc (Zn). Additional letters may be added at the end to indicate more information about the alloying element (e.g., descriptors of the details and stages of development). For room temperature applications, Mg-Al-Zn alloys which frequently also contain manganese (Mn) are used. The Mg-Zn-Zr alloys include the addition of zirconium (Zr), thorium and cerium, and are used for elevated temperature applications.

Nowadays, Mg alloys are used for a wide variety of applications; from computer cases and bicycle frames, to structural components in the aerospace and automotive industries. Automobile parts made from Mg include steering wheels, steering column parts, instrument panels, seats, gear boxes, air intake systems, stretchers, gearbox housing, and tank covers. It is expected that in the future, Mg alloys will be used to construct some larger body parts such as cylinder blocks, petrol tank covers, doors and window frames. Mg alloy AZ91 is considered to be the most common Mg alloy used in Mg-related applications [16].

Mg alloys can be divided into cast alloys, which are produced by casting (die or sand), and wrought alloys, which are produced by hot working (mainly by extrusion, rolling and press forging at temperatures in the range of 300–500 °C. The majority of Mg products and components are formed by the die casting method since Mg has very good castability. However, the conventional pouring method results in the appearance of oxides and dross due to the reactive nature of Mg and, therefore, the squeeze casting technique has been used to deliver better quality castings (e.g., with AZ91) [17].

Wrought alloys are preferred for use in the automotive and aerospace industries as they have better strength and are lighter weight than casting alloys. Table 2.1 shows the most common Mg alloys and their chemical compositions, uses and basic properties.

Table 2.1: Most common magnesium alloys, their chemical compositions, uses and properties [18]

Alloy	Alloying additives	Basic properties and applications
AZ91	9.0%Al, 0.7%Zn, 0.13%Mn	Good castability, good mechanical properties at T<150°C
AM60	6.0%Al, 0.15%Mn	Greater toughness and ductility than AZ91, Slightly lower strength. Often preferred for automotive structural applications.
AM50	Mg-Al system	Good strength, ductility, energy absorption properties and castability
AE44	Mg-Al rare earth system	Better creep behavior and castability than AE42
AE42	Mg-4 atomic percent Al-2 atomic percent rare earths	Low castability, good creep behavior
AS41	4.2%Al, 1.0%Si	Better creep resistance than AZ91 at elevated temperature but lower strength
ZE41	4.2%Zn, 1.2%RE, 0.7%Zr	Rare earth addition improves creep strength at elevated temperature
AZ31	3.0%Al, 1.0Zn, 0.2%Mn	Good extrusion alloy
AM20	Mg-Al system	High ductility, toughness, poor die-castability
MRI 153M	Mg-Al-Ca-Sr system	For high temperature application up to 150°C
MRI 230D	Mg-Al-Ca-Sr system	For high temperature application up to 190°C
AS21	Mg-Al-Si system	For use at temperature in excess of 120°C
AJ62	Mg-Al-Sr system	Good thermal and mechanical strength, castability, corrosion resistance and creep behavior

As does each metal or alloy, Mg and Mg alloys have unique and outstanding properties relative to other engineering materials that make them attractive for use in applications in which those features make a great deal of difference. The following are the most important properties of Mg alloys:

- Lowest density of all commercially available metallic constructional materials.
- Mg has a very light specific gravity.
- High specific strength.
- Great damping capability.
- Good castability, machinability and weldability.
- Non-magnetic.

- Acceptable heat conductivity.
- Readily available.
- Resistant to ageing.
- Good electrical and thermal conductivity.
- Recyclable.

However, there are also some undesirable features in Mg and Mg alloys that limit the usage of these metals including:

- Poor corrosion resistance behavior with a high corrosion rate in service conditions that involve environmental exposure.
- Low modulus of elasticity.
- Limited cold workability and toughness.
- Limited high strength and poor wear and creep resistance at elevated temperatures [19]-[21].

Mg AZ31B possess a good combination of strength, workability and corrosion resistance, suitable for manufacturing of automotive components. Mechanical properties of (the alloy of interest in this study) are tabulated in Table 2.2

Table 2.2: Physical properties of magnesium alloy AZ31B [15]

Crystal structure	Ultimate Tensile strength (Mpa)	Yield Strength (Mpa)	Elastic modulus (Gpa)
HCP	260	200	44.8

In the past, Steel, Aluminium and plastic are known to be the most used materials in the auto industry. But in recent years and with global trends that left the automotive industry with no choice but to produce a new and safe light material that is more environmentally friendly. The reason behind this trend is that reducing the weight will saves energy and also reduces gas emissions since the CO₂ emission has a direct relation to fuel consumption and it is known that by reducing the automotive weights by a certain amount, similar percentage of improvement in fuel economy is resulted as seen in Figure 2.2 below.

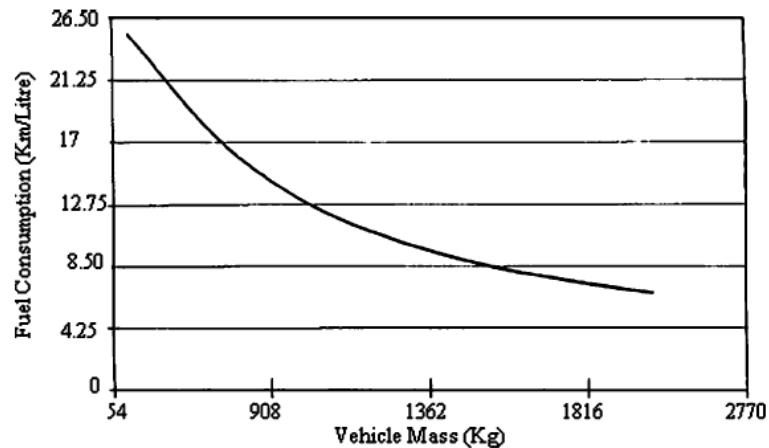


Figure 2.2: Relation between fuel consumption and vehicle mass [18]

Since then, a lot of researches and developments in auto manufactures companies occurred focusing on weight reduction and energy saving. High-strength steels, aluminum, and polymers are already being used to reduce weight significantly, but it was found that additional reductions could be accomplished by increase the implementation of the low-density Mg and its alloys [18],[22].

In the past and until 2004, Mg sheet was expensive. However, the development of new production technologies and procedure, such as twin-roll casting and extruded sheet resulted in a significant decrease in the production cost and brought the price of the Mg sheet to an acceptable level for the automotive industry. Nowadays, the price of Mg metal is more expensive than earlier which could be attributed to the high demand for Mg especially in automotive industries.

Today's application of Mg sheet in the automotive industry is well-known. A typical example is the composite Mg-aluminium alloy engine manufactured by BMW and known as the R6. This engine is considered to be the lightest 3.0 litre, 6-cylinder gasoline engine in the world. Another example is that Audi reported that they reduced the engine weight of V8 Quattro model by 5 kg compared to other 8-cylinder Audi by utilizing Mg components. Porsche Panamera window frame, Lincoln MKT tailgate, Mercedes E-class tailgate, inner panel in Cadillac STS, all these are examples of implementing Mg alloys in auto industry. It was reported that Mg alloys have better noise and vibration dampening characteristics than aluminium [18],[23].

Figure 2.3 below gives an idea for some parts in a vehicle with the potential replacement of Steel and Aluminum by Mg alloys and their impact on the weight reduction. It was reported that by replacing

some steel and aluminum parts with Mg alloys mainly from three major areas like body, power train and chassis components, the weight reduction will be 20-70% [18].

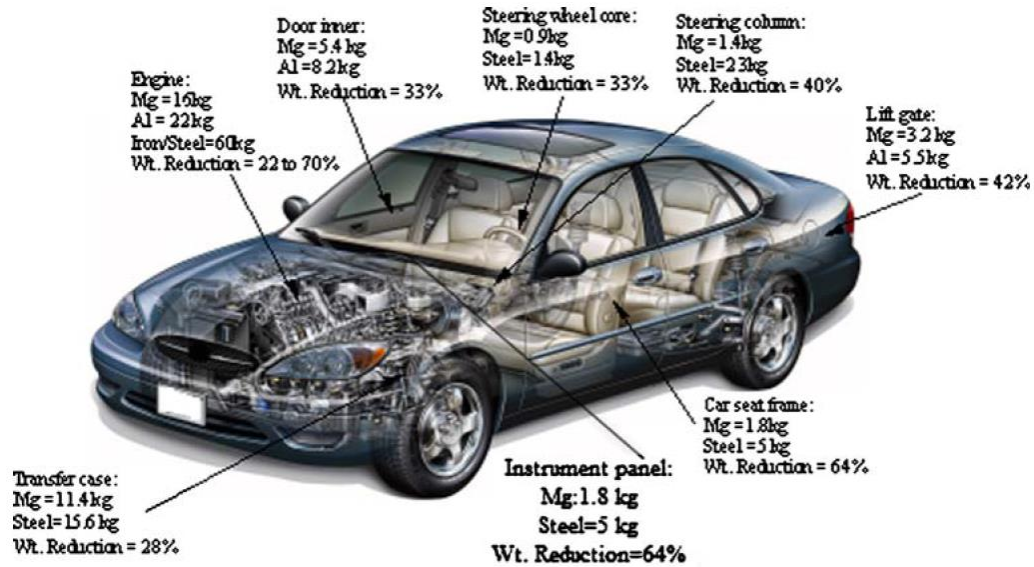


Figure 2.3: Weight reduction resulted from replacing some automotive components by Mg alloy [18]

2.2 Corrosion of Magnesium

The poor corrosion resistance of Mg and its alloys has been a major obstacle to their widespread use in structural applications, despite their other excellent properties. Corrosion of metals can be defined as the destruction or deterioration of a material due to their direct reaction with the environment [24]. Mg is considered to be the most active metal used in engineering applications. Many studies have been carried out to explore the issue of Mg and Mg alloy corrosion and to develop solutions to improve their corrosion resistance [25]-[31]. It was concluded that the corrosion of Mg and its alloys is unique from an electrochemical point of view. For this reason, understanding Mg's thermodynamics, the stability of Mg in different environments, and the critical electrochemical reactions that can occur to Mg are of great importance [32].



The negative standard Gibbs free energy change (ΔG°) of Mg oxidation reactions given above indicates that Mg has a strong tendency to transform into its oxidized states (i.e., corrosion products) [32]. In pure water, Mg is considered unstable and various reactions may occur. Several different pourbaix diagrams (E -pH) have been reported, the E -pH diagram shown in Figure 2.4 below is an integration of the previously reported pourbaix diagrams [32].

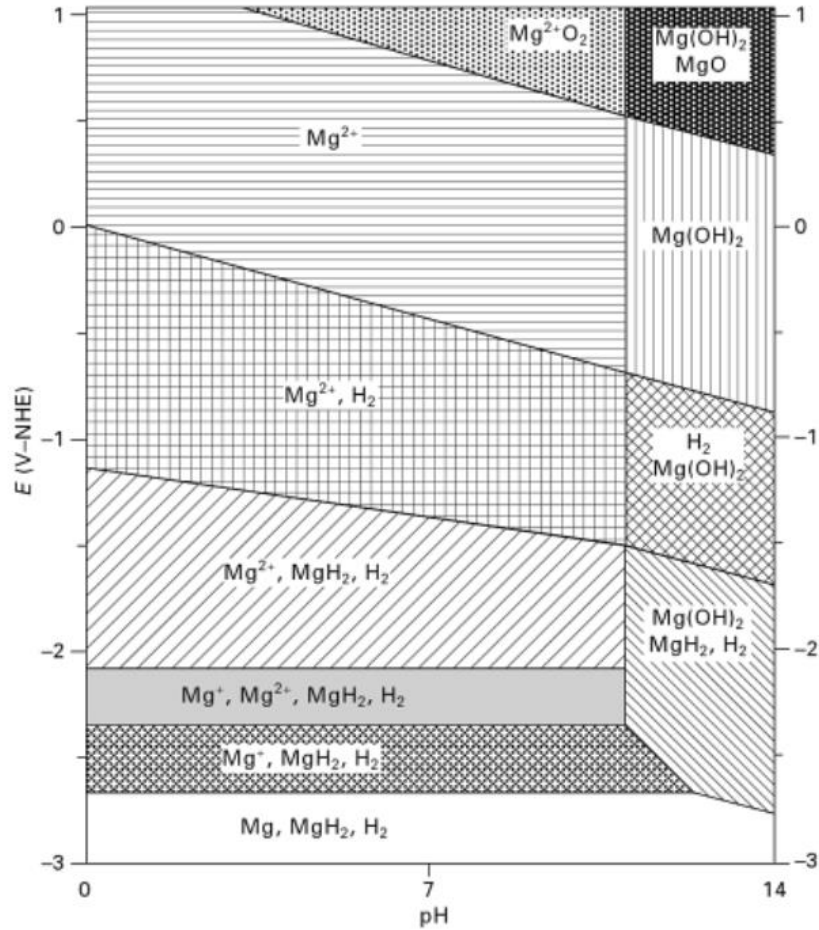


Figure 2.4: Potential-pH (Pourbaix) diagram for a magnesium-water system at room temperature [32]

The diagram clearly shows that Mg moves toward oxidization in most of the E -pH diagram regions. However, this diagram is showing the ranges of corrosion and passivation for Mg assuming the exposure is to pure water. In real life, the water that Mg would be exposed to is not pure and may contain aggressive species that could affect the actual corrosion regions in the E -pH diagram [32]. The immunity regions at Mg, MgH₂ and H₂ are below -2.7 V SHE, significantly below the region of water stability between (0.00 and 1.23) – (0.059pH) V. This also indicates the strong tendency of Mg to

corrode. An oxide MgO or hydroxide Mg(OH)_2 surface film usually forms on Mg substrate. The Mg(OH)_2 surface film is more stable than the MgO film in aqueous solutions [32]. The latter film is known to be porous and does not provide the required protection for the Mg from corrosion attack [25]. MgO is usually formed on the Mg substrate surface when it is exposed to the air, but after exposure to an aqueous solution, most of this MgO will be replaced by Mg(OH)_2 as seen in Figure 2.5.

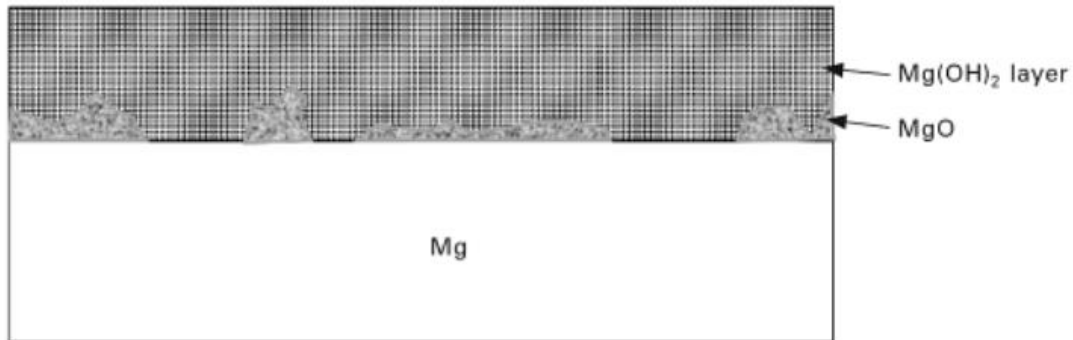
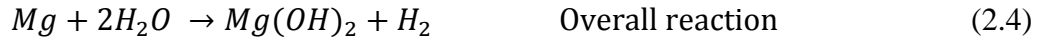


Figure 2.5: Schematic diagram of magnesium surface film [32]

The corrosion process in an aqueous solution can be increased rapidly by the presence of chloride ions in the solution. The Mg(OH)_2 layer is normally porous and loose which will not provide the Mg substrate with the necessary protection. Once the surface film is broken, the corrosion attack will proceed from the weakest areas and it has been reported that repairing this broken film area is not an easy process for Mg [32].

There are also some metallurgical factors that influence the corrosion behavior of Mg . Impurities, and alloying Mg with particular elements, can alter the corrosion resistance of Mg and/or strengthen the surface protective film layer depending on the alloying elements' composition and structure [27],[32]. The presence of phases in some Mg alloys is also an important factor. For example, AZ91 has a large amount of β -phase, $\text{Mg}_{17}\text{Al}_{12}$ precipitated along the grain boundaries due to the high percentage of Al in the alloy. This β -phase is normally passive and acts as a cathode with respect to the Mg substrate (which acts as an anode) [27]. The anodic, cathodic and overall reactions associated with the corrosion of Mg in aqueous environments at neutral pH can be expressed as follows [27]:




Since Mg and Mg alloys may be subjected to different environments, and suffer the effects of air pollutions, there are many types of corrosion that can cause a breakdown of the passive film and degradation of the metal through chemical reactions with the surrounding environment. Because Mg and its alloys are known to be very sensitive to impurities and do not form stable passive films, the majority of corrosion attacks take place in environments with a pH below 11 [26]. The following are the major types of corrosion to which Mg alloys are most susceptible.

2.2.1 .Galvanic Corrosion

Also called dissimilar metal corrosion or contact corrosion. Galvanic corrosion can be defined as the corrosion damage that takes place when two materials with dissimilar potentials are coupled in a corrosive electrolyte. Four elements are required in order for the chemical reaction to take place: an anode (corroded metal), a cathode (protected metal), direct electrical contact and an electrolyte between the anode and the cathode to allow for the movements of ions [24]. Mg and Mg alloys are highly susceptible to galvanic corrosion and it is a major concern in industrial design and material selection. Mg has a normal electrode potential of -2.3 V at 24°C, assuming that the hydrogen electrode potential is zero. This fact places Mg at the bottom of the electrochemical series as a very active metal as shown in Table 2.3 [25]. For example, when attaching a noble material such as passive stainless steel (which works as an efficient cathode), with active Mg alloys (anode), severe galvanic corrosion will occur in the Mg. In contrast, if Mg alloys are attached with more active potential materials such as Al, Zn or cadmium, the consequences will be much less damaging. Another scenario for the galvanic corrosion of Mg alloys known as micro-galvanic coupling involves certain impurities or inner secondary phases. For instance, intermetallic compounds such as β phase $Mg_{17}Al_{12}$ especially in Mg-Al alloys may cause micro-galvanic corrosion between the α -Mg matrix and β - $Mg_{17}Al_{12}$, in which case the β phase acts as the cathode and the surrounding Mg matrix as the anode as seen in Figure 2.6 [16].

Table 2.3: Galvanic series in seawater [25]

Galvanic Series in Seawater		
Material	Steady State Electrode Potential, Volts (Saturated Calomel Half-Cell)	Cathode (Most Noble)
Graphite	+0.25	
Platinum	+0.15	
Zirconium	-0.04	
Type 316 Stainless Steel (Passive)	-0.05	
Type 304 Stainless Steel (Passive)	-0.08	
Monel 400	-0.08	
Hastelloy C	-0.08	
Titanium	-0.1	
Silver	-0.13	
Type 410 Stainless Steel (Passive)	-0.15	
Type 316 Stainless Steel (Active)	-0.18	
Nickel	-0.2	
Type 430 Stainless Steel (Passive)	-0.22	
Copper Alloy 715 (70-30 Cupro-Nickel)	-0.25	
Copper Alloy 706 (90-10 Cupro-Nickel)	-0.28	
Copper Alloy 443 (Admiralty Brass)	-0.29	
G Bronze	-0.31	
Copper Alloy 687 (Aluminum Brass)	-0.32	
Copper	-0.36	
Alloy 464 (Naval Rolled Brass)	-0.4	
Type 410 Stainless Steel (Active)	-0.52	
Type 304 Stainless Steel (Active)	-0.53	
Type 430 Stainless Steel (Active)	-0.57	
Carbon Steel	-0.61	
Cast Iron	-0.61	
Aluminum 3003-H	-0.79	
Zinc	-1.03	
Magnesium	-1.63	

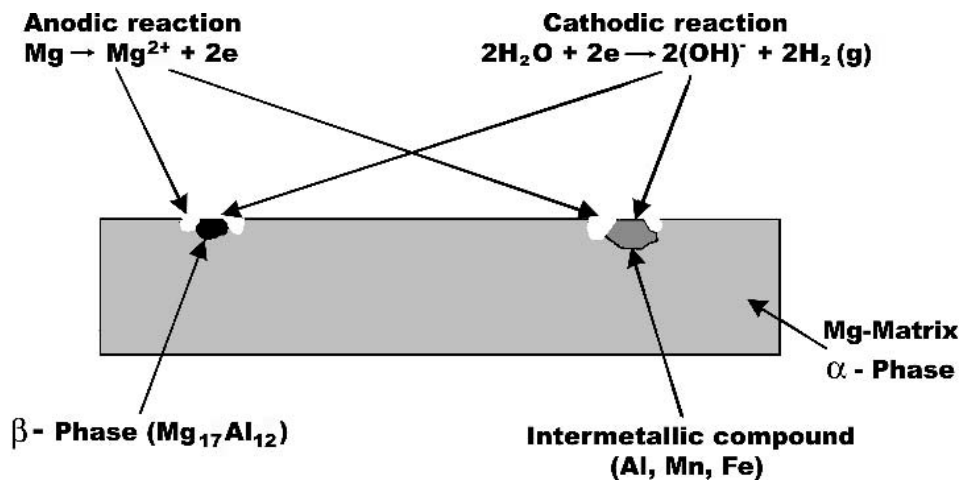


Figure 2.6: Schematic presentation of typical micro-galvanic corrosion of Mg-Al alloys [16]

There are various methods that can be followed to protect Mg and Mg alloys from galvanic corrosion such as:

1. Minimizing the chemical potential difference between dissimilar materials through proper materials selection in the design stage.
2. Applying selective coatings.
3. Using insulation materials between the dissimilar metals [26],[27] ,[33].

And to reduce the risk of the micro-galvanic corrosion, modifying the microstructure of the alloy is needed through:

1. Heat treatments.
2. Modifying casting process.
3. Adding some elements to the alloy or reducing the percentage of some elements as Al in Mg-Al alloys [34]-[36].

2.2.2 Stress Corrosion Cracking

Stress corrosion cracking (SCC) is considered one of the most dangerous types of corrosion [31]. It is defined as the cracking induced from the combined influence of long term tensile stress (above a critical level), susceptible alloys and a corrosive environment as illustrated in Figure 2.7 [24].

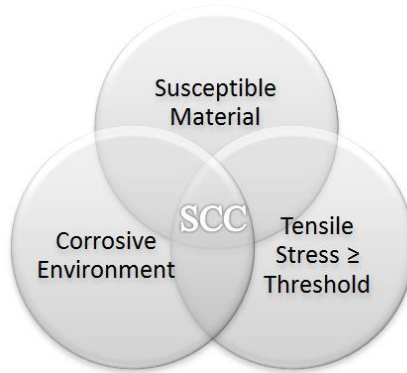


Figure 2.7: Schematic of typical conditions for stress corrosion cracking [24]

SCC can be propagated in a transgranular (TGSCC) or intergranular (IGSCC), but the transgranular mode occurs more often. The intergranular mode may occur due to the precipitation of $Mg_{17}Al_{12}$ in the Mg-Al-Zn group of alloys [27],[33]. Pure Mg is resistant to SCC in atmospheric and aqueous environments. On the other hand, Mg alloys are susceptible to SCC especially the wrought alloys [28]. Alloying Mg with Al and Zn elements encourage SCC and as the percentage of Al in an alloy increases, the tendency for SCC increases as well [27],[31]. For example Mg alloys such as AZ91, AZ80 and AZ61 show a high susceptibility to SCC as the percentages of Al are high at 9%, 8% and 6%, respectively. AZ31 is another example of Mg alloy but it shows a good resistance to SCC as the percentage of Al is only 3%. Alloys containing Zr are another group of SCC resistant Mg alloys, if the applied stresses remain below the yield stress. Also it has been proven that adding Mn to Mg alloys will improve their resistance to SCC. SCC of Mg alloys can take place in alkaline media ($pH > 10.2$), or in fluoride containing solutions [31],[33],[37].

2.2.3 Pitting Corrosion

Pitting corrosion is form of localized corrosion in which the attack on the surface appears as small holes or spots referred to as pits [24]. This type of corrosion is considered to be dangerous because it is a kind

of failure that is very difficult to detect, predict or design against and pits can initiate, propagate and perforate without obvious signs because the corrosion products often cover the pits. The pits can take a variety of different shapes as shown in Figure 2.8.

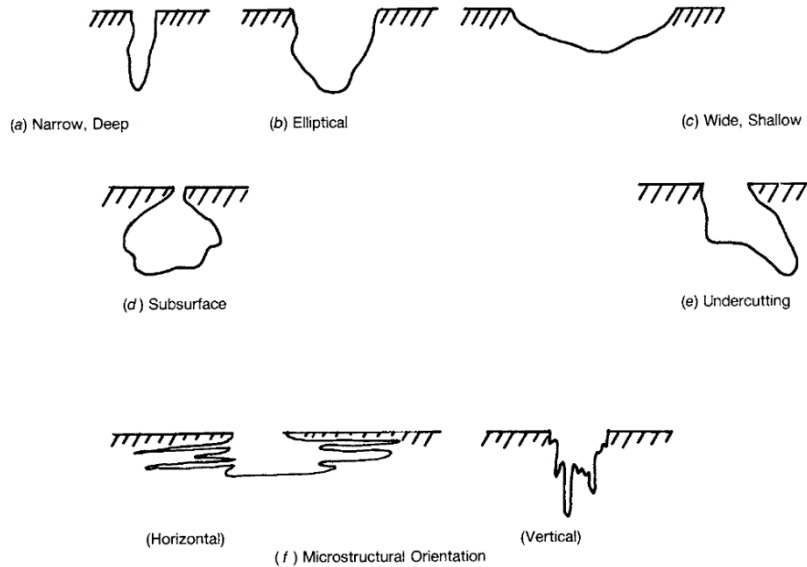


Figure 2.8: Different forms of pits [38]

In nature, Mg is a passive metal which allows the occurrence of pitting corrosion at its free corrosion potential by providing a high potential to cause the current to flow into the pit in neutral or alkaline salt solutions or non-oxidizing media [16]. Pitting is normally associated with stagnant condition which means that increasing the flow velocity decreases the pitting attack. Corrosion pits are usually initiated at the interface with the secondary phase particles, such as $Mg_{17}Al_{12}$, due to the breakdown of the passivity. Then, an electrolytic cell will be formed and the second phase will act as a cathode while the surrounding Mg matrix is the corroded anode [26],[31]. The process of pitting corrosion consists of two stages: initiation and growth. Figure 2.9 below is a schematic of the pitting corrosion mechanisms for Mg alloy AM60 immersed in 3.5% NaCl aqueous solution [31]. In air and before immersion, the alloy surface is covered by an oxide surface film which will be broken after the immersion due to the presence of the chloride ions in the solution. Absorption of the chloride ions on the α -phase area around the secondary phase particles β takes place and this result in the dissolution of the anodic α -phase against the cathodic β -phase. A pit is then initiated and with time the corrosion will proceed until a hemispherical corrosion pit is formed which then spreads over the surface [31].

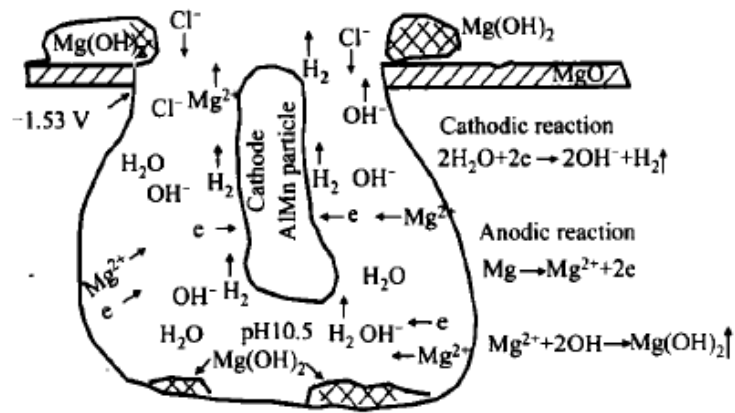


Figure 2.9: Schematic of pitting corrosion mechanisms for magnesium alloy AM60 [31]

2.2.4 Intergranular Corrosion

Intergranular corrosion is a localized attack that takes place along the grain boundaries, or immediately adjacent to grain boundaries, due to the precipitation of the secondary phase while the bulk of the grains remains unaffected [31]. In the case of Mg and Mg alloys, it is still being debated whether they are susceptible to intergranular corrosion or not. But most researchers have claimed that Mg and its alloys are immune to intergranular corrosion. They argue that the grain boundary phase acts as a cathode to the grains itself and the corrosion tends to be concentrated near the grain boundary which may cause grains to be undercut or fall out. This form of attack can have the appearance of intergranular corrosion because it follows a grain boundary path [26],[27],[31]. In contrast, recent studies claim to have proven that Mg and Mg alloys can undergo intergranular corrosion. Figure 2.10 below is a micrograph of an attack that occurred at grain boundaries and claimed to be intergranular corrosion morphology of AZ80-T5 in a 3.5% NaCl aqueous solution after 1 hour immersion.

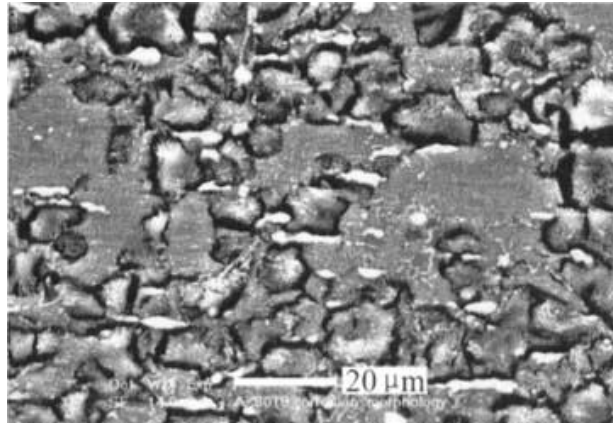


Figure 2.10: Intergranular corrosion morphology of AZ80-T5 in a 3.5% NaCl [31]

2.2.5 Filiform Corrosion

Filiform corrosion is a type of localized corrosion that usually occurs under a coating of steel, Al or Mg. It does not occur on bare and pure Mg. The corrosion products result from bulging in the coating and the attack, which usually looks like filaments (Figure 2.11), proceeds from the points that no longer have coating [31],[39].

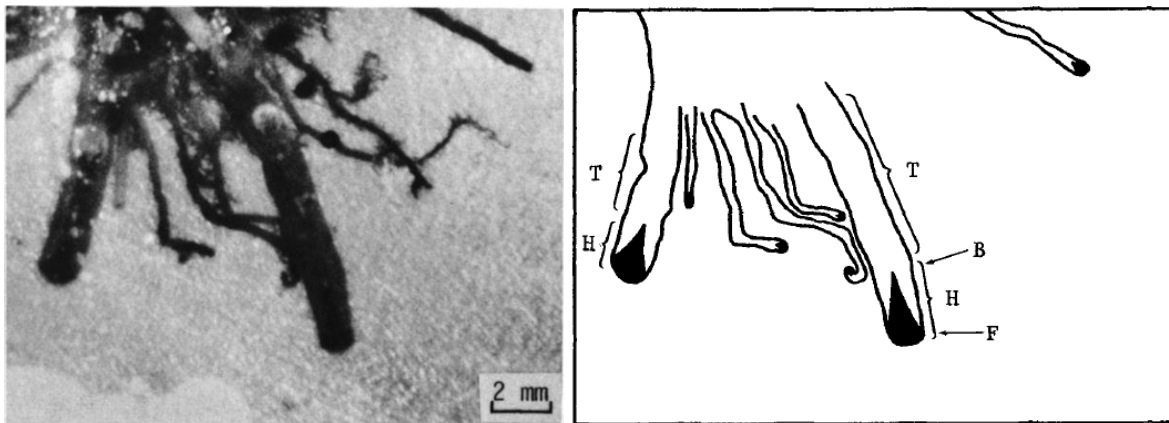


Figure 2.11: Typical filiform corrosion tracks on steel under a polyurethane coating [39]

The filament head in filiform corrosion is normally cathode while the tail is anode [39]. Some studies have reported that the filiform corrosion of Mg is caused by the difference in the oxygen concentration between the anode and the cathode on the substrate. Although filiform corrosion does not occur on

uncoated pure Mg, it can occur on uncoated AZ91 and AZ31 alloys [16],[31]. Filiform corrosion can be minimized by:

1. Applying a multilayer coating.
2. Using a chromate conversion coating on Al.
3. Using a zinc coating on steel.
4. Reducing the relative humidity to the lowest possible when storing items made of susceptible alloys

2.2.6 Crevice Corrosion

Crevice corrosion is a localized form of attack that occurs due to the presence of a stagnant solution located where oxygen cannot reach. This kind of attack is usually found under seals, washers or flanges and becomes aggressive in the presence of chloride ions [24]. For Mg, it has been reported that crevice corrosion does not really occur because Mg corrosion is relatively insensitive to oxygen concentration differences. There is a form of attack that takes place in narrow gaps and looks like a crevice corrosion attack but it is not, however, as the corrosion observed in this attack is caused by the preservation of unevaporated moisture within the crevice. With time, corrosion of the metal in that narrow area will occur [16],[26].

2.2.7 Fatigue and Corrosion Fatigue

The discovery of fatigue occurred in the 1800s when investigators in Europe observed that some structures like bridges and railroad components were cracking when subjected to repeated loading [40]. Fatigue damage is the largest cause of failure in metals, which is catastrophic and can occur very suddenly without warning. The term “fatigue” is used because this type of failure normally occurs after a lengthy period in materials or structures that are subjected to repeated cycles or fluctuating loading at stress levels considerably lower than their tensile or yield strength. The yield strength or yield point of a material is defined as the stress at which a material begins to deform plastically; prior to the yield point the material will deform elastically and will return to its original shape when the applied stress is removed [40]. There are three common ways in which stresses may be applied: axial (tensile-compression), torsional (twisting) or flexural (bending). Fatigue failure is brittle like in nature, even in normally ductile metals, and there is very little plastic deformation associated with it. Rather, the failure

occurs due to the loading conditions, specimen geometry, environmental conditions, microstructure or some combination of these variables [24].

There are three basic factors necessary to cause fatigue: (1) a maximum stress, (2) applying stress in a fluctuating manner, and (3) a large number of cycles. The fluctuating stresses could be fully reversed stress cycles in which the maximum and minimum stresses are equal and are symmetrical about a mean of zero (commonly used during testing). Another type of stress cycle involves both stresses (cyclic and applied) being either in tensile (greater than zero) or in compression (less than zero) and their values are not necessarily equal. Random or irregular stress cycles are another way of applying stress in which random loads and frequencies are applied to the tested object [24],[40].

The fatigue properties of any material can be studied by performing fatigue testing after carefully determining the fatigue test properties. A rotating bending machine is usually used for this testing in which compression and tensile loading are applied to the tested specimen while rotating at adjusted frequency speeds (Figure 2.12). Tension-compression stress cycle testing can also be applied to determine a material's fatigue properties [24].

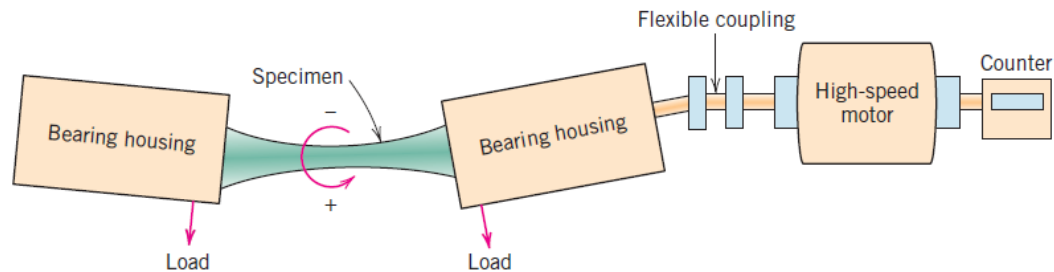


Figure 2.12: Schematic diagram of fatigue-testing with rotating bending [24]

The resulting number of cycles to failure for a specific material under a specific amount of stress will be shown on the counter and is used to plot the S-N curve. "S-N" means stress versus cycles to failure, and is displayed with the stress amplitude on the vertical axis and the logarithm of the number of cycles to failure on the horizontal axis. There are two types of S-N curves based on the behavior of the material: ferrous materials (iron based) usually reach a level of stress above which that material will not fail (the endurance limit) and the S-N curve proceeds as a horizontal line (Figure 2.13a), nonferrous material such as Al, Cu and Mg do not have an endurance limit and the fatigue will be represented by fatigue strength where the material will fail at some point and the S-N curve trend will continue downward (Figure 2.13b).

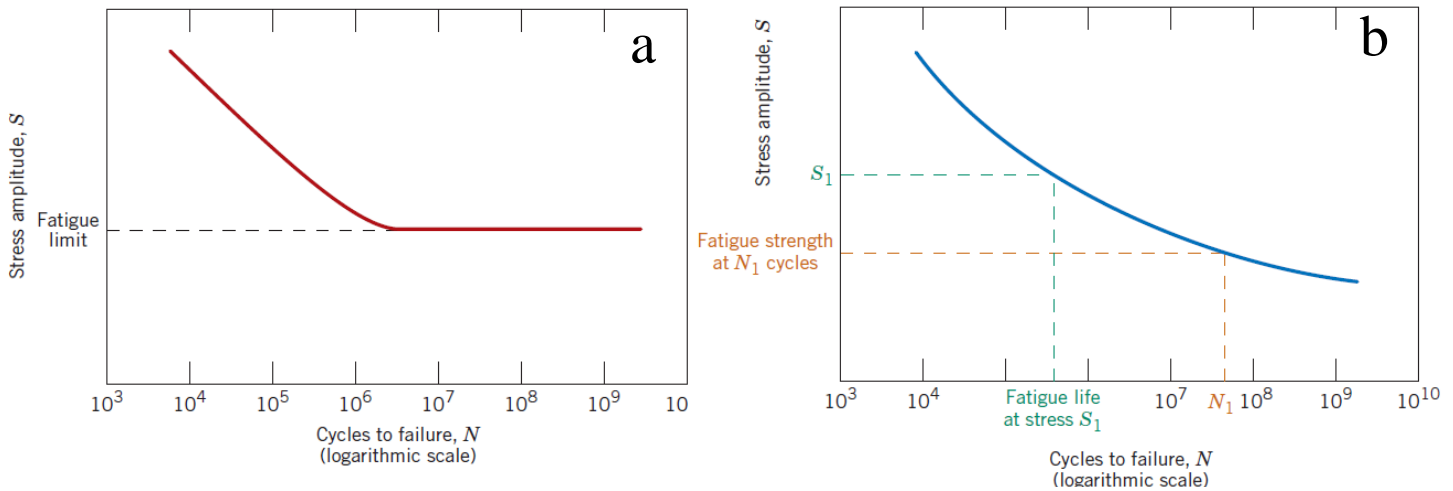


Figure 2.13: Schematic of the S-N curves of (a) a material that has an endurance limit and (b) a material that does not have an endurance limit [24]

The term corrosion fatigue refers to the process that causes metal fractures due to the combined influence of cyclic stresses (fatigue) and the corrosion environment [33]. Corrosion fatigue failure depends on three basic conditions occurring: loading, a corrosive environment and a susceptible material. The fatigue process is caused by the rupturing of the protective passive film, followed by corrosion acceleration due to the metal being exposed to a corrosive environment. The failure will take place at even lower loads and after a shorter period of time if the material is not in dry air. The terms fatigue and corrosion fatigue are similar in many aspects including method of initiation, mode of failure and methods of prevention. The corrosion fatigue failure scenario can be summarized into three stages [40],[41]:

- I. Crack Initiation: usually the failure starts from cracks that initiate from corrosion pits after a large number of loading cycles.
- II. Crack Propagation: the initiated crack will grow due to the applied stresses and the corrosive environment.
- III. Failure: final fracture occurs suddenly after a large number of cycles when the material cannot resist the applied stress.

After failure, studying the fracture surface is essential as it provides a lot of information about the causes of the failure and the time it takes the material to proceed from crack initiation to the final fracture. It will also provide information about the type and direction of forces applied to the failed

part. Fatigue fractographic features can be seen at both macro-scale and micro-scale. Macro-scale fractography refers to features or marks on the fracture surface that can be observed and measured by the naked eye, while micro-scale fractography refers to features or marks on the fracture surface that can only be observed and measured by using special microscopic equipment such as an optical microscope or a scanning electron microscope [40],[42]. The most important features that can be detected from a fracture surface include:

Failure origin or fracture initiation sites are usually located near or at the surface edges. The origin of the failure can be viewed in macro-scale, and it could be a single origin point indicating that the failure had occurred with low overstress, or multiple reversed origins (two ways) which could result from high stress or high stress concentration (Figure 2.14). Micro-scale initiation sites usually include small cleavage cracks, some porosity and other imperfection that can initiate the crack such as nicks, machining marks or corrosion pits that work as stress risers [40],[43].

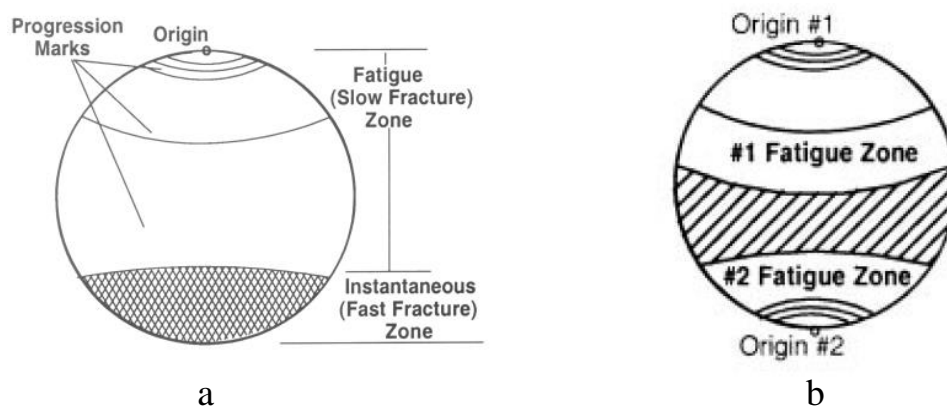


Figure 2.14: Schematic macroscopic surface features, (a) single origin and (b) two origins [43]

- **Final fracture**, or the overload zone or overstress zone as it is also known, is simply the area where the final fracture takes place. This zone or area is usually seen macroscopically as brittle but sometimes a small amount of ductility could exist. From this zone, we can find out about the load applied when the final fracture happened. For example, if the overload zone is large this indicates that the part went through a high amount of stress during the final fracture. The overload zone's roughness depends directly on the strength of the material; the roughness increases as the strength of the material used increases [40],[43].

- **Progression marks** are usually recognized in macro-scale and give a lot of information about crack growth. These marks only exist in fractures with variations in the applied stress. The common name for these marks is ‘beach marks’; the name capturing their similar appearance to lines in the sand on a beach (Figure 2.15). Progression marks are usually generated in one of two ways, by a change in the loading or frequency, or by a change in stress amplitude (e.g., start-up and shutdown forces) [40],[43].

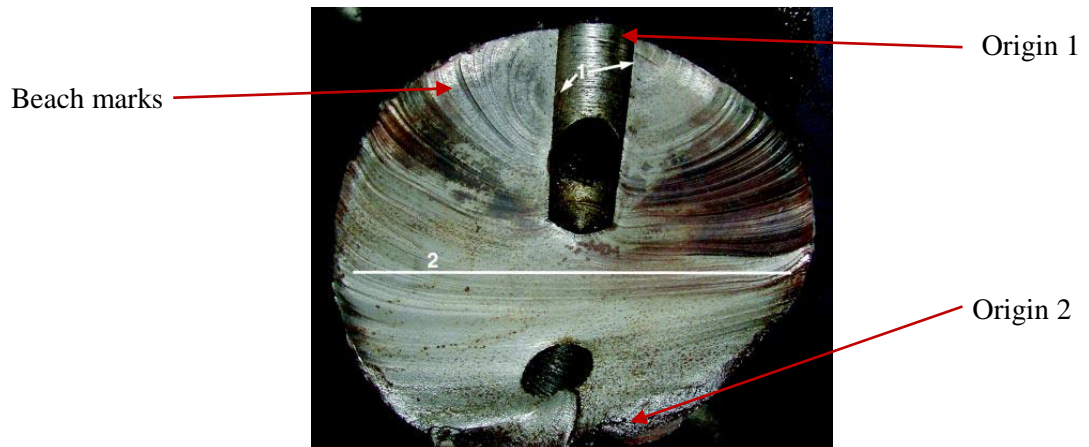


Figure 2.15: Fatigue fracture surface showing two origins with progression beach marks [43]

Beach marks should be distinguished from fatigue striations which look similar. The difference is that fatigue striations indicate each stress cycle practiced by the part and they can only be seen using a very high magnification level; beach marks can be seen by naked eye [43] (Figure 2.16).

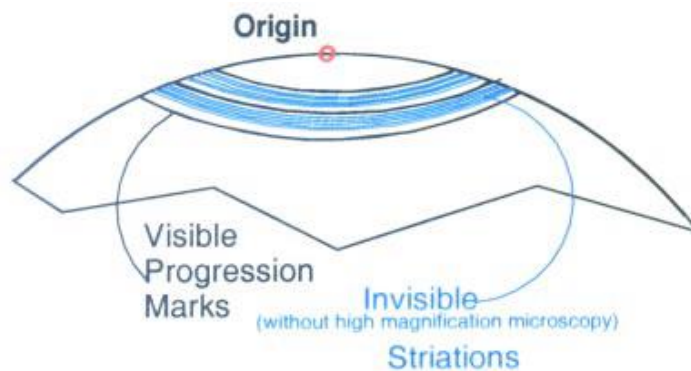


Figure 2.16: Schematic showing beach marks and striation marks [43]

- **Ratchet marks** are the borders between two adjacent failure planes. The existence of these marks points to multiple origins. Figure 2.17 shows ratchet marks that separate the two origin cracks. Valuable

information can be generated simply by studying the ratchet marks and the size of the fracture zone [43]. For example, it would be easy determine the major cause of the fracture, whether it was the load or the stress concentration. If there were many ratchet marks and a small overload zone, this would indicate failure under a light load and a high stress concentration.

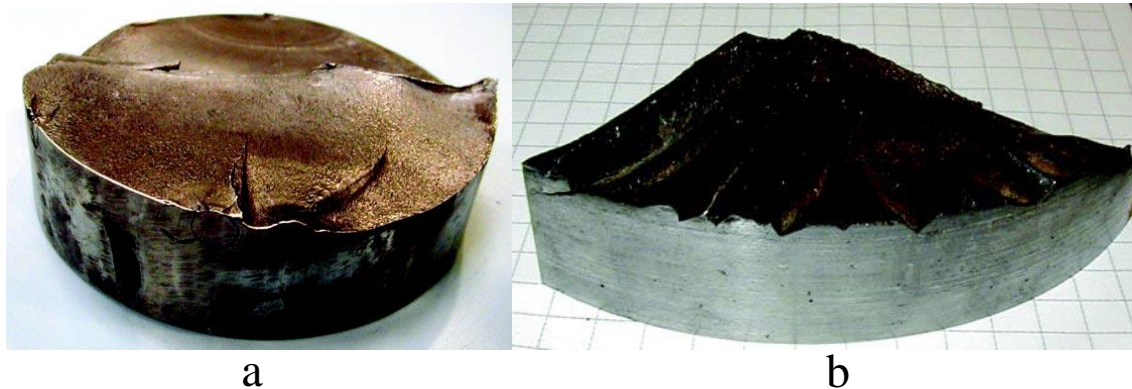


Figure 2.17: Fatigue fracture surface showing (a) two ratchet marks and multiple origins that result from bending force, and (b) ratchet marks resulting from torsion force [43]

The ratchet mark edges indicate whether torsional forces were involved with the failure. Figure 2.18 shows two examples, one of which shows ratchet marks perpendicular to the fracture face indicating that bending or tension caused the failure, and one with tapering ratchet marks indicating that the primary load causing the failure was torsional.

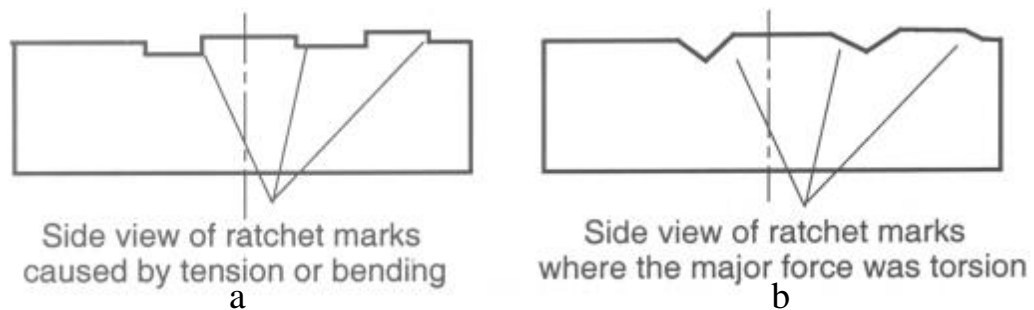


Figure 2.18: Schematic showing two different angles for ratchet marks caused by (a) tension or bending (b) torsion [43]

In the case of multiple origins being found on a fracture surface, by analyzing the ratchet mark angles it can be ascertained which origin is the primary one. For example, in Figure 2.19, since the middle two

ratchet marks are somewhat closer at the surface, it could be concluded that the failure began between them [40],[43].

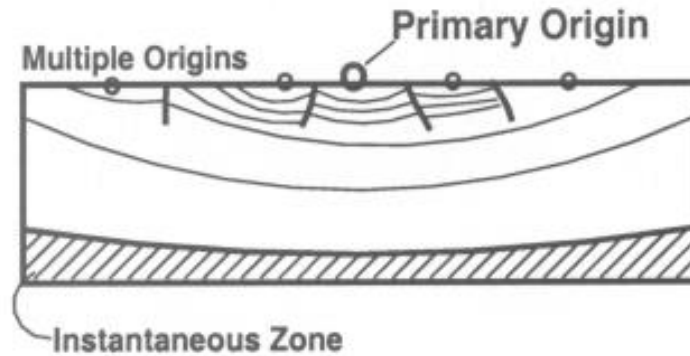


Figure 2.19: Schematic showing multiple origins and multiple ratchet marks [43]

Although corrosion fatigue failure can have heavy and costly consequences in maintenance and equipment, it can be controlled if new designs and procedures take into consideration the factors that may influence fatigue life. The following are the most effective approaches to reducing the risk of corrosion fatigue in any type of material:

- I. Protecting the material from the corrosive environment by using coatings and/or inhibitors.
- II. Using more corrosion resistant materials which have a better fatigue life.
- III. Insuring good design that helps to minimize the stress concentration of components that are in cyclic service.
- IV. Eliminating or reducing stress raisers such as notches and sharp filler by streamlining the part.
- V. Removing grinding marks, nicks and gouges if possible on the surface of components.
- VI. Ensuring good fit up and smooth transitions for welds, and minimizing weld defects.
- VII. Performing a periodic inspection to the part for any sign of cracks and replacing the part once a crack exceeds a critical length.
- VIII. FEA (Finite Element Analysis) stress analysis can be used, as it can predict the crack initiation.

2.3 Accelerated Corrosion Testing

Due to industrial demand for new materials and alloys that offer good corrosion and wear resistance in different environments, accelerated corrosion testing is being heavily used to test and compare new alloys. Accelerated corrosion testing employs testing methods that provide corrosion results in a much shorter time than it takes for corrosion to occur in actual life. The first accelerated corrosion testing was carried out in 1914, at which time the well-known ASTM B117 salt spray (fog) testing was incorporated [12]. Usually a cabinet or chamber is used to provide a testing environment in which specimens are exposed to corrosive elements for a given period of time. After exposure, the specimen undergoes a cleaning process followed by an examination for corrosion, blisters and/or pitting and a coating evaluation. Accelerated corrosion testing can be divided into two types: static accelerated corrosion testing and cyclic accelerated corrosion testing.

In static testing, the chamber maintains a single environment during the entire testing period. The Salt Fog Test (ASTM B117) is the best known example of static accelerated corrosion testing in which the testing specimens or parts are continuously exposed to a 5% salt spray of NaCl solution with a pH between 6.5 to 7.2 and a temperature of 35°C, with 100% relative humidity [12]. ASTM B117 has been accepted as the standard corrosion test method for plated and painted finishes, electrical and military components. However, organizations such as ASTM, the Society of Automotive Engineers (SAE), the American Iron and Steel Institute (AISI), the Federation of Societies for Coatings Technologies (FSCT) and others, have realized the need to develop a more realistic accelerated test method rather than static testing method [44].

Cyclic accelerated corrosion testing was first introduced in England by Harrison and Timmons during the 1960s [45]. In this type of testing, the materials under study are exposed to different environments such as ambient, fog (spray), humid and dry environments. These different exposure environments make the cyclic corrosion testing more realistic and correlate to actual atmospheric exposure conditions. In the automotive industry, different standards have been issued for appropriate cyclic accelerated corrosion testing. Some commonly used tests include the Ford L-467 [46], the GM 9540P [47], and the SAE J2334 [48]. Table 2.4 summarizes the cyclic accelerated corrosion tests most commonly used by the automotive industry.

Table 2.4: Summary of the cyclic accelerated corrosion tests that commonly used in automotive industry

Standard	Salt Solution	Exposure	# of cycles	Correlation to real life
ASTM B117 [12]	5% NaCl	Continuous exposure to salt spray at 35°C, 100% relative humidity and solution pH between 6.5 to 7.2	As agreed between requester and corrosion department	Not specified
Ford L-467 [46]	0.5% NaCl	6h wet (fog) at 25°C 2.5h transition phase 15.5h constant temp. 50°C and humidity of 70%	As agreed between requester and corrosion department	Not specified
GM 9540P [47]	1.25% complex salt solution composed of 0.9% sodium chloride NaCl, 0.1% calcium chloride and 0.25% sodium bicarbonate	8h wet (fog) at 49°C 8h dry off at 60°C, ≤30% RH 8h ambient at 25°C, 45% RH	Depends on the location of the tested components (underbody, underhood or exterior) with maximum number of cycles =80	40 cycles (40 days) of GM 9540P is approximately equal to 5 year performance [49]
SAE J2334 [48]	0.675% of complex salt solution composed of 0.5% sodium chloride, 0.1% calcium chloride and 0.075% sodium bicarbonate	6h humid stage at 50°C, 100% RH 15min salt immersion stage under ambient conditions 17h 45min dry off stage at 60°C, 50% RH	Minimum 60	Reported to be equivalent to 5 years exposure in field testing in Montreal

2.4 Corrosion Protection Methods

Usually, through the alloying method, the corrosion resistance of Mg is improved. However, alloying Mg with other elements is not enough to provide the necessary corrosion protection. Therefore, further protection of the Mg alloy surface is required. Coating is the most widely used method to improve the corrosion resistance of Mg alloys; the coating inhibiting electric contact between the substrate and the sample surface. There are many different types of coating and methods of application. However, the pre-treatment and cleaning processes completed prior to the application of any coating are also critical. The appropriate pre-treatment helps to ensure the success of the coating and usually follows these steps: mechanical pre-treatment include grinding, polishing, particle-blasting and brushing. Alkaline cleaning is used mainly to remove any oils, grease or organic materials and acid etching is used to eliminate any oxide or hydroxide on the surface of the Mg alloy [8]. The following are the most commonly used techniques for coating:

2.4.1 Chemical Conversion Coating

Chemical conversion coating is considered one of the most effective and cheapest ways to prevent the corrosion of Mg alloy's base metals. The metal requiring protection is immersed in a solution which contains certain compounds that react with the surface. The reaction causes precipitation from the solution onto the surface of the base metal, forming a film, which provides a barrier between the metal and its environment through the corrosion inhibiting chemicals it contains. One of the biggest challenges with conversion coatings is to produce crack-free coatings with uniform coverage [1],[8]. Figure 2.20 shows the conventional conversion coating process. There are some factors that influence the effectiveness of conversion coating such as the pre-treatment processes used, the composition of the Mg alloy, the composition of the conversion formulation, any post-treatment procedures used, and the operational parameters such as temperature and pH [1],[8]. The most common conversion coating processes for Mg alloys are based on phosphate, chromate, fluorate, stannate, and cerium baths. Chromate conversion coatings have been used extensively as pre-treatment methods for Mg alloys to achieve good corrosion resistance and they result in a uniform layer on the surface [8]. However, the downside of chromate conversion coating is the highly toxic and carcinogenic nature of the Cr^{6+} in the chromate bath, which means its use is prohibited by environmental regulations [1]. Because of this, research has focused on finding chromium-free and more environmentally friendly conversion coating techniques which have corrosion resistance as good as the chromate conversion coating. Phosphate-silane [50] and zinc-phosphate conversion coatings [51] are examples of such chromium-free coatings.

However, these conversion coatings are pre-treatments in effect as the surfaces coated by these processes usually have unsatisfactory corrosion protection for many applications. They do offer a good adhesion surface for paints though.

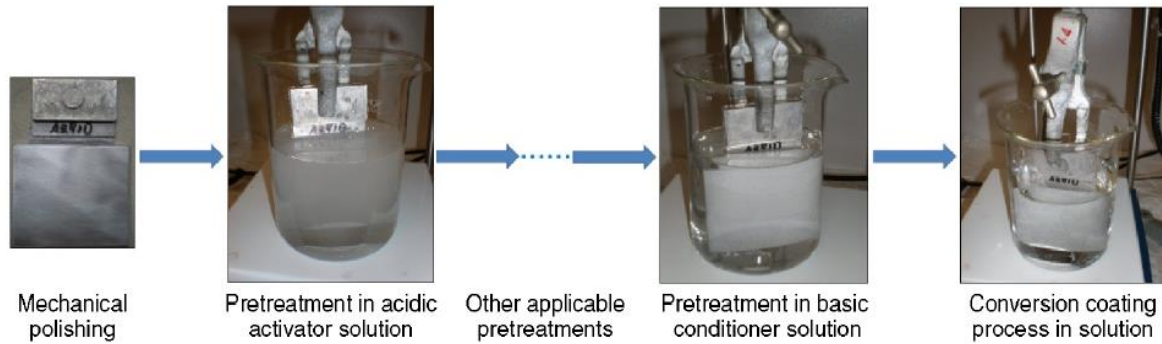


Figure 2.20: Steps in the conventional conversion coating process using AZ91D Mg alloy [8]

2.4.2 Electrochemical Plating

Electrochemical plating is one of the most cost effective and simplest techniques for introducing a metallic coating to a substrate. The plating process can be divided into two groups: electroplating and electroless plating. Prior to electroplating and after performing the appropriate pre-treatment, the metal must be given an undercoating either through direct electroless Ni-P coating or Zn immersion followed by pre-electroplating Cu, Ni, and Zn [1],[52]. The appropriate undercoating will result in a good plating process. In electroplating, through a process called electrodeposition, electrons are supplied from an external source to reduce the dissolved metal (cations) in order to form a coherent metal coating on an electrode. Electroplating is used mainly to change the surface properties of an object (e.g., abrasion and wear resistance, corrosion protection, qualities). Electroplating for Mg alloys is usually performed through three layers (Cu-Ni-Cr). The bottom layer of Cu ensures good adhesion, the Ni layer provides corrosion resistance and Cr is a high strength material for the outer layer. Combining these three elements together will result in a good coating system for Mg alloys [52]. In electroless or chemical plating, the reducing electrons are supplied by a chemical reducing agent in solution or, in the case of immersion plating, the substrate itself. Ni-P alloy coating is most frequently used in this technique. Electroless plating provides a uniform deposition on irregular parts. The problem with the plating methods is that they do not form a strong adhesion plating film on Mg alloys due to the high chemical activity of Mg. However, some case studies have revealed good coating adhesion and

uniformity [9],[52]. It was reported that in the case of plating Mg alloy AZ31 with Cu (Figure 2.21), there was good adhesion to the Mg substrate and a uniform 13 μm coating thickness [9].

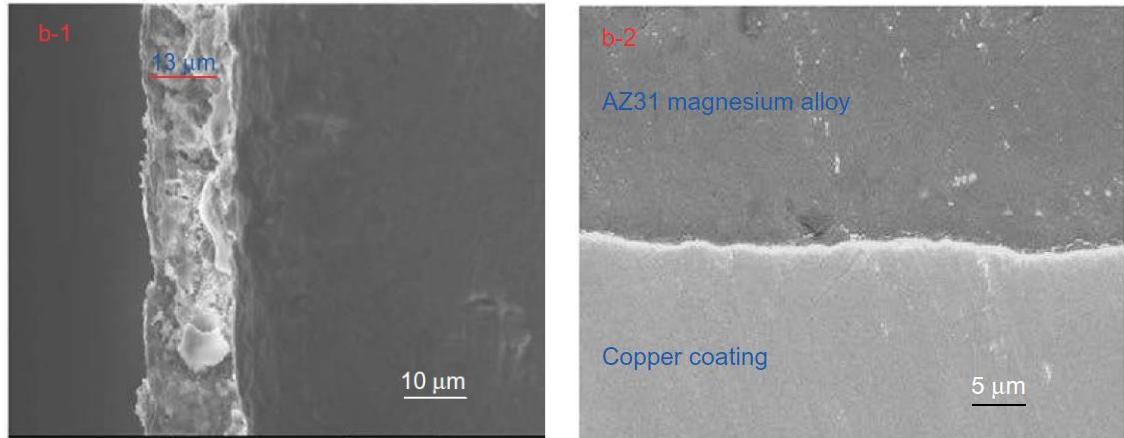


Figure 2.21: Example of copper plating on Mg AZ31 [9]

2.4.3 Plasma Electrolytic Oxidation (PEO)

Plasma Electrolytic Oxidation (PEO) Process, also known as micro-arc oxidation and spark anodizing, is an environmentally friendly coating technique. PEO is one of the most popular coating methods in recent years for Mg alloys in the industrialized world. This method passes high voltages (usually from 100 to 500V) through the surface to be coated in an electrolytic bath containing chemicals such as phosphates, silicates, hydroxides, fluorides etc. The resultant oxide coating is considered to be thick, hard, a very good adherent for ceramic coatings, and provide good corrosion resistance to the substrate. The coating that is formed usually consists of three layers with distinct levels of porosity; the upper layer being the most porous and loose layer [53],[54]. Figure 2.22 shows a cross section of PEO ceramic coating that was applied on AZ31 Mg alloy at 300 V/3 A/40 min. The oxidized ceramic coating consists of a loose layer (I), compact layer (II) and contact layer (III), and the total thickness is about 20 μm [10].



Figure 2.22: Microstructure of plasma electrolytic oxidation ceramic coating with three layers as (I) loose layer, (II) compact layer and (III) contact layer [10]

Many studies have been performed using PEO on AZ31 Mg alloy and examined including ceramic coating obtained through micro-arc oxidation processes [9], PEO of AZ31 in silicate solutions with different additives [55], PEO of AZ31 with aerosol deposition [56] and PEO of AZ31 with cerium conversion composite coatings [57].

2.4.4 Cold Spray Coating

Cold spray coating, also known as cold gas dynamic spraying and high-velocity particle consolidation, is a simple technique for surface protection. The concept of coating one metal with another was introduced early in the 20th century, with Thurston patenting a method in 1902 [58]. Schoop then patented a method to coat surfaces by spraying them with molten metal droplets, in 1915, the idea having come to him after he saw the deposition left on a wall after throwing a mud ball at it [58]. In the late 1980s, a team from the Institute of Theoretical and Applied Mechanics of the Siberian Division of the Russian Academy of Science developed a method of applying a cold spray coating [58]. The cold spray technique went through years of development and modifications in the US and Germany and now has become one of the most important means for applying surface protection for metals. In this process,

a small metal powder (1–50 μm) is accelerated in a gas flow at the desired metal surface at velocities of 500–1000 m/s at a temperature that is lower than the melting point of the powder [59],[60]. After leaving the accelerating nozzle, the particles impact the surface of the substrate and due to the high rate of plastic deformation and localized shear straining, the particles bond to the substrate and result in a solid state coating layer on the substrate. A simple schematic of a typical cold-spray apparatus is shown in Figure 2.23. A typical cold spray system consists of a powder feeder, supersonic nozzle, source for compressing the gas (helium, nitrogen or air), gas heater, spraying chamber and monitoring system for controlling the test parameters [59],[60].

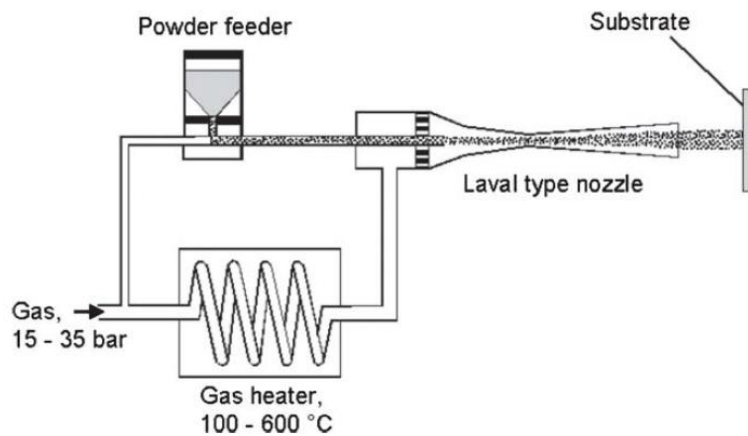


Figure 2.23: Schematic drawing of a typical cold gas spray apparatus [59]

There are basically two types of cold spray systems: high pressure cold spray (HPCS) and low pressure cold spray (LPCS). These two types differ in two ways. In an HPCS system, 25-30 bars of gas pressure are used while an LPCS system uses only 5-10 bars of pressure. The second distinction is that HPCS systems use axial injection for the powder while radial injection is utilized in LPCS [58],[60]. Good deposition of cold spray coating depends on many factors. The critical velocity is the minimum velocity the particles have to reach to transit from causing erosion to the substrate. It is very important for the particle velocity used in cold spraying to be greater than the critical velocity in order for deposition to occur, otherwise particles will either reflect or cause erosion on the substrate surface [58],[61]. The particle diameter also has a significant influence on the deposition process as it has been reported that small particles can be more easily accelerated and have higher impact velocity than larger particles, thus resulting in a better coating with lower porosity [58]. The particle size can also affect the process

itself, for example, if using particles with a size of less than $45\mu\text{m}$, device nozzle clogging may occur. The plastic behavior of the substrate and particles is also relevant to the deposition efficiency; it has been reported that using particles which are more plastic than the substrate will result in a better deposition of the coating. Materials with an FCC structure have the highest plasticity, followed by materials with hexagonal structures, while materials with a BCC structure have the lowest plasticity [58]. Figure 2.24 shows scanning electron micrographs of Cu particles that have been cold sprayed on a Cu substrate.

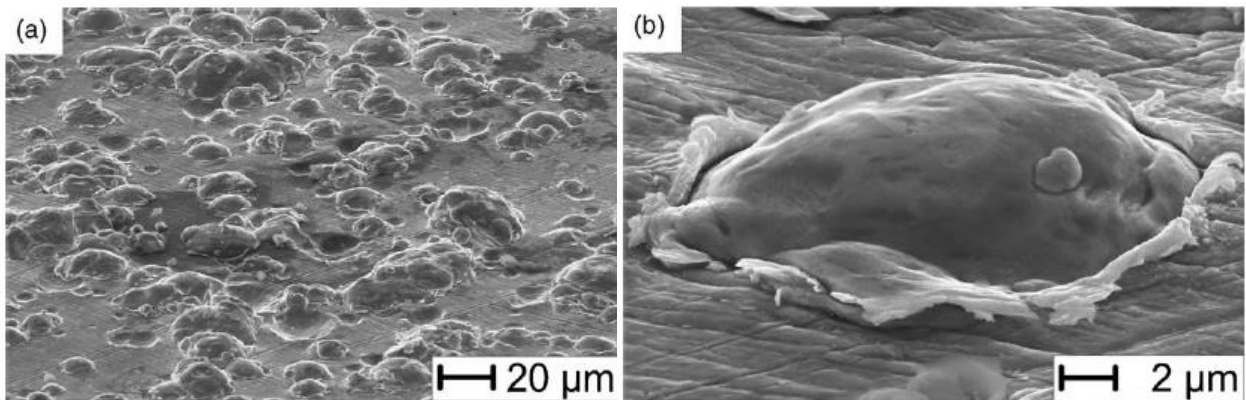


Figure 2.24: Scanning electron micrographs of cold sprayed copper particles on a copper substrate (a) an overview and (b) a close-up image [61]

In this research study, aluminum powder cold spray coating is being applied on the substrate Mg alloy AZ31B and nitrogen (oxygen-free) was used as the propellant gas. This coating was studied to investigate its effectiveness on the corrosion protection and corrosion fatigue life enhancement of Mg alloy AZ31B.

2.5 Literature Review

2.5.1 Corrosion of Mg Alloys

Even though the concerned alloy in this research is AZ31B, review of previous studies on the corrosion of different Mg alloys from different aspects is given in the table below for a better understanding of the corrosion of AZ31B.

Author	Corrosion Study Mechanism	Findings
O. Lunder, 1987 [62]	Two sets of AZ91 Mg alloy with different Mn and Fe concentrations were corrosion tested by immersion in 5% NaCl solution for 3 days to study the effect of adding Mn on the corrosion behaviour of AZ91.	Mn is an important alloying element for enabling Mg alloys with acceptable corrosion resistance especially when the proper Mn/Fe ratio is selected.
O. Lunder, 1989 [63]	Different heat treated AZ91 Mg alloys in the form of-cast (F), homogenized (T4), and artificially-aged (T6), with different distributions of β -phase in the alloy were tested by 3 days immersion in 5% NaCl solution.	The β -phase in AZ91 Mg alloy is more corrosion resistant than the surrounding matrix due to a better distribution of the β -phase at the ground boundaries. The T6 alloy exhibited the best corrosion resistance and the T4 showed the worst.
T. Beldjoudi, 1993 [64]	Solution-treated (T4) and artificially aged (T6) AZ91 Mg alloys were corrosion tested in a 5% NaCl solution. Electrochemical investigations were performed.	The T6 heat treatment decreased the Al content and the $Mg_{17}Al_{12}$ precipitated and act as a cathode to the alloy which improved its corrosion resistance.
G. Song, 1998 [65]	AZ21, AZ501 and AZ91 Mg alloys were corrosion tested in a 1N NaCl solution for 100 hours at room temperature. Results were presented by measuring electrochemical polarization curves for the tested alloys.	In terms of the corrosion rate and hydrogen evolution, the tested alloys performed as follows: AZ501 < AZ21 < AZ91. If the β phase volume is big, it will act as anode barrier and protect the alloy. If the β phase volume is small, it will act as a cathode and corrode the α -phase.

S. Mathieu, 2002 [34]	High pressure die-cast and semi-solid cast AZ91D were corrosion tested for 7 days in ASTM D1384-87 solution at room temperature.	The semi-solid process improved the distribution of the ($\alpha+\beta$) phases and led to an increase in the corrosion resistance as compare to the high pressure process.
Ming-Chun, 2008 [35]	AZ91D and reference pure material were corrosion tested by immersion in a 1N NaCl solution for 48 and 96 hrs. The corrosion behaviour was evaluated in terms of the evolved hydrogen and also by measuring the weight reduction of the specimens.	The β -phase in AZ91 works as a corrosion barrier as opposed to the alloy matrix. The corrosion rate for AZ91 is larger than for pure Mg. The corrosion rate is directly related to the hydrogen evolution rate.
Ming-Chun, 2009 [66]	Pure Mg, AZ31, AZ91, AM30, AM60 and ZE41 alloys were corrosion tested by immersion in 3wt% NaCl solution for 12 days. Hydrogen evolution and corrosion rate measurements were performed.	The corrosion behaviour of all tested alloys mainly depended on the volume fraction and electrochemical properties of the β -phase, and the composition of the α -phase.
C. Ying, 2009 [67]	Immersion corrosion testing in 1mol/liter NaCl solution for AZ31, AZ91, AM60 and ZK60 alloys was performed. The results were presented by electrochemical impedance spectroscopy and potentiodynamic polarization techniques.	Corrosion resistance followed this pattern ZK60 > AM60 > AZ31 > AZ91. Corrosion morphology for the four alloys depended on the distribution of the β . Since the Al content in AZ91 is higher than in AZ31, the β -phase was higher which led to more micro galvanic cells in AZ91.
W. Liu, 2009 [68] 2010 [69]	AM60 and AM60 Mg alloy with the addition of Ce or La alloys were corrosion tested by immersion test in 3.5% NaCl for 10 days at room temperature. The results were analyzed by electrochemical and hydrogen evolution measurements in addition to the microstructures study.	The addition of Ce or La provides a significant improvement in the corrosion resistance of AM60 due to the appearance of a new λ -phase that has the shape of a needle and results in a content reduction for the β -phase.

T. Zhang, 2011[70]	AZ91 alloys were tested as cast and extrusion by immersion in a 3.5% NaCl solution at room temperature for 12 hours. The test was analyzed by weight loss and electrochemical measurements.	The extrusion process for AZ91 worsened the corrosion resistance of the alloy because it decreased and changed the distribution of the β -phase as compared to that of the cast AZ91.
R. Arrabal, 2012 [71]	AM50 and AZ91D alloys with the addition of up to 1.5wt% of Nd were corrosion tested by immersion in 3.5% NaCl solution at 22°C for up to 5 days. The test was analyzed by galvanic and electrochemical measurements.	Adding Nd to AM50 and AZ91D reduced the β -phase due to the appearance of Al_2Nd which decreased the micro-galvanic performance. Adding $\approx 0.8wt\%$ Nd reduced the corrosion rate of AM50 and AZ91D by 90%, but adding more Nd did not reduce the rate any further.
H. Matsubara 2013 [72]	AM50 and AM60 alloys were corrosion tested by immersion in 5% NaCl solution at temperature of 45°C for 1-24 hour periods to study the effect of impurity Fe. The results were analyzed by corrosion weight and microscopic observations.	The corrosion rate depended on the percentage of the impurity and increased as the Fe/Mn ratio increased. The detected inclusions, from which the corrosion initiated, were mostly Al and Mn with a small quantity of Fe.
W. Song, 2014 [73]	Extruded AM30 alloy was tested with cyclic salt spray testing that included a 3.5wt% NaCl salt solution, high humidity and dry cycles at 35°C as well as immersion in a 3.5wt% NaCl at room temperature for 60 hours. Results were analyzed macro- and microscopically.	The general corrosion was more severe in the immersion testing than in the salt spray testing due to longer solution exposure. There was faster pit nucleation under immersion testing. There was more filiform corrosion apparent on specimens tested with the salt spray.
R. Matthew, 2015 [74]	Immersion corrosion testing of Mg alloy ZEK100 in 1.6wt% NaCl, 0.16wt% NaCl and deionized water was performed. The potentiodynamic polarization curve was plotted and macro corrosion pictures were analyzed.	The corrosion behaviour was related to the Cl content in the tested solution. Three phases were found on the corrosion surface: Mg-Zn-Nd (T-phase); Zn-Zr, Zr; and Fe-containing Zr (the most active cathode phase).

2.5.2 Corrosion of AZ31B

The corrosion behavior of Mg alloy AZ31B has been studied in the laboratory from different aspects and under different corrosive environments and setups. The following are the corrosion studies that were performed on Mg alloy AZ31B:

- Aung [36] studied the effect of grain size and twins on the corrosion behavior of AZ31B. Testing coupons with different heat treatments at 200, 300, 400 and 500 °C for 3 hour periods (which affects the grain size) were prepared and corrosion tested by immersion in 3.5wt% NaCl solution at room temperature for a maximum of 2 days. The results were analyzed by weight loss, hydrogen evolution and potentiodynamic measurements. It was concluded that the existence of twins in the as-received and 200 °C heat treated samples increased the corrosion severity. The application of heat treatment at 300 °C eliminated the twins and the corrosion resistance improved, however, corrosion pits appeared in samples heat treated at 400 and 500 °C and the worst corrosion was seen in the 500 °C samples.
- Qu [5] investigated the corrosion behavior of AZ31B in different concentrations of NaCl solution (0 , 10^{-5} , 10^{-4} , 10^{-3} , 10^{-2} , 10^{-1} mol L⁻¹), with and without CO₂ saturation, by immersion. Electrochemical measurements and surface analysis revealed that the corrosion rate increased as the NaCl concentration increased, and that the saturated NaCl solution increased the corrosion severity. However, as the immersion time lengthened, the CO₂ provided a thicker protective film and decreased the average corrosion rate.
- Zhang [75] prepared different AZ31B group of bars by different extrusion ratio. Immersion corrosion testing in 4wt% NaCl solution with pH of 7 for three days were performed in addition to others mechanical testing to study the effect of the different extrusion rate preparation on the corrosion behavior and on the mechanical properties of the alloys. It was concluded from this study that raising the extrusion ratio resulted in decreasing the grain size which improve the corrosion resistance of the alloy. Also this will lead to improving the yield strength and ultimate tensile strength of the alloy. It was also concluded that increasing the pH level will increase the corrosion resistance of AZ31B.
- Pu [76] performed burnishing on AZ31B in order to improve the corrosion resistance of the alloy by refining the grains and basal texture. Immersion corrosion testing in 5wt% NaCl solution at room temperature for 200 hours of burnished, and unburnished, samples was performed and the results were analyzed by surface analysis and electrochemical measurements. The burnishing process resulted in major grain refinements which led to better corrosion resistance. It was also concluded that the small

grain with little basal texture had less corrosion than the small grain with strong basal texture. No clear evidence was found in regards to the relation between residual stress and corrosion performance.

- Liao [6] studied the effect of AZ31B grain size on corrosion performance. By immersion and cyclic salt spray testing in 5wt% NaCl solution for 96 hours, he studied two AZ31B alloys with refined grains in comparison to two regular hot extruded AZ31B and AM60 samples. The results were analyzed by surface analysis, weight loss and electrochemical measurements. It was shown that the fine grained AZ31B alloys had better corrosion resistance than the other samples and he further concluded that reducing the grain size will enhance the passivity of the alloy. In 2013, Liao also studied grain size effect on corrosion behavior by testing fine grained AZ31B in comparison with hot extruded AZ31B with coarser grains [77]. The corrosion study was accomplished by exposing the alloys to marine and urban environments for a period of one year and then performing macro and micro analysis and weight loss measurements. It was found that the fine grained alloy exhibited better corrosion resistance than the more commonly used hot extruded alloy and the improvement in the corrosion resistance was attributed to the smaller grain size. The marine environment resulted in more aggressive corrosion for both alloys due to the higher concentration of NaCl in the marine environment versus the urban environment.
- A comparative study of AZ31B using immersion and potentiodynamic polarization testing with different concentrations of NaCl solution (0.2-1 M), pH levels (3-12), and exposure times (1-8 hrs.), was conducted by Thirumalaikumarasamy in 2014 [78]. The three variables that were manipulated are considered to be the most important factors affecting the corrosion behavior of AZ31B and the ranges selected reflect areas where the corrosion study results were limited to date. It was concluded from this work that the corrosion rate resulting from immersion testing is higher than that from potentiodynamic polarization testing. It was also reported that an acidic media causes more severe corrosion than alkaline media, and that the highest corrosion rate was at pH = 3. Finally, it was concluded that as the duration of the immersion test period increased a hydroxide film was shaped and improved the corrosion resistance of the alloy.

All of the above corrosion researches were performed using immersion testing technique, which doesn't mimic the automotive service environment as well as salt spray testing (fog), the used corrosion testing technique in this research.

2.5.3 Corrosion Fatigue of AZ31B

The corrosion fatigue behavior of different alloys and materials can be investigated in the laboratory under different corrosive environments and setups. The following are the corrosion fatigue studies that have been performed on Mg alloy AZ31:

- In 2008, Nan [79] performed corrosion fatigue testing of extruded alloy AZ31 using a 3% NaCl environment that was dripped on the smooth specimen under test at a flow rate of 140 ml/min and circulated back to the NaCl solution tank. The NaCl solution was exchanged once each day. A rotating bending machine was used for the fatigue testing at a frequency of 30 Hz and at room temperature. In order to protect the specimens under test from crevice corrosion, specific areas were protected with silicon resin. The S-N curve (Figure 2.25) was plotted based on the test results and it was compared with the results of fatigue testing on the same alloy but in laboratory air. An endurance limit at 120 MPa can be observed from the fatigue behavior of AZ31 in air, but there is no such limit in the NaCl corrosive environment where the specimen always failed regardless of the stress level.

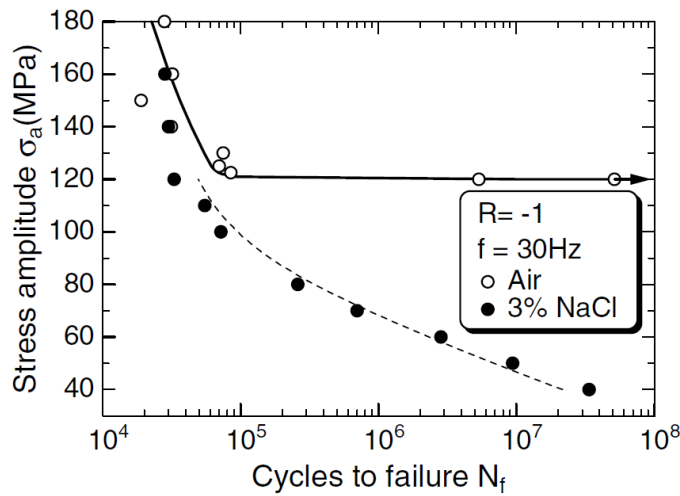


Figure 2.25: S-N curve for extruded AZ31 alloy in air and 3.5% NaCl [79]

This failure was attributed to the initiation of corrosion pits and crack growth on the specimens which grew until failure occurred when the stress rose above 120 MPa. Nan related the corrosion pit growth rate with the magnitude of the stress with the following expression:

$$P_{dep} = 2.2 \times 10^{-3} \times 1.08^{\sigma_a} t^{1.3}$$

Where σ_a and t represent the stress amplitude (MPa) and the failure time (hr).

- In other work, Eliezer [11] performed corrosion fatigue testing of die-cast AM50 and extrusion AZ31 alloys to study the fact that an increase in the Al percentage in Mg-Al-Zn-Mn alloys will lead to an increase in the fatigue life of the alloys in both air and corrosive environments. A 3.5% NaCl (pH≈5) solution was used as a corrosive environment and was dripped on the gauge of the specimen under test. A rotating bending machine was used to induce fatigue at a frequency of 30 Hz and at room temperature. The S-N curve (Figure 2.26) was plotted based on the corrosive environment fatigue test results for the AZ31 alloy and it was compared with the same test results for AM50 and for the two alloys tested in the laboratory air environment. It was concluded that the fatigue life in air for all of the tested alloys decreased significantly when compared to testing in the 3.5 NaCl solution but this decrease was more for the extrusion alloy.

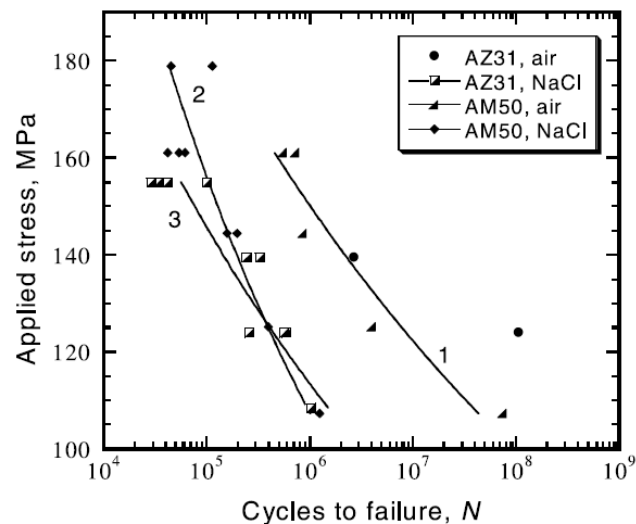


Figure 2.26: S-N curve for extruded AZ31 and AM50 alloys in air (1), AM50 in 3.5% NaCl (2), AZ31 in 3.5% NaCl (3) [11]

- In 2003, Unigovski [80] studied the corrosion fatigue of different extruded AZ31, AM50 and ZK60 Mg alloys in air, 3.5% NaCl, 3.5% NaCl saturated with Mg(OH)₂, 0.1N Na₂B₄O₇ buffer solution and 0.1N Na₂B₄O₇ saturated with Mg(OH)₂. For the solutions environment, he used a dripping down solution on the specimen gauge surface while circulating the solution between the specimen and the corrosion tank during the experiment with a constant rate pump. In this study, it was concluded that the fatigue life of all of the alloys in air was significantly longer than in NaCl-containing solutions. The ZK60 alloy

showed very high fatigue life and corrosion fatigue properties in comparison to the other alloys. The buffer $\text{Na}_2\text{B}_4\text{O}_7$ solution reduced the fatigue life of the AZ31 alloy, while the saturation $\text{Na}_2\text{B}_4\text{O}_7$ solution with $\text{Mg}(\text{OH})_2$ had no effect on the corrosion fatigue behavior of the AZ31 alloy; however, the $\text{Mg}(\text{OH})_2$ saturated 3.5% NaCl increased the corrosion fatigue life for the AZ31 alloy as shown in the S-N curve (Figure 2.27).

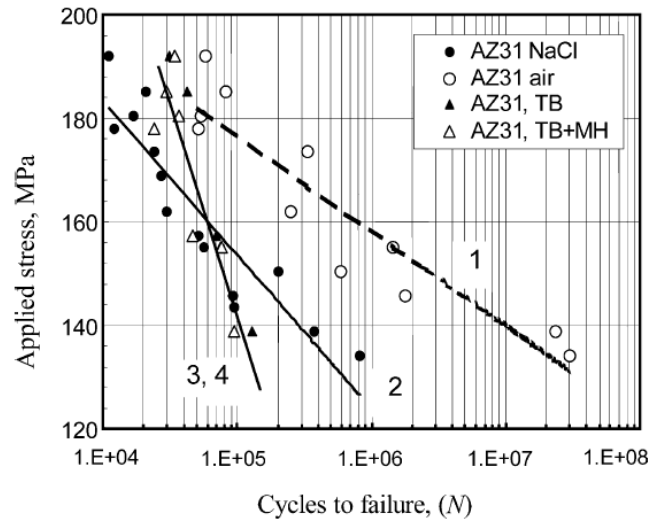


Figure 2.27: S-N curve for extruded AZ31 alloy (1) in air, (2) in 3.5% sodium chloride, (3) in 0.1N borate, and (4) 0.1N borate solution saturated with magnesium hydroxide [80]

- Pre-corroded specimens in accelerated salt spray fog environments were used in Chamos' 2010 work for investigating the fatigue behaviour of bare and pre-corroded Mg alloy AZ31 samples [81]. The pre-corrosion was accomplished based on the ASTM B117 standard with a 5% NaCl solution and a 6 hour exposure period. The fatigue testing was performed with two hydrolic MTS machines with a capacity of 100 and 250 KN, respectively. It was concluded that the pre-corroded material had lost 50% of its fatigue limit compared to the un-corroded material. From the S-N curve, it can be seen that the endurance limit was at a stress of 155 MPa which is close to the yield of AZ31 (163 MPa). The pre-corrosion caused the initiation of pitting on the specimens' surface which accelerated the fatigue crack growth.

It should be mentioned that there have been no studies conducted to date, to the author's best knowledge, on the corrosion fatigue of AZ31 extrusion Mg alloy with Al cold spray coating. In this research study, a comparison of corrosion fatigue life between bare and Al cold spray coated Mg alloy AZ31B is given.

2.5.4 Cold Spray of Mg Alloys

Significant amounts of research have been conducted on the coating of Mg alloys with Al particles by using cold spraying techniques and its effect on the corrosion resistance and the mechanical properties of the alloy.

- Mixing of particles into cold spray coating studies were carried out by Irissou [82] in 2007 and Spencer in 2009 [83]. Both groups studied the addition of hard ceramic particles into cold sprayed coatings in order to achieve higher densities of coating with less porosity than pure Al techniques. In Spencer's work, he compared the cold spray coating resulting from applying pure Al powder feedstock, Al + 25% Al₂O₃ and Al + 75% Al₂O₃ composite coatings on AZ91E Mg alloy substrates. After studying the microstructure for the three different coatings, it was observed that some porosity appeared in the pure Al coating, while when using the same cold spray conditions, a uniform and porosity free coating was achieved after the addition of 25% ceramic Al₂O₃. The addition of higher proportions of Al₂O₃ (i.e., >25%), resulted in a reduction in the deposition quality. According to the researchers, the results demonstrated that the Al-Al₂O₃ composite coating was stronger than the pure Al coating. For corrosion behavior comparison, both salt spray testing and electrochemical testing using linear potentiodynamic polarization were used in a neutral 5% NaCl solution. It was reported that the corrosion performance under both corrosion test scenarios was very similar for all three coatings, and that the corrosion resistance of the three coatings was similar to that of the bulk Al alloy comparator. However, the corrosion resistance performance of the three coatings was much better than that of the bare Mg alloy AZ91E substrate, in both corrosion testing environments [81],[82].
- Tao [84] studied the effects of mixing pure Al powder with 25% α -Al₂O₃ (Al25) and 50% α -Al₂O₃ (Al50) particles on the cold spray coating performance. He tested three groups of specimens, those with pure Al coating, Al25 and Al50, and compared the adhesion strength for the coating/substrate and the presence of micro-cracks within coating. According to his findings, the composite coatings showed better adhesion strength to substrate than the pure Al coating, and while some micro-cracks were noticed on the pure Al coating/substrate interface almost none were seen at the Al50 coating/substrate interface. The corrosion performance of samples with the three types of coating were compared to the performance of AZ91D and bare pure Al samples. The results showed that adding α -Al₂O₃ to the pure Al spray powder had no particular benefit as the corrosion current density of the three types of coating were almost the same. However, all three of the coatings showed better corrosion resistance

performance than the AZ91D, as their corrosion current densities were three orders lower than that of AZ91D (Figure 2.28).

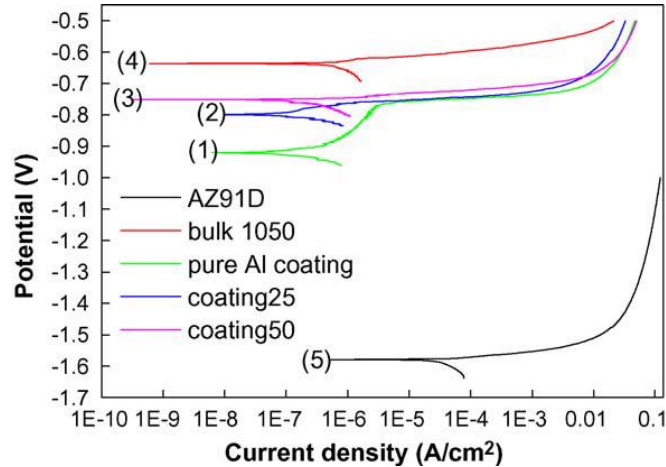


Figure 2.28: Potentiodynamic polarization curves in 3.5 wt.% NaCl solution [84]

- In 2010 Tao also studied the effect of cold spray coating on cast AZ91D using 1 to 40 μm spherical pure Al particles [85]. According to the cross-section micrographs reported, the coating shows good coating/substrate interface although some micron-sized cracks and pores were apparently detected within the coat. For the corrosion study, electrochemical measurements and surface morphology were performed on Al coated and bulk Al samples after immersion in a 3.5wt% NaCl solution for comparison purposes. The surface morphology study indicated that the Al cold spray exhibited better corrosion resistance than the bulk Al on which some areas were severely corroded. The cyclic polarisation curves for the Al coating and bulk Al (Figure 2.29), indicate that the bulk Al has a greater tendency for pitting corrosion given the smaller difference between E_{pit} and E_{corr} (lower resistance). The curves also indicate that the Al coating has better repassivation than the bulk since it shows a bigger difference between E_r and E_{corr} .

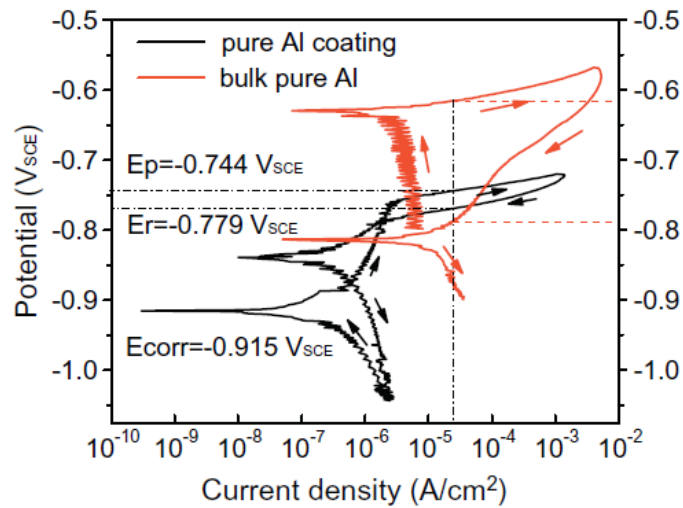


Figure 2.29: Cyclic polarization curves of cold sprayed pure Al coating and bulk pure Al after 1 h of immersion in a 3.5 wt.% NaCl solution [85]

- Spraying Mg substrate with high purity Al particles will result in a coating with low hardness. Deforce [60] tested the cold spray coating of cast ZE41A-T5 Mg alloy with high purity Al powder that contained 5wt.% Mg in order to enhance the hardness of the new alloy. For comparison, four groups of testing samples were prepared by spray coating with: 1) commercially pure 99.5wt.% Al pure particle powder, 2) high pure 99.95wt.% Al pure particle powder, 3) AA5356 5wt.% Mg powder, and 4) AA4047 12wt.% Si powder. The results showed that the high purity Al powder coatings showed highest adhesion strength and corrosion performance as they were tested in salt spray fog (ASTM B117) for 1000 hours without failure. The highest hardness measured was on AA5356 5wt.% Mg powder.
- It was proven that with the proper ratio of mixing hard particles to pure Al, the coating will have greater bonding strength. Hengyong [86] investigated the effects of adding intermetallic $Mg_{17}Al_{12}$ particles of a controlled volume to a pure Al powder with controlled particle size, in terms of the deposition pattern of a cold pressure spray coating on an as-cast AZ91D Mg substrate. The selection of the $Mg_{17}Al_{12}$ particle was based on the fact that it has a better corrosion resistance and four times higher hardness than the AZ91 Mg alloy. In terms of the coating's microstructure, it was reported that the pure Al cold spray coating resulted in a non-dense coating with high porosity, particularly in the top coating region, as can be seen in Figure 2.30a.

On the other hand, the pure Al mixed with the $Mg_{17}Al_{12}$ particles was successfully sprayed on the AZ91D Mg substrate and a coating build-up was obtained. It appears from a microstructure review

(Figure 2.30b), that a dense coating with no porosities even at the top region of the coating was obtained. Their measurements demonstrated that this coating had two to three times better cohesion strength on the Mg alloy substrate than the pure Al coating had shown [86].

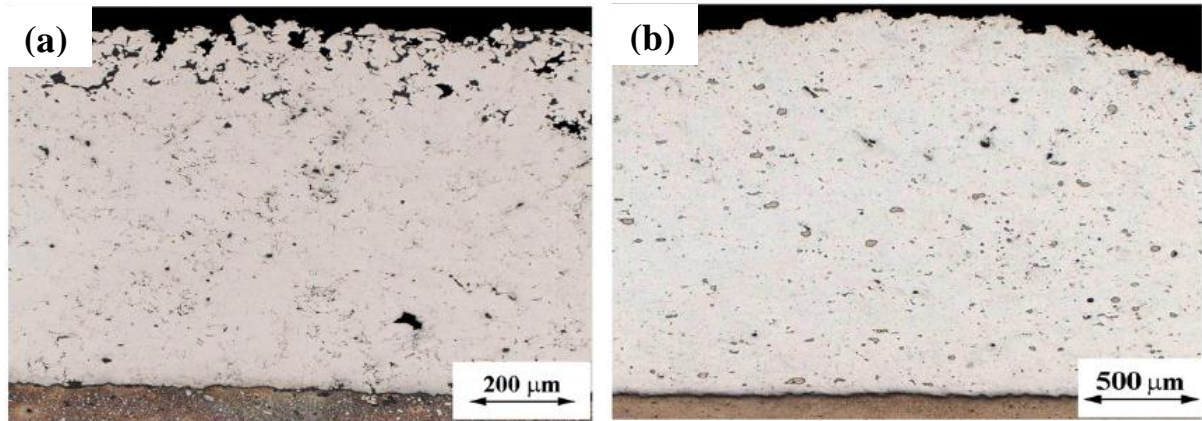


Figure 2.30: (a) Cross-section of pure aluminum coating on an AZ91D substrate, and (b) Scanning electron microscope image taken at the coating's top surface revealing the high level of porosity [86]

The mechanical properties for both types of coatings were also investigated. It was reported that the hardness measurements for the pure Al deposition coating decreased gradually towards the top coating surface which led to a weak coating at that region, hence, the increased porosity. This was not the case with the composite coating; the measurements taken close to the interface and at the coating top surface did not show a large difference. In terms of the corrosion resistance performance, it was noticed that by adding the $Mg_{17}Al_{12}$ particles to the pure Al feedstock in the cold spray coating procedure, the corrosion performance actually degraded [86].

From these studies, it can be concluded that the purity percentage of Al powder is playing an important role in the quality of the coating. There is no corrosion or corrosion fatigue studies conducted, to the author's best knowledge, on the corrosion of Al cold spray on AZ31 extrusion Mg alloy. In this research high purity Al powder ($> 99.93\%$) as initial stage is being used as cold spray feedstock and the corrosion and corrosion fatigue behavior of bare and Al cold spray coated Mg alloy AZ31B is studied in salt spray chamber.

Chapter 3

Materials and Experimental Methodology

This chapter provides detailed information about the research methodology utilized in this thesis: the materials, specimen characteristics and preparation; the testing equipment and standards; and the measurement tools and setup. In this study, the effect of Al cold spray coating on both the corrosion resistance and fatigue strength of AZ31B was examined. Two corrosion tests were performed in this thesis work; the first took place in a simple in-house chamber while a standard cyclic corrosion test chamber was used for the second. In both tests, uniform coupons with different dimensions were tested as per ASTM B117 standards. Two sets of coupons were used, one set were bare AZ31B and the other were Al cold spray coated AZ31B. For the corrosion fatigue study, another two sets of stress relieved cylindrical specimens, again AZ31B bare and AZ31B with Al cold spray coating, were used and tested by a rotating bending machine (RBM) to prepare S-N curves for each set.

3.1 Materials

The material investigated in this study was extruded Mg alloy AZ31B (Figure 3.1). The chemical composition of this alloy is given in Table 3.1 below [87].

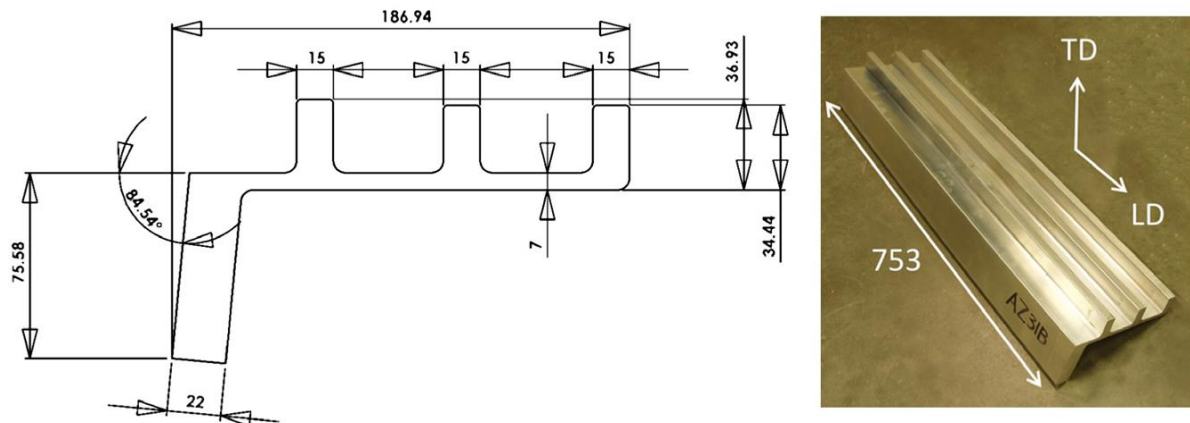


Figure 3.1: AZ31B extrusion (all dimensions in mm) [87]

Table 3.1: Chemical composition of the extruded AZ31B (wt.%) [87]

Al	Mn	Zn	Fe	Ni	Cu	Mg
3.10	0.54	1.05	0.0035	0.0007	0.0008	balance

For the first corrosion study, 20 coupons were machined and prepared (from the extrusion piece smaller teeth shown in Figure 3.1) in the University of Waterloo machine shop as per GM standard 14872 (Figure 3.2). Each of these coupons had dimensions of 25.4 mm x 50.8 mm x 3.18 mm (width, length and thickness). Half of these coupons were sent for Al cold spray coating to CenterLine in Windsor, Ontario, Canada (Figure 3.3). Details of the cold spraying process are discussed in Section 3.1.1.

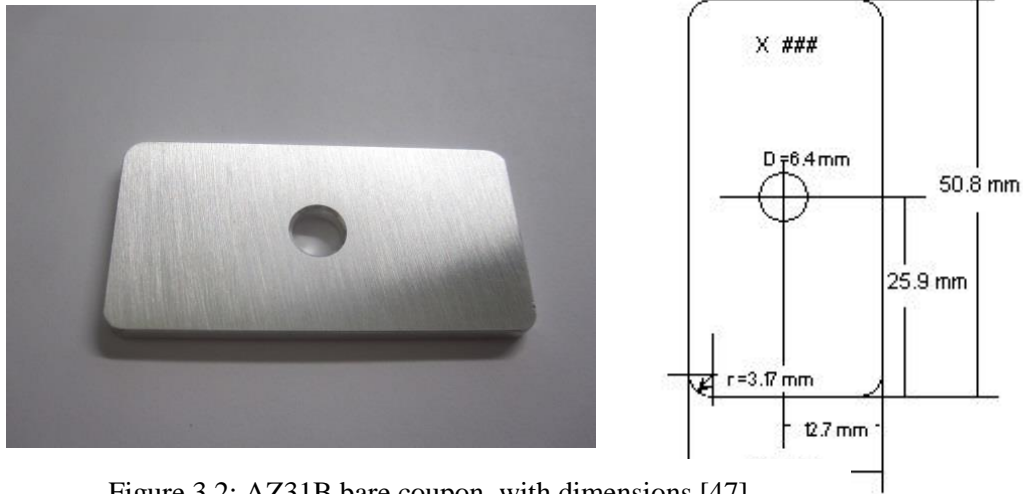


Figure 3.2: AZ31B bare coupon, with dimensions [47]



Figure 3.3: AZ31B Al cold spray coated coupon.

For the second corrosion study, 12 slices with the dimensions of 75mm x 260mm x 1.5mm (width, length and thickness) were wire cut from similar location of the extrusion AZ31B piece shown in Figure 3.1, by XL Tool Inc. in Kitchener, Ontario, Canada. Six slices were sent for Al cold spray coating to Centerline, as before. Corrosion testing coupons with dimensions of 50mm x 75mm x 1.5mm (width, length and thickness) were then cut from the 12 slices at the University of Waterloo machine shop for a total of 27 bare Mg alloy AZ31B, and 30 Mg alloy AZ31B Al cold spray coated, coupons as seen in Figure 3.4.

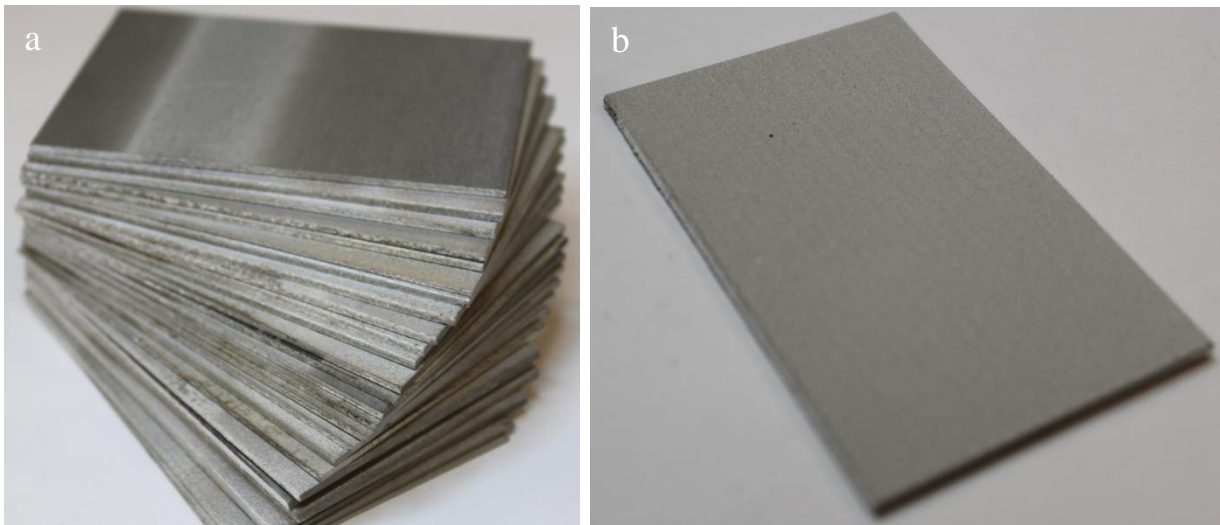


Figure 3.4: AZ31B (a) bare coupons and (b) an Al cold spray coated coupon for corrosion testing

Vickers hardness testing was performed on three different mounted and polished cross section samples from the coated coupons shown in Figure 3.4 to measure the hardness profile for the Al coating, interface and Mg substrate. The test was conducted according to ASTM E384-99 [88], at room temperature with a 100 g indentation load and a 15 sec holding time. Table 3.2 represents the profile results for the three areas; the letter C stands for the coating area, B for base metal and I stands for interface.

Table 3.2: Micro-indentation Vickers hardness test results at 100 gr.

Indentation No.	Average Readings, HB	Standard Deviation
1C	52.1	1.35
2C	51.2	2.25
3I	55.7	0.65
4B	62.8	1.05
5B	63.8	1.50
6B	62.5	1.32
7B	62.2	1.32
8B	61.5	1.3
9B	64.0	0.76
10B	63.1	2.35
11B	62.2	1.02
12B	61.5	1.53
13I	56.9	0.56
14C	52.1	0.62
15C	52.8	1.44

The hardness testing results show that the hardness of the three tested areas increases in the following order: B > I > C. Where the average hardness reading for B is 62.2 HB, for I is 56.4 HB and for C is 52.1 HB. These results are actually sensible since it was expected for the AZ31B alloy to have the higher hardness due to its high ultimate tensile strength as compared to the Al alloy. Figure 3.5 shows hardness indentations on the B, C and I.

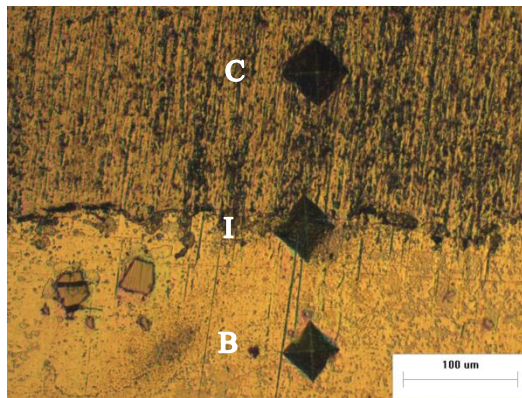


Figure 3.5: Optical microscope image showing the hardness indentations at C, I and B

Metallographic examination of cross sections taken from the coated coupons was conducted to study the Mg substrate and Al coating interface/bounding quality (Figure 3.6). A good bounding with no voids between the Mg substrate and the Al coating can be seen from the optical pictures. The applied Al coating was also apparently uniform, with a thickness range of 200 to 250 μm (Figure 3.7).

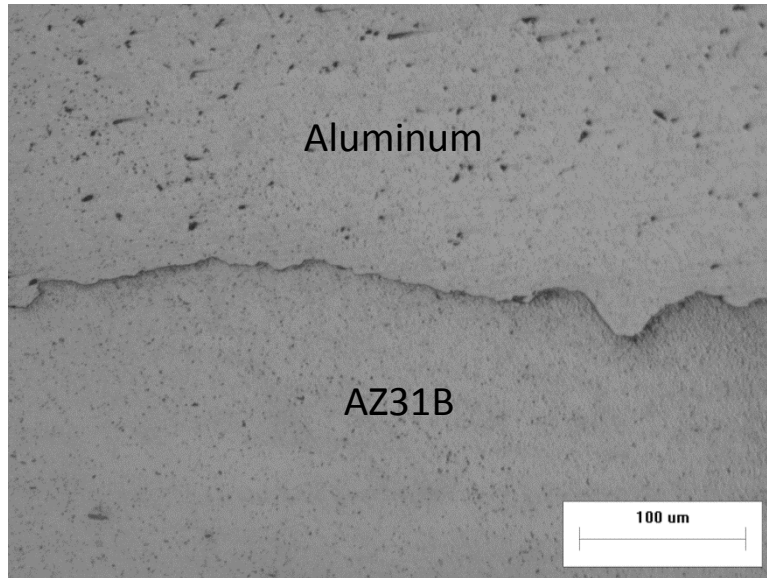


Figure 3.6: Optical microscope image showing Al coating interface

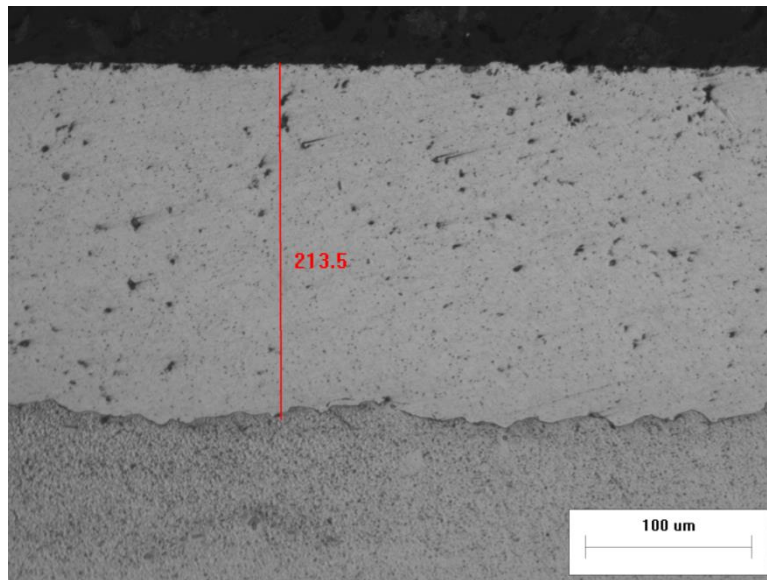
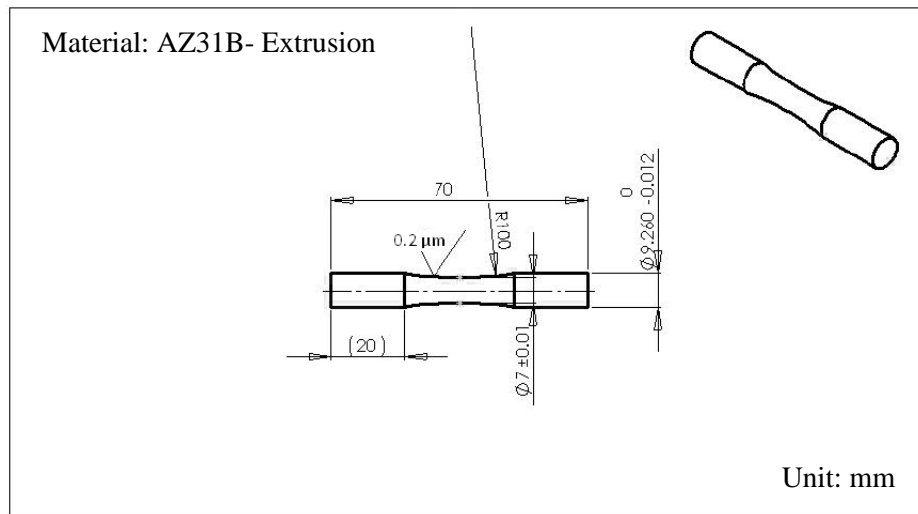


Figure 3.7: Optical microscope image showing Al coating thickness

For the corrosion fatigue test, 50 cylindrical specimens of AZ31B with dimensions shown in Figure 3.8 were machined and prepared from the extrusion AZ31B piece shown in Figure 3.1 at University of Waterloo machine shop in accordance with the RBM manual [89]. These specimens were then sent to Bodycote Thermal Processing, Kitchener, Ontario, Canada for stress relieve process. The procedure was done at 500 °F (260 °C) for 15 minutes, as per the ASM stress relieve process [40]. The reason for carrying out such a process is to eliminate any internal (residual) stresses that may have accumulated in the material. These stresses can cause undesired properties and behavior in the material including loss of tolerance, cracking and can contribute to some types of failures. Half of these specimens were sent after the stress relief process for Al cold spray coating to Centerline, as before.



(a)



(b)

(c)

Figure 3.8: Cylindrical specimens used for corrosion fatigue testing: (a) schematic and dimensions (b) bare and (c) Al cold spray coated

3.1.1 Cold Spraying of Samples

The cold spray process used on materials for this project was conducted by Supersonic Spray Technologies (SST), a division of CenterLine (Windsor) Ltd. Figure 3.9 shows typical low-pressure cold spraying equipment used by SST, however, for this research the testing coupons and cylindrical specimens were coated with a high-pressure cold spray applied inside a spray booth similar to what is illustrated in Figure 3.10.



Figure 3.9: Commercial low-pressure cold spray equipment. Picture courtesy of Supersonic Spray Technologies, a division of CenterLine (Windsor) Ltd [90]

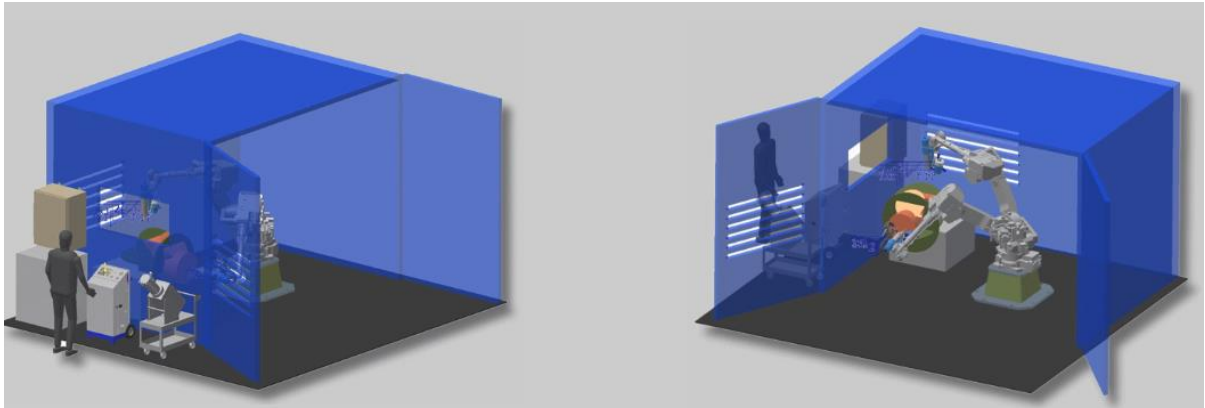


Figure 3.10: Schematic of the high-pressure cold spray booth used by Supersonic Spray Technologies, a division of CenterLine (Windsor) Ltd [90]

The following steps were carried out as part of this coating process:

- I. Every sample surface was grit-blasted with SST-G002 Al₂O₃ grit.
- II. Samples were cold sprayed with Al powder at the process settings of 500C/500psi, stepover=1.2mm, standoff distance=12mm, gun speed V_t=120mm/s, powder feed-rate of 18-20g/min, and nitrogen (oxygen-free) was used as the propellant gas.
- III. The Al powder used was series SST-A05011, purity Al>99.93%, density: 0.9-1.0 g/cc and had an average particle size of 20 μm (Figure 3.11).

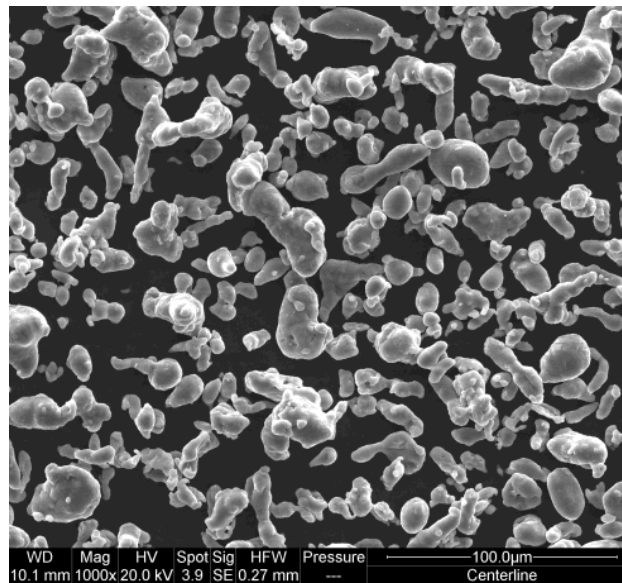


Figure 3.11: Morphology of aluminum powder used for the cold spray process

3.2 Testing Equipment and Standards

3.2.1 Corrosion Salt Spray (Fog) Test

The first corrosion study was performed and designed based on ASTM B117: Standard Practice for Operating Salt Spray (Fog) Apparatus. A simple in-house chamber was used (Figure 3.12) in which a two phased environment was applied within one day. The first phase involved 8 hours of mist cycles of 5% NaCl solution spray at 35°C, in which periodic puffs of salt spray (10 second duration every 15 minutes) elevated the relative humidity (RH) in the chamber to between 95-98%. After this 8 hour mist cycle, the chamber should have the ability to maintain a fixed humidity of at least 60% for 16 hours. The corrosive salt solution was prepared by dissolving five parts by mass of NaCl in 95 parts of distilled water to get a 5wt% NaCl solution. A special pH measuring tool was used to insure salt solution's pH between 6.5 to 7.2. The tested coupons were secured on a coupons rack by nylon fasteners, bolts, washers and nuts at 20° to the horizontal with 5 mm spacing between each coupon and the rack surface. The temperature was maintained at 35°C during the entire test and for that, a heater for the solution and a waterproof heating mat were also used inside the chamber. The temperature and humidity in the chamber were measured by sensor placed inside the chamber and the entire operation was controlled by Labview software.

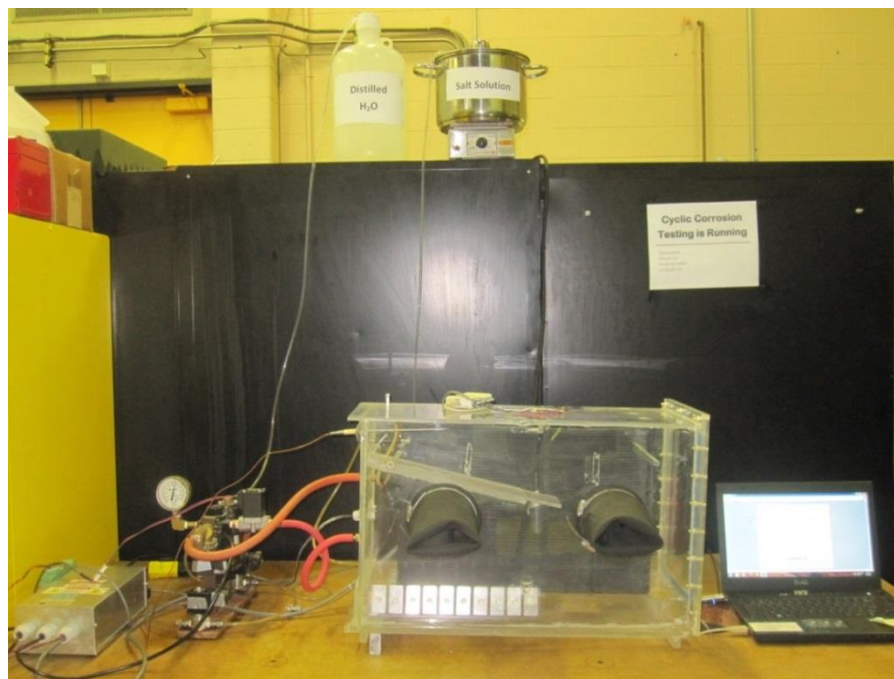


Figure 3.12: In-house corrosion testing apparatus and setup

The second corrosion study carried out as part of this research was performed at CanmetMATERIALS Technology Laboratory in Hamilton, Ontario, Canada as per the ASTM B117 standard. In this case, the testing coupons were exposed to a static environment of continuous salt spray exposure with a concentration of 5% NaCl at 36°C, 100% RH and a solution pH between 6.5 and 7.2 [12]. The basic apparatus for this testing are a closed testing chamber (Singleton Corp. SCCH - Salt Fog Chamber) that contains one or more atomizing nozzles (to atomize the salt solution within the chamber), a salt solution reservoir, specimen supports, provisions for heating the chamber and necessary means of control, and a humidifying tower connected to a reservoir. The specimens are subjected to a continuous dense saline fog. A schematic drawing of the basic components of the salt fog test chamber used is shown in Figure 3.13 below [44].

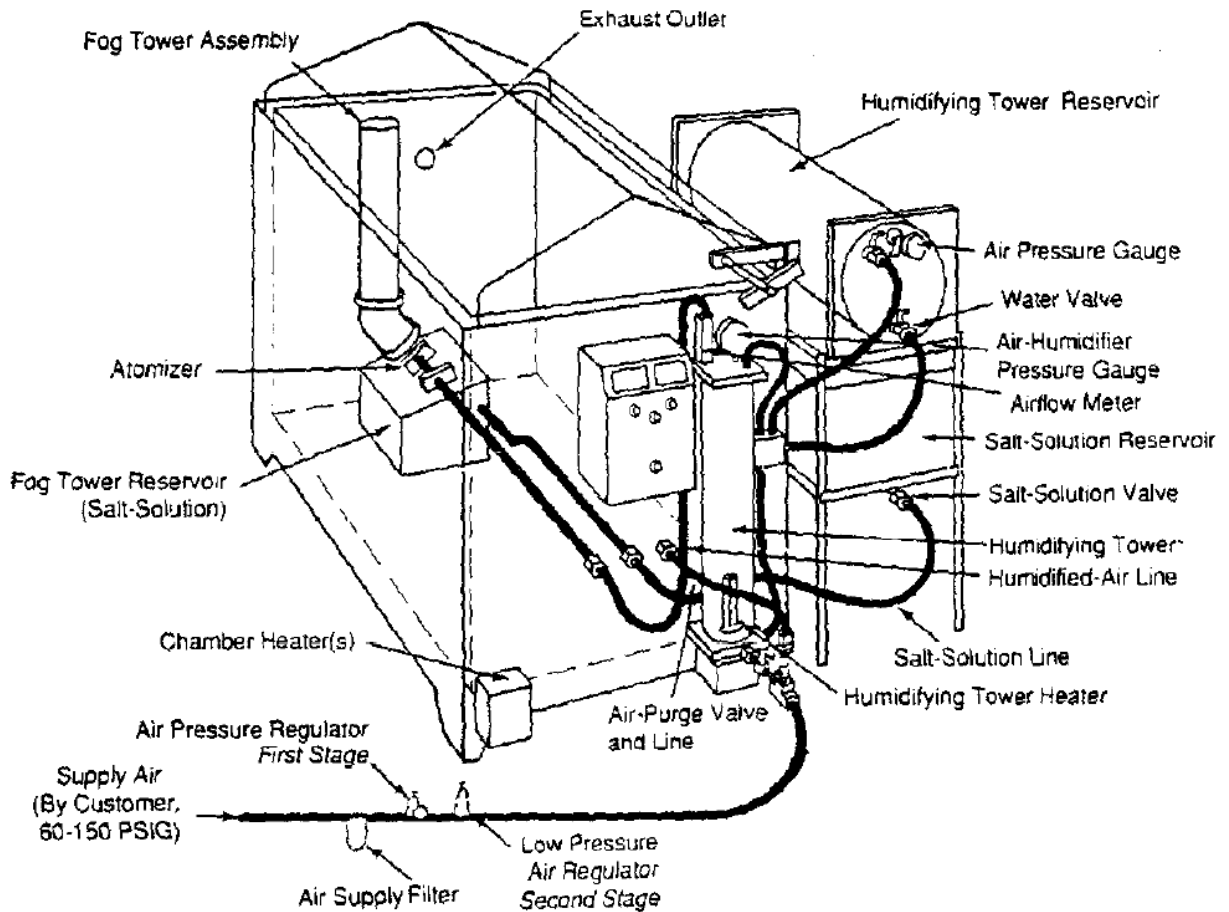


Figure 3.13: Schematic drawing of the salt fog test chamber used for corrosion testing [44]

As per the ASTM B117 standard, the following conditions were followed in both corrosion tests:

- I. Drops of solution which accumulate on the chamber ceiling due to fog shall not be permitted to fall on the specimens being exposed; in order to prevent this occurrence, a sloping ceiling is used on the corrosion chamber.
- II. Salt used in the experiment shall contain total impurities of no more than 0.3% by mass; specifically, halides (bromide, iodide, fluoride) shall contribute less than 0.1% to the mass of the salt content.
- III. The pH of the water solution should be kept between 6.5 and 7.2 to retain its integrity as “neutral” in terms of acidity – acidity can contribute to corrosion and is an unwanted factor in this case. This requires pH measurement instrumentation (to measure pH and temperature simultaneously) in the chamber and the ability to adjust the pH of the solution by adding acid or base to it to compensate for its pH change at 35°C.
- IV. The testing coupons shall be supported at an angle between 15° and 30° from the vertical direction.
- V. There should not be any contact between the coupons being tested and any metallic surface.
- VI. Fog collection should be performed with 1.0 to 2.0 ml of solution being collected per hour from each 80cm² of horizontal collection area.

ASTM G1 – 03 (Standard Practice for Preparing, Cleaning, and Evaluating Corrosion Test Specimens) [91] was used for cleaning all of the tested coupons after exposure to the corrosive environment in order to remove any corrosion products accumulated on the coupons without actually removing any of the base metal. The complete removal of the corrosion product ensured accuracy in the determination of the true mass loss of the tested alloy. Chemical cleaning procedures were used in this study that involved immersion of the corroded coupons in a solution designed to remove the corrosion products with minimal dissolution of any base metal. For Mg and Mg alloys, two chemical solutions could be used as listed in Table 3.3 [91]. Procedure C.5.1 was used during testing at UW, while procedure C.5.2 was used during the cleaning process in CanmetMATERIALS laboratory due to safety issue as it is conducted at room temperature which is considered to be safer than a procedure requiring boiling. The chemical cleaning solutions used is shown in Figure 3.14.

Table 3.3: Chemical cleaning approaches suitable for magnesium and its alloys [91]

Designation	Solution	Time	Temperature	Remarks
C.5.1	150 g chromium trioxide (CrO ₃) 10 g silver chromate (Ag ₂ CrO ₄) Reagent water to make 1000 mL	1 min	Boiling	The silver salt is present to precipitate chloride.
C.5.2	200 g chromium trioxide (CrO ₃) 10 g silver nitrate (AgNO ₃) 20 g barium nitrate (Ba(NO ₃) ₂) Reagent water to make 1000 mL	1 min	20 to 25°C	The barium salt is present to precipitate sulfate

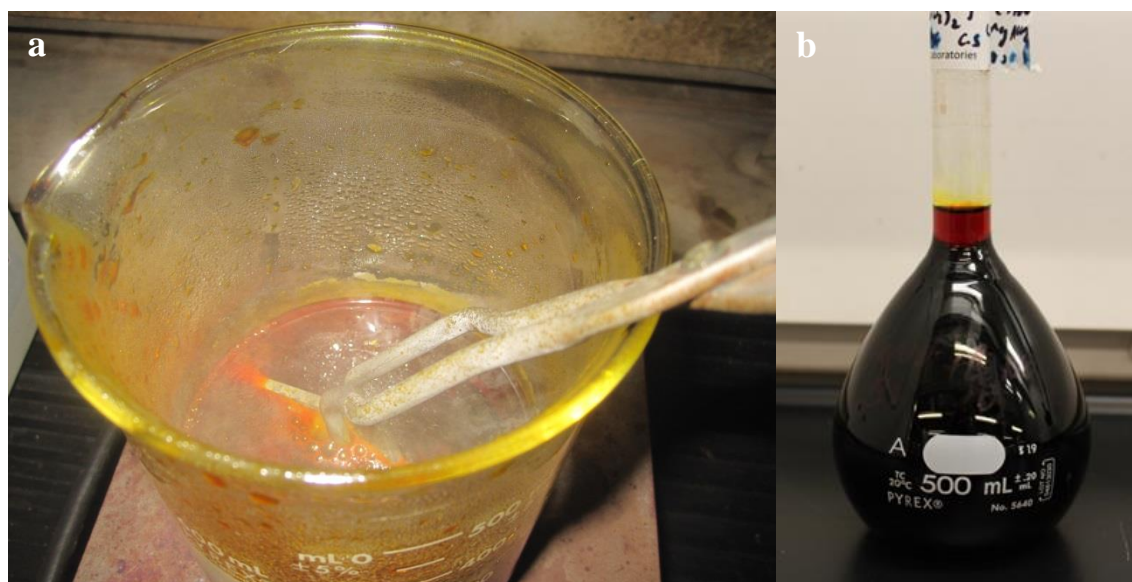


Figure 3.14: The prepared chemical cleaning solution (a) C.5.1 (b) C.5.2

The chemical cleaning procedure is usually followed by some light brushing/cleaning in reagent water to remove any loose products. Due to the heavy amounts of corrosion product that accumulated on the surface of the coupons in these experiments, the cleaning procedure was repeated several times for each coupon to ensure complete removal of the corrosion products. As per the ASTM G1 – 03, in order to eliminate any uncertainty in measuring the mass loss, the mass loss versus the number of times cleaned should be graphed and the cleaning process must be repeated until a slope line results from the data of all previous cleanings that is as close as possible to horizontal. In Figure 3.15, the line BC represents the corrosion of the metal after the removal of all corrosion products [91].

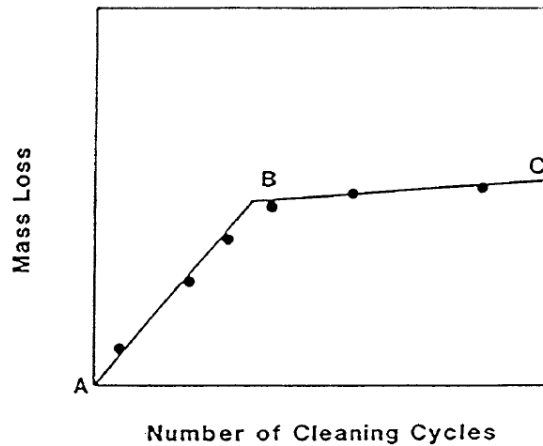


Figure 3.15: Mass losses of corroded specimens resulting from repetitive cleaning cycles [91]

In order to measure the weight of the tested coupons before and after the corrosion cycles, as well as before and after the chemical cleaning process, a four digits weighing scale was used. Plastic weighing boats and papers were also used for the weighing process. An SJ-400 surface roughness tester was utilized to measure the surface roughness of coated and uncoated coupons (Figure 3.16). Surface characterization and topographic analysis of the coupons was performed with AltiSurf® 500 laser profilometer (Figure 3.17) and Nanovea 3D Imaging (Figure 3.18), from which two dimensional (2D) and three dimensional (3D) images were generated. These images enabled surface characterization, measurement of functional parameters, pits measurements and 2D roughness analyses. An optical microscope, Scanning Electron Microscope (SEM) and Energy Dispersive X-ray (EDX) were also used in this study, particularly for the analysis of the cold spray coating bonding and analysis of microstructure and grains/grains boundaries.



Figure 3.16: SJ-400 surface roughness tester setup



Figure 3.17: AltiSurf® 500 laser profilometer for topographic analysis of samples

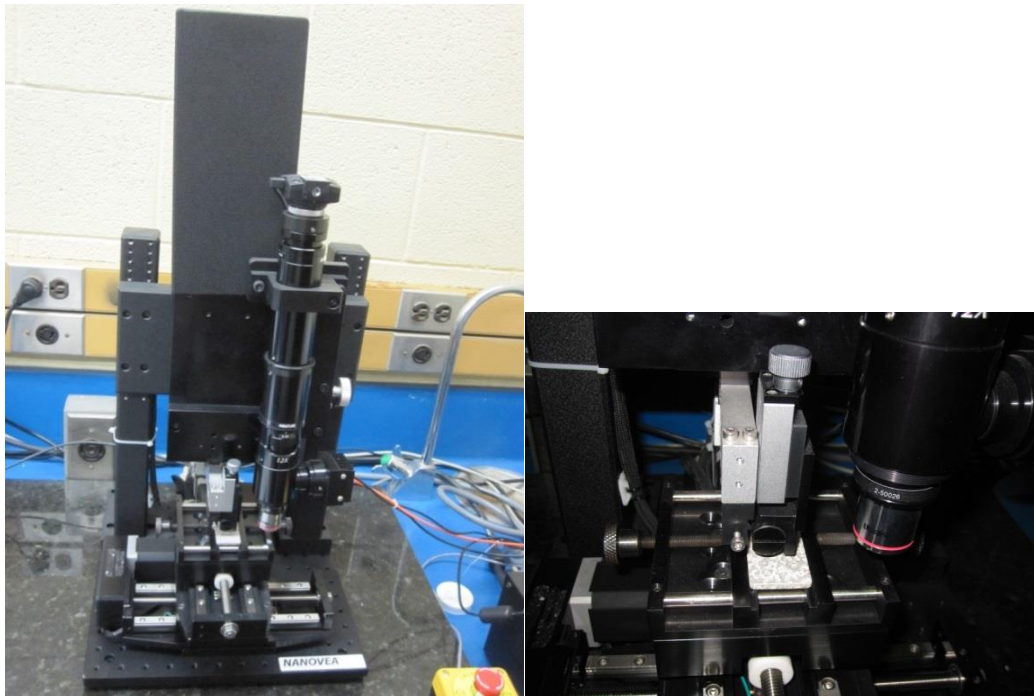


Figure 3.18: Nanovea 3D Imaging equipment

3.2.2 Fatigue Rotating Bending Machine

An R.R. Moore machine model was used for the fatigue testing. This equipment (Figure 3.19) is designed to perform high speed rotating beam fatigue tests on either straight shank specimens or tapered-end specimens. In this study, the cylindrical specimens shown in Figure 3.8 were used and gripped by two collets between the two bearing housings. The two bearing housings (Figure 3.19a) are precision machined units that house the specimen as well as a lubrication and cooling system for the bearings. The weight pan assemblies (Figure 3.19b), and loading harness (Figure 3.19c), placed under the equipment are used to apply the required load to the specimen. The loading harness hangs from the bearing housings in which variable load disks can be added to reach the desired amount of applied stress [89]. These weights cause constant bending moments in a vertical plane to the specimen so that a maximum compressive stress results at the top point of the specimen and maximum tensile stress at the lower point of the specimen with no axial strain. The rotational movement is accomplished by an electrical motor that has an adjustable speed regulation from 500 RPM to 10,000 RPM. Each revolution of the motor and specimen is sensed by the magnetic sensor at the motor shaft. The sensor then sends the count signal to a digital display revolution counter to a maximum total of 99,999,999 cycles [89] but usually, 10 million cycles is considered as the run out or endurance limit. By applying different loads to the tested specimens, different numbers of cycles to failure will be generated and these are the data needed to generate the S-N curve.

The corrosive addition to fatigue testing machine can be achieved by one of three methods: dripping a salt solution down onto the specimen gauge surface during the fatigue testing [79], pre-corroding the specimens in an accelerated salt spray fog environment [81], or by using a specially designed chamber within the fatigue setup in which the specimens are continually sprayed with an NaCl solution [92]. In this study the first method was used, and a special transparent pocket made of plexiglass (Figure 3.20) was designed to contain the salt solution splashes and allow draining of the solution. The salt solution dripped down onto the specimen gauge surface through a tube from a large container with a capacity of 18.9 liters which had a controlling valve to control the solution flow rate. The solution which accumulated at the bottom of the pocket was drained into another tank underneath the fatigue machine through a drain hole connected to a hose.



Figure 3.19: R.R. Moore Rotational Beam Fatigue Testing Machine: (a) bearing housing, (b) weight pan, and (c) loading harness [89]



Figure 3.20: Setup for the corrosion fatigue testing

Chapter 4

Experimental Results and Discussion

In this chapter, the author's findings regarding the impact of Al cold spray coating on the corrosion resistance and fatigue strength of AZ31B are reported. A summary of the measurements and results, generated during the experiments described in the previous chapter, are presented and discussed.

4.1 UW Corrosion Testing Results

The duration of exposure for this testing was set to be 15 cycles (days) for both bare and Al cold spray coated AZ31B with two coupons removed every 3 cycles. Prior to being affixed within the testing environments, the Al coated coupons were sandpapered in order to smooth the surface and to make the coating layer more uniform. Sandpapering the Al coated coupons' surface resulted in a uniform coating thickness of around 230-240 μm . Edge protection was needed on the cold sprayed coupons since not much Al coating had been applied to the edges. For this reason, silicone resin was used to cover the edges and prevent possible contact between the salt solution and the uncoated areas as seen in Figure 4.1.



Figure 4.1: Coupons edges protected with silicon resin

4.1.1 Bare AZ31B Coupons Corrosion Testing

Figure 4.2 shows the corrosion morphologies of the bare AZ31B coupon surfaces before and after the 5wt% NaCl exposure. From a visual examination, it can be seen that up to 6 cycles of exposure (Figure 4.2c) no clear pits had formed on the surface but general corrosion on the coupons surface is started. However, beginning from cycle 9 (Figure 4.2d), general corrosion is more clear and pits had started to arise and were distributed across the surface. The general corrosion and pitting became more severe after cycles 12 and 15, with the pits becoming wider and shallower (Figure 4.2e, f). The influence of grains, grains boundaries and secondary phases within the microstructure is playing an important role in the corrosion behavior of the alloy. More elaboration on this effect and the general and pitting corrosion causes and mechanisms is discussed in details in section 4.2.1.

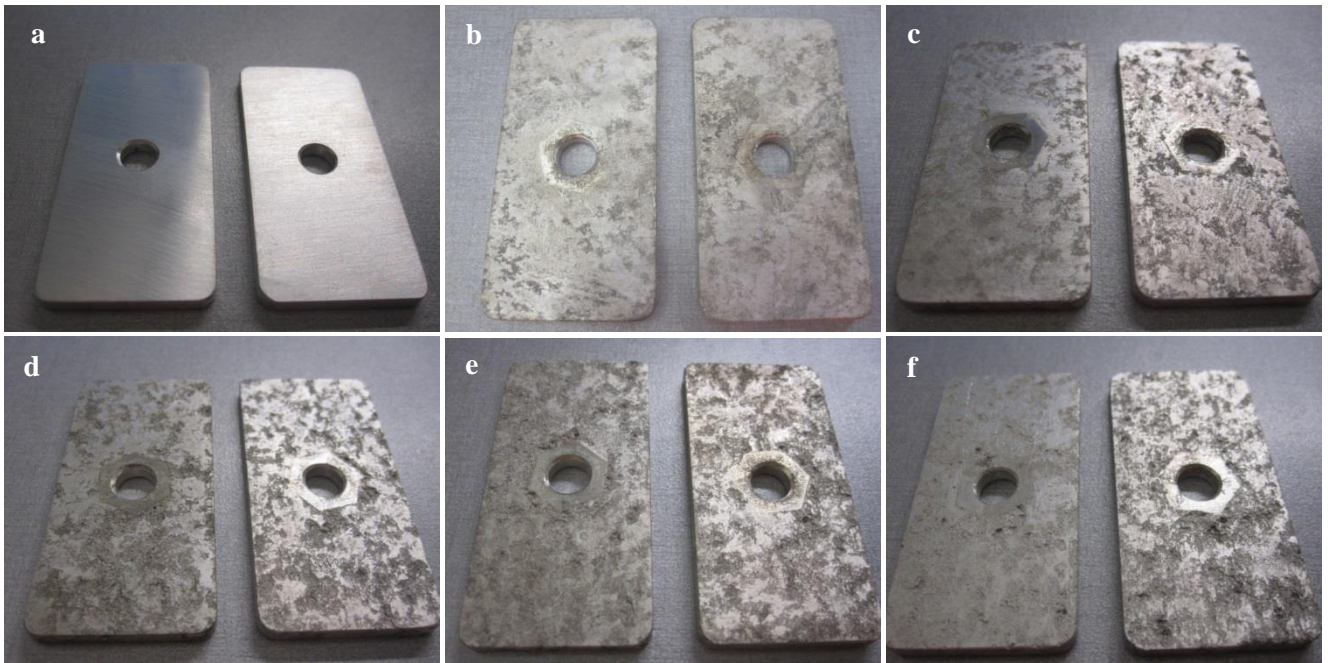


Figure 4.2: Bare AZ31B coupons before and after 15 days of salt spray exposure: (a) before testing,

Figure 4.3 shows the average weight loss per surface area for the tested bare AZ31B coupons over the 15 exposure cycles in salt spray environments (removal frequency is two coupons). By analyzing the chart, it can be argued that the average weight loss behavior followed a generally linear trend but that after 6 cycles the weight loss seems to be more aggressive. The linear increase indicated that the corrosion products generated were not protective to the base metal and that the created $Mg(OH)_2$ layer film is weak as it does not slow the corrosion rate. The weight loss measurements are also consistent

with the general corrosion morphology over the 15 cycles shown in Figure 4.2. The vertical lines are standard deviations.

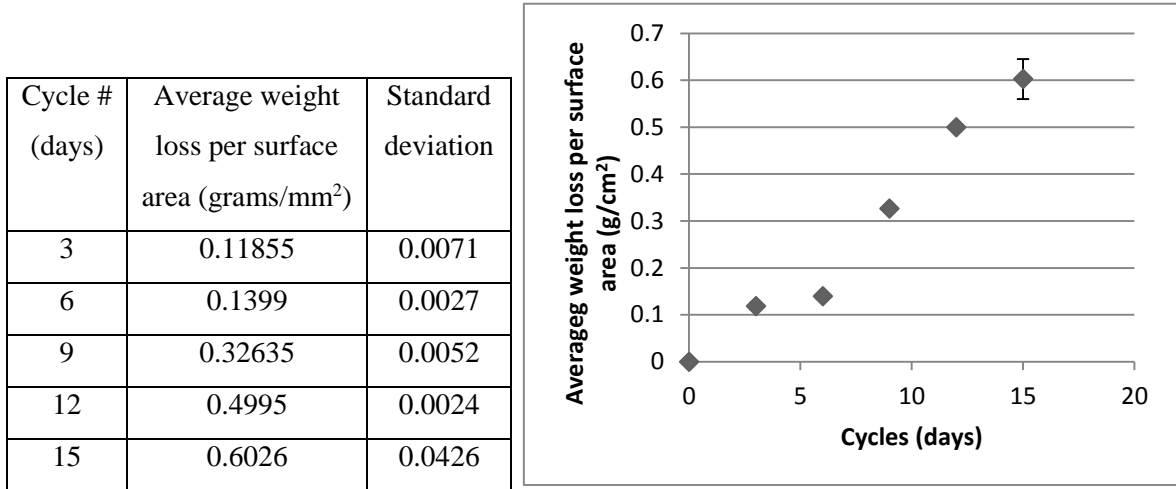


Figure 4.3: Average weight loss versus the number of tested cycles

Figure 4.4 shows the average of few thousands roughness measurements for the bare and Al coated AZ31B coupons before and after the salt spray exposure. Due to the machining process, the coupons had some variation in their surface roughness, therefore, roughness measurements were taken in two directions: longitudinal and transverse. As described previously, the roughness measurements were performed by the SJ-400 surface roughness tester. A limitation of this machine is that it is only able to measure the roughness through a line rather than for an area. For this reason, several measurements were taken and the average of these reading was considered. The vertical lines are standard deviations.

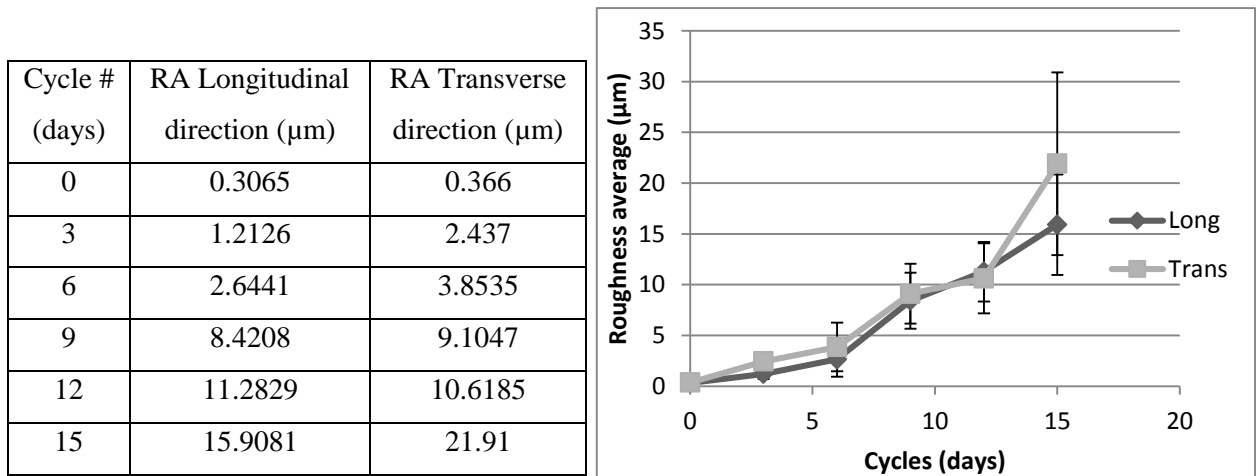


Figure 4.4: Average roughness measurements versus the number of tested cycles

microstructure of the alloy, for example grain size, spacing between cathodic secondary phases which will be discussed in details in section 4.2.

Pit measurement was done via an optical microscope. Figure 4.5 shows typical sizes of the pits developed after every 3 cycles of exposure. As seen in these pictures, the pit sizes increased with the increasing number of cycles.

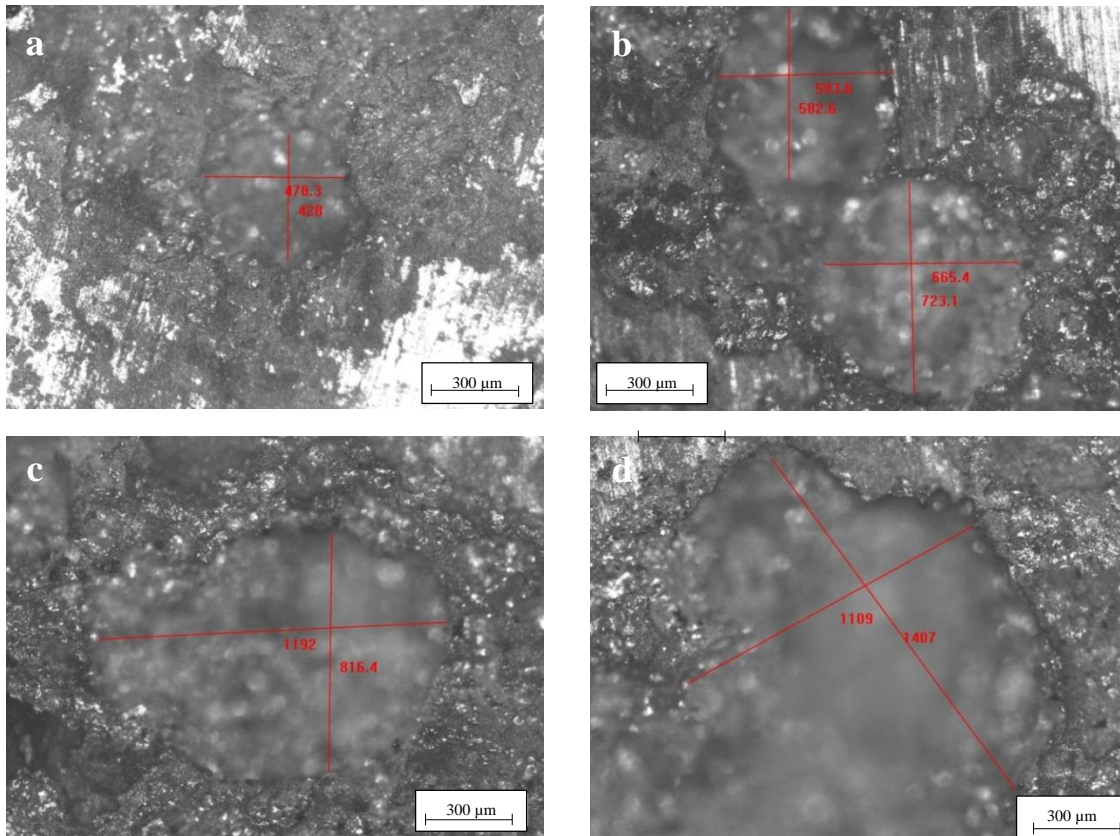


Figure 4.5: Typical sizes of the pits in bare coupons after: (a) 6 cycles, (b) 9 cycles, (c) 12 cycles, and (d) 15 cycles in bare and coated coupons

All pit measurements from each set of coupons tested/cycle were averaged together and reported in Figure 4.6 below. The changes in average pit diameter for both the coated and uncoated coupons over the 15 cycles of exposure follow a linear trend after 3 cycles. The vertical lines are standard deviations.

Cycle # (days)	Average pit diameter (μm)	Average # of pits per unit area (pits/ mm^2)
0	0	0
3	0	0
6	345.4	5
9	678.7	8
12	745.2	20
15	910.9	37

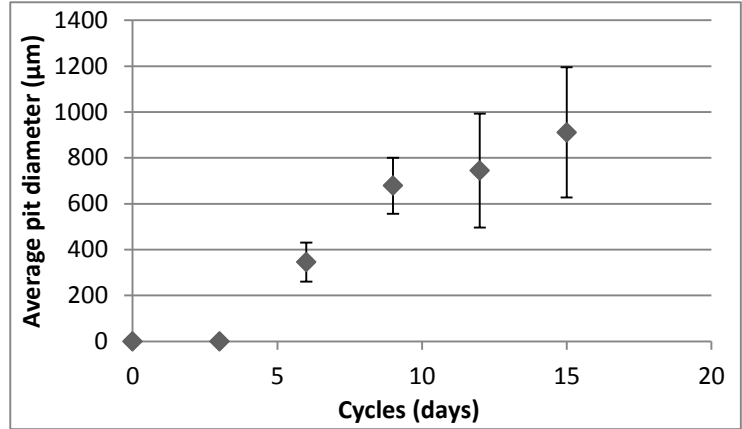


Figure 4.6: Average pit diameter versus the number of tested cycles for bare and coated coupons

Pit depth was also studied by using the Nanovea 3D Imaging equipment in which a 3D image of an area was produced and analyzed. A limitation of this equipment is that only a small area size can be studied each time. Figure 4.7 presents a typical example of a $5.0 \times 5.0 \text{ (mm)}^2$ area in which a pit with a depth $\approx 240 \mu\text{m}$ and size $\approx 1500 \times 1700 \mu\text{m}$ can be seen.

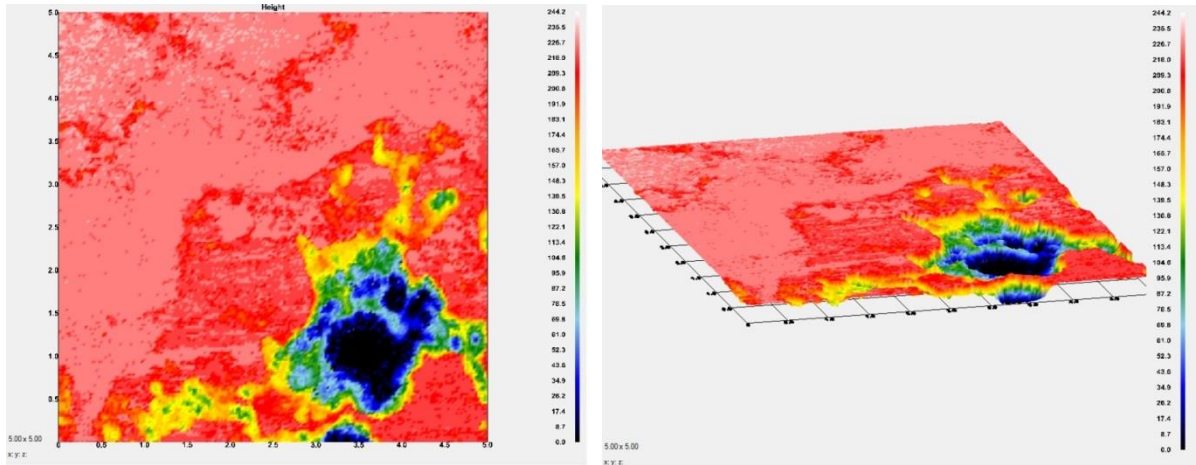


Figure 4.7: Example of surface analysis by Nanovea 3D Imaging showing a pit in a bare coupon

In Figure 4.8, it can be seen that the average pit depth seems to increase systematically over the exposure time in a linear fashion. From cycles 3 to 6, the pit depth increased at a steeper rate than between cycles 6 to 15. The pits and surface characteristics shown on Figure 4.6 and 4.8 on the salt-

spray surfaces were affected by the cycling of the water, which did not continuously remove the pit debris, trapping chloride ions and allowing the pits to grow deeper and wider initially but more slowly later in time. The vertical lines are standard deviations.

More discussion on the general and pitting corrosion causes and mechanisms is discussed in detail in section 4.2.1.

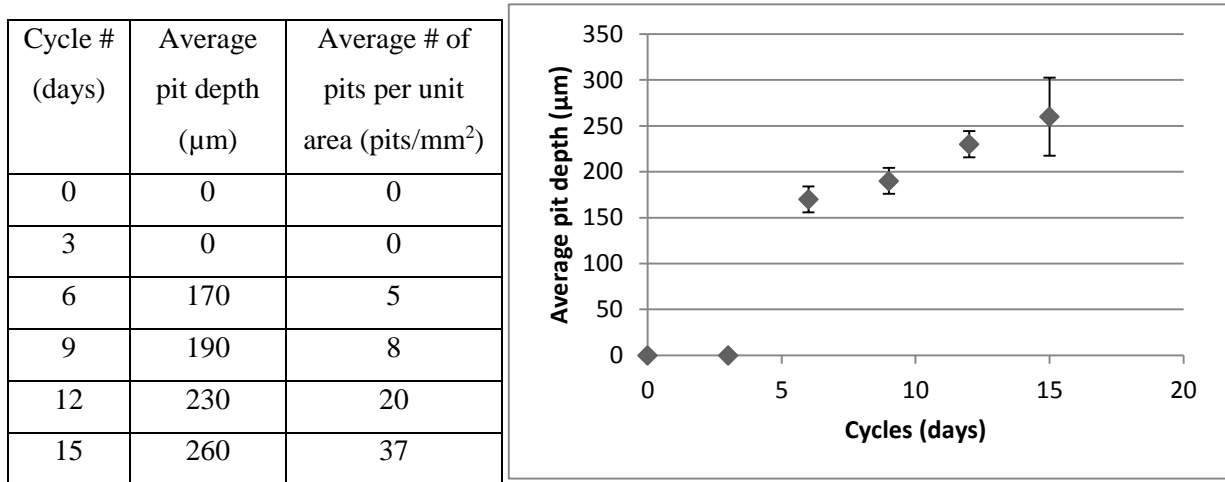


Figure 4.8: Average pit depth versus the number of tested cycles for bare and coated coupons

4.1.2 Al Cold Spray AZ31B Coupons Corrosion Testing

Figure 4.9 shows the corrosion morphologies of the Al cold spray coated AZ31B coupon surfaces before and after the 5 % salt spray exposure. From a visual examination, it can be seen that up to 6 cycles (Figure 4.9c), there were no corrosion or clear pits on the surface, but from cycle 9 (Figure 4.9d) onward, small pits began to appear close to the edge. These pits most likely resulted from the penetration of the corrosive solution to areas of the edges of the substrate that were not well coated or protected by the silicone resin and proceeded from there. After 12 and 15 days of exposure, large localized pitting had appeared on the surface near the edges and some had begun in the middle of the surface as shown in (Figure 4.9e, f). The detected pits at middle of surfaces of coupons from the 12 and 15 cycles are most likely developed due to defect of the Al cold spray coating at those areas since the coating around them did not attacked. After 9 cycles, the Al cold spray coating had been removed from some areas on the coupons' surface.

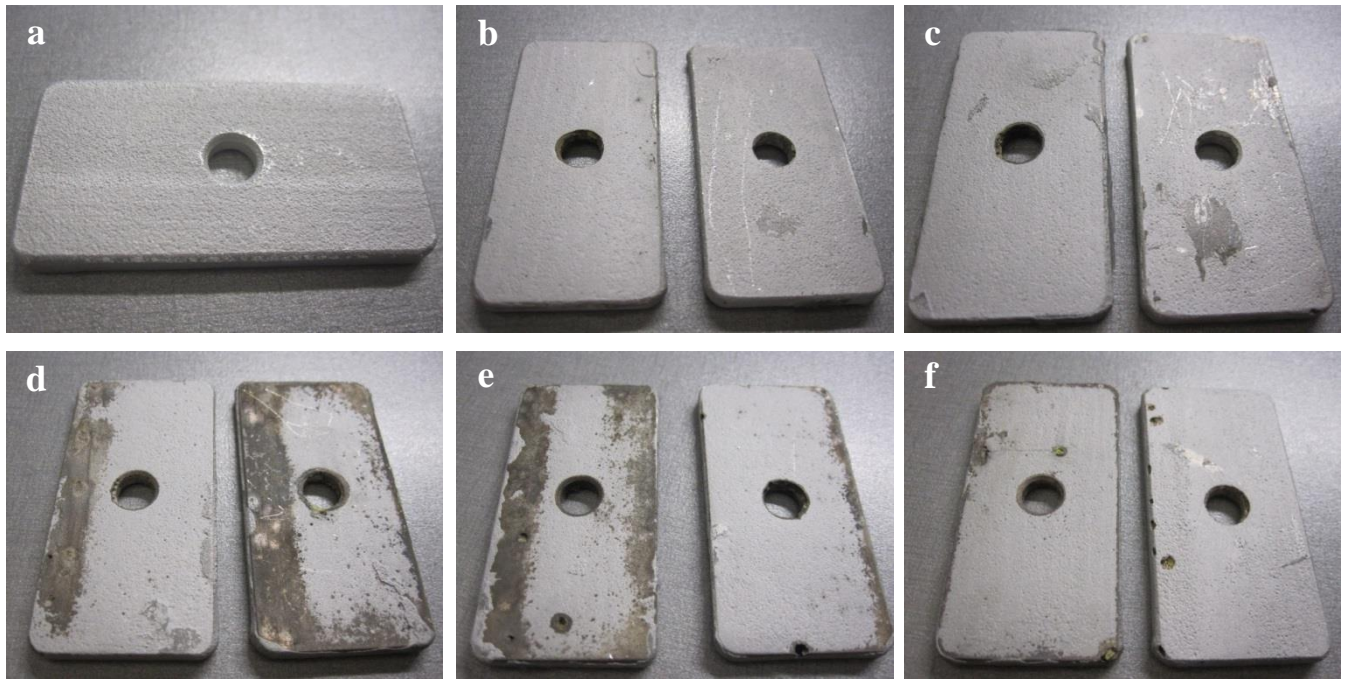


Figure 4.9 Coated coupons before and after 15 days of salt spray exposure: (a) before testing, (b) after 3 cycles, (c) after 6 cycles, (d) after 9 cycles, (e) after 12 cycles, and (f) after 15 cycles

The average weight loss for the coated coupons over 15 exposure cycles in a salt spray environment was measured and reported as shown in Figure 4.10. The average weight loss increased over time, but after 6 cycles the weight loss seems to be more aggressive. The large standard deviations of the two replicates coupons at cycles 9, 12 and 15 are due to the variations of the percentage of Al cold spray coating peeling off of the coupons after the chemical cleaning, as some coupons lost more Al coating than others. No general corrosion can be noticed on the Al cold spray coated AZ31B coupons surface as compared to the bare AZ31B coupons (Figure 4.2) and this indicate that the Al coating layer was protective to the base Mg substrate. This is consistence with what has been reported about corrosion mechanism of Al, as in aqueous solution a dense and strong oxide film will developed on the surface of the Al substrate that provide good corrosion resistance to the Al substrate [32]. For Mg alloys and in aqueous solution, the developed oxide or hydroxide film is normally known to be porous and loose which will not provide the Mg substrate with the necessary protection and results in the linear increase in the corrosion rate, pits size and surface roughness.

Cycle # (days)	Average weight loss per surface area (grams/mm ²)	Standard deviation
3	0.2148	0.0636
6	0.2747	0.0106
9	0.8135	0.5091
12	1.0935	0.5869
15	1.1235	0.7071

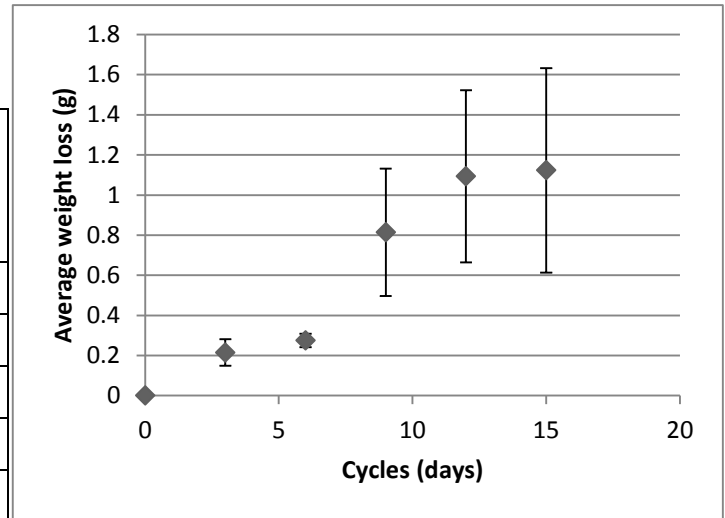


Figure 4.10: Average weight loss versus the number of tested cycles for coated coupons

Figure 4.11 shows the average roughness measurements for the coated coupons before and after the corrosion testing. As was done for the bare AZ31B coupons, few thousand measurements were taken in both longitudinal and transverse directions and the average of these reading was considered. As shown in the chart, the roughness of both directions looks to be more or less constant, indicating no sign of severe general corrosion on the surface.

Cycle # (days)	RA Longitudinal direction (μm)	RA Transverse direction (μm)
0	9.505	8.9525
3	10.1959	8.5225
6	11.1908	10.2565
9	9.3593	10.4428
12	10.9868	12.9273
15	10.562	13.328

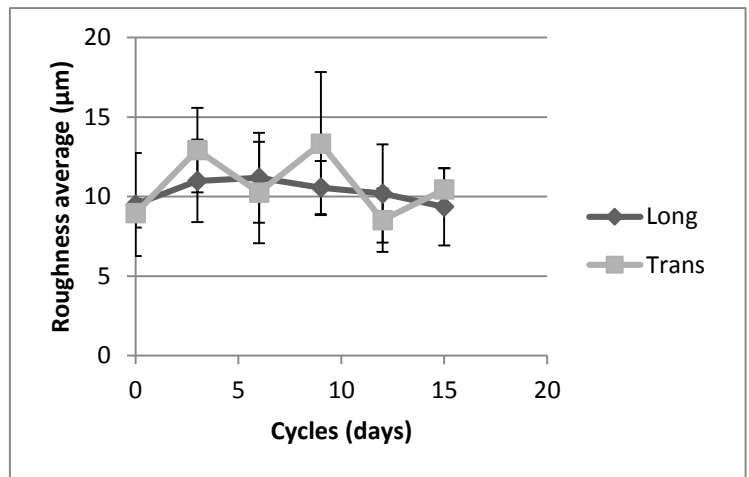


Figure 4.11: Average roughness measurements versus the number of tested cycles for coated coupons

Pit measurements (size and depth) for the coated coupons were also studied by means of an optical microscope and the Nanovea 3D Imaging equipment. Figure 4.12 shows typical sizes of the pits developed after every 3 cycles of exposure. As shown in the figure, the pit size increased as the number of cycles increased with the biggest pit measured at cycle 15 (Figure 4.12d). But from Figure 4.13 which shows the changes in average pit diameter over the 15 days of exposure, it seemed after 12 cycles there was no further pit growth.

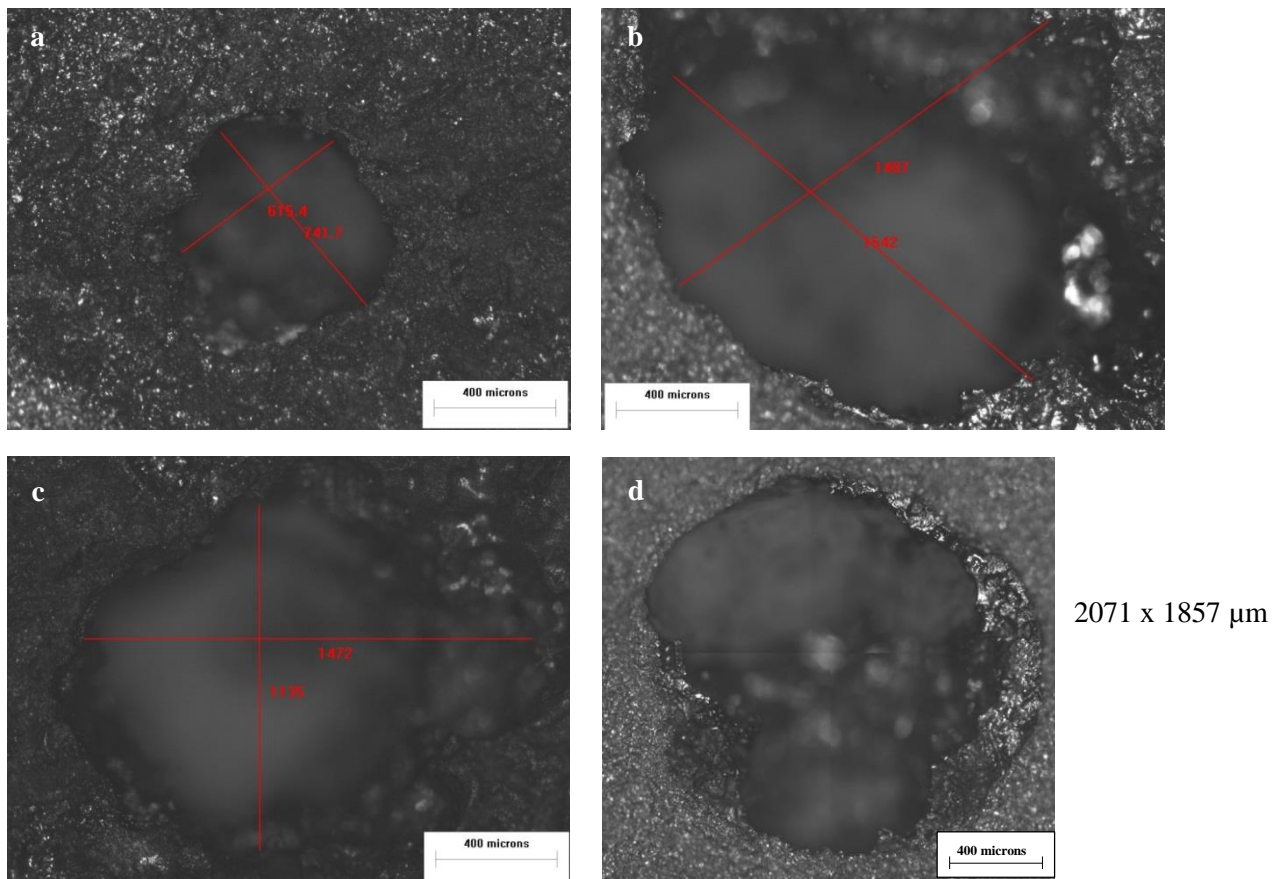


Figure 4.12: Typical sizes of the pits in coated coupons after: (a) 9 cycles, (b) 9 cycles, (c) 12 cycles, and (d) 15 cycles

Cycle # (days)	Average pit diameter (μm)	Average # of pits per unit area (pits/ mm^2)
3	0	0
6	0	0
9	1218.03	4
12	1448.5	4
15	1418.5	7

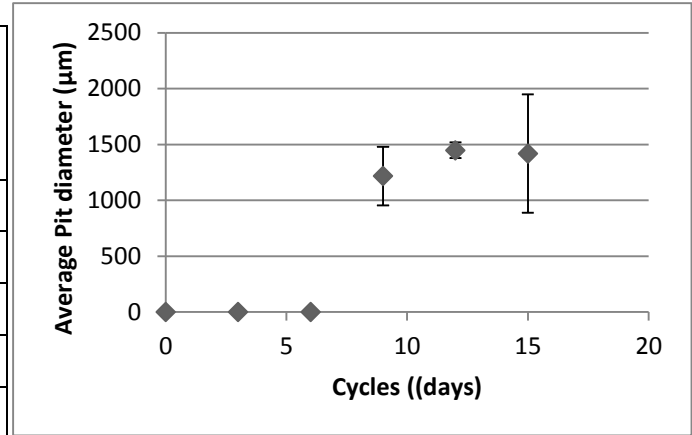


Figure 4.13: Average pits size versus the number of tested cycles

The pit depth studies are presented in (Figure 4.14) in which the average pit depth over exposure time seems to follow a linear trend after cycle 6. From cycles 9 to 15, the pit depth trend was increasing at a slower rate than from cycles 6 to 9.

Cycle # (days)	Average pits depth (μm)	Average # of pits per unit area (pits/ mm^2)
3	0	0
6	0	0
9	205	4
12	220	4
15	250	7

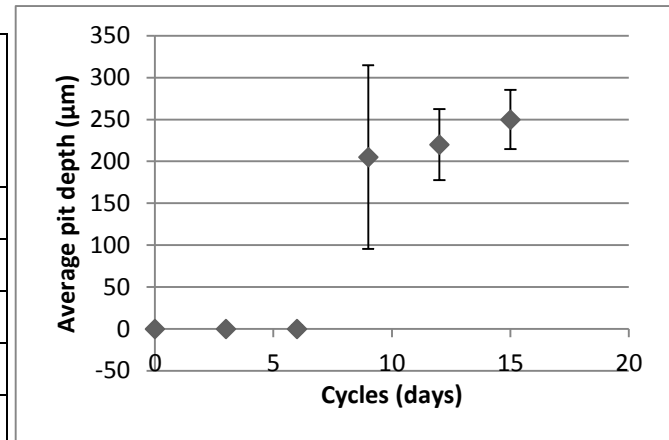


Figure 4.14: Average pit depth versus the number of tested cycles for coated coupons

After comparing the first corrosion testing results for bare and coated AZ31B specimens, it can be said that there was a clear evidence that Al cold spray provided some sort of protection to the Mg substrate since no general corrosion appeared on the Al coated AZ31B coupons surfaces as the case with the bare AZ31B. However, it was not possible to reach to a solid conclusion regarding the benefits of applying Al cold spray coating to Mg alloy AZ31B in an effort to increase its corrosion resistance due to the unexpected findings (e.g., peeling off of the coating). Due to this, it was decided to perform another standardized corrosion test at the CanmetMATERIALS facilities.

4.2 CanmetMATERIALS Corrosion Testing Results

Bare and Al cold spray coated coupons shown in Figure 3.4 above were exposed to continuous salt fog environment in this testing. The temperature in the chamber was maintained between 36-37°C during the test while the temperature in the humidifying tower was maintained at 47°C. The salt solution container had a capacity of 60 liters and it was regularly filled with fresh 5% NaCl with a pH between 6.5 to 7.2. A pH measuring tool was used to measure the prepared solution pH and buffer solutions were used for calibrating the pH tool before any use. Addition of some acid (10% HCl) or base (Sodium hydroxide) was necessary from time to time in order to adjust the pH of the salt solution to be within the recommended value. Fog was collected with a fog collector in the vicinity of the specimens periodically to ensure that the fog quantity is within the range of 1.0-2.0 mL per hour per 80cm² as per ASTM B117 standard. An air-purge valve controlled the amount of fog in the chamber. All testing coupons were placed at angles of 15-20° from vertical line in the chamber rack during the testing as shown in Figure 4.15. Prior to the corrosion test, the specimens were cleaned in acetone, dried with warm flowing air and weighed.

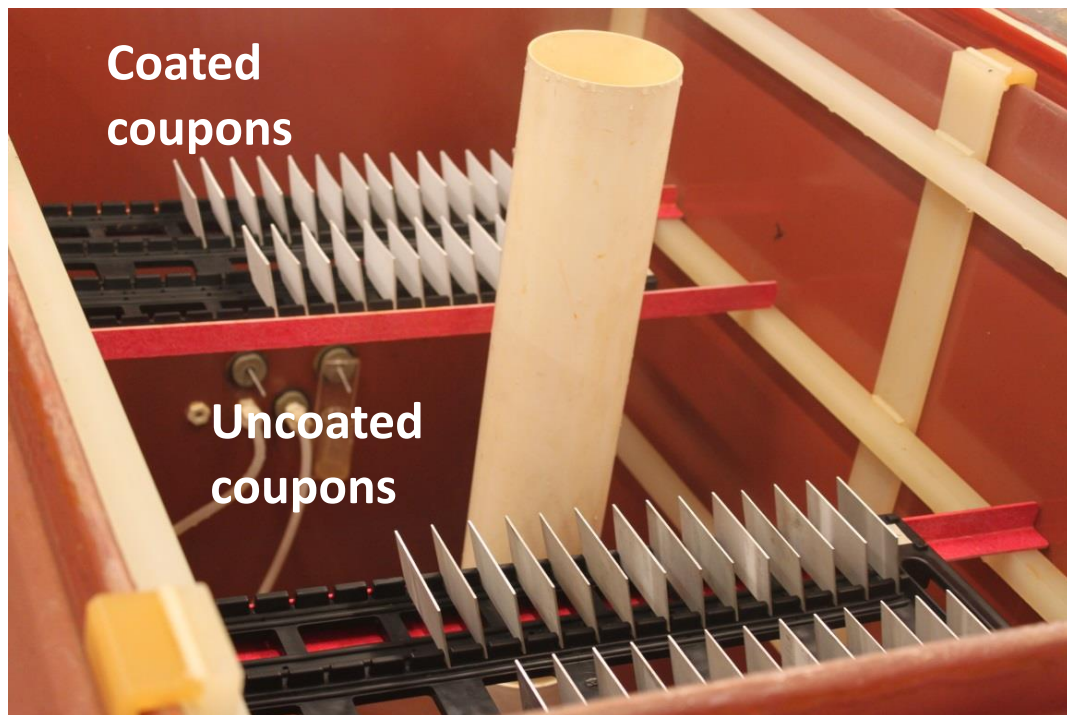


Figure 4.15: The testing coupons (coated and uncoated) distributed in the rack before testing

Since the thickness of the testing coupons for this experiment was very small ≈ 1.6 mm, the Al cold spray coating could not be applied at the coupon edges. For this reason, a way of protecting the edges needed to be found. Microstop lacquer mask (Figure 4.16) was applied on all coated coupon edges in order to prevent any contact between the electrolyte (salt fog) and the uncoated edges. Both types of coupons were examined at the same time but the exposure duration is varied as described below.



Figure 4.16: The applied mask used for protecting the edges of coated coupons

4.2.1 Bare AZ31B Coupons Corrosion Testing

Twenty-seven uncoated Mg alloy AZ31B coupons were tested in the CanmetMATERIALS corrosion chamber using the parameters outlined in Chapter 3. The coupons were tested in the salt spray chamber for a duration of 33 cycles (days) with removal frequency of 3 coupons every 3 cycles (days) of testing except for some cycles. Figure 4.17 shows the macrographs of the uncoated coupon surfaces after the 5% salt spray exposure over the 33 cycles.

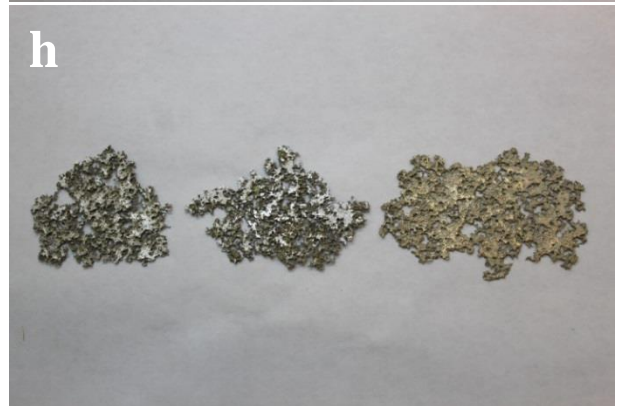
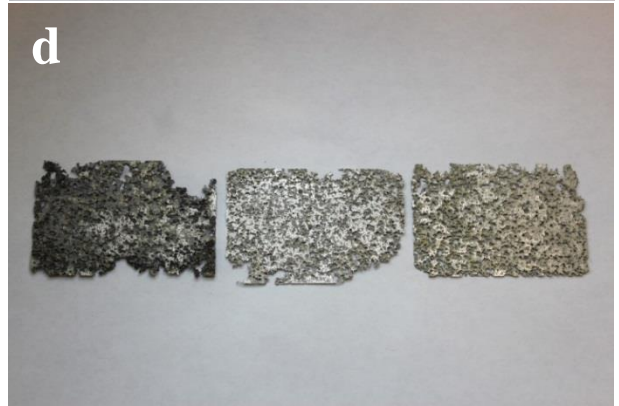
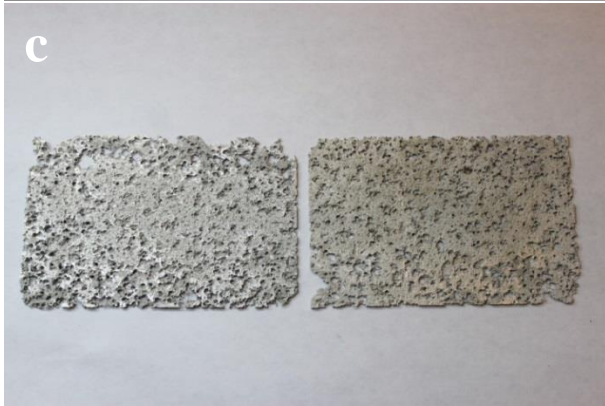




Figure 4.17: Uncoated coupons exposed to 5% salt spray after: (a) 4 cycles, (b) 6 cycles, (c) 8 cycles, (d) 11 cycles, (e) 14 cycles, (f) 17 cycles, (g) 20 cycles, (h) 23 cycles, (i) 26 cycles, and (j) 33 cycles

By visual examination of the tested coupons, it can be seen that the 5% NaCl continuous fog environment had a significant impact on the bare Mg alloy AZ31B, resulting in a great amount of material loss. This is due to the fact that Mg is a very reactive metal in aqueous environments and even more reactive in salt- water environment in which it is displaying a very high anodic standard electrode potential of around -2.36 V [93]. The observed corrosion mechanisms are general and pitting corrosion. Corrosion pits and material perforations were revealed in the first coupons inspected after 4 days of testing. The corrosion attack continued during the testing period and almost no material was left at the end of the 33 cycles (days) of testing. Table 4.1 summarizes the weight measurement results and shows the average weight loss of the uncoated coupons. The average weight loss of coupons in grams per cycle, versus the number of testing cycles, was graphed (Figure 4.18) and as one can see, the weight loss due to corrosion follow increasing linear trend through the testing period. From cycles 8 to 11 the loss in the corrosion rate seems to be slower a bit which could be attributed to the corrosion protection that the accumulated corrosion products provide to the substrate surface (Figure 4.19). After cycle 11, the corrosion rate increased again and was following linear increasing trend up to the end of the test at cycle 33.

Table 4.1: Uncoated coupons corrosion testing analysis

Cycle # (days)	# of coupons	Average weight before testing (g)	Average weight after testing (g)	Average weight after cleaning (g)	Average % weight loss	Average weight loss (g)
4	3	9.4769	17.7041	7.7712	18.0093	1.7069
6	1	9.4835	17.6198	7.6314	19.5297	1.8521
8	2	8.6404	21.2517	6.2845	27.2641	2.3560
11	3	8.8748	24.8327	6.0257	32.0779	2.8491
14	3	8.0783	20.7237	4.7944	40.6030	3.2839
17	3	8.2622	26.2321	4.6243	44.0047	3.6379
20	3	9.1767	17.4175	4.2239	54.0402	4.9527
23	3	8.9364	16.8824	2.5796	71.0985	6.3569
26	3	8.8378	13.7876	2.1109	76.2546	6.7269
33	3	9.6187	9.8578	0.9657	89.9627	8.6530

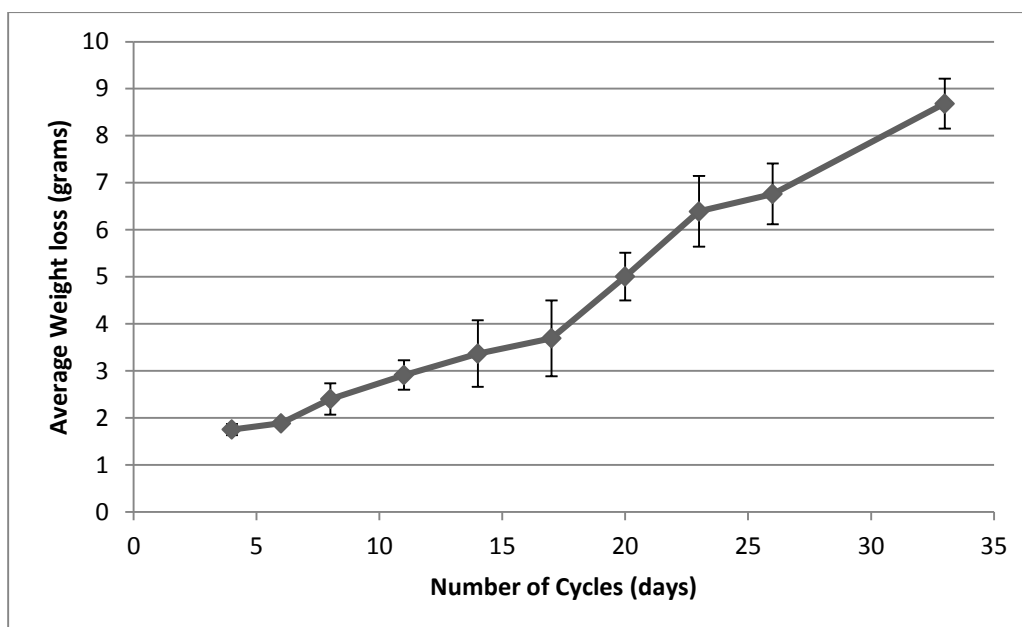


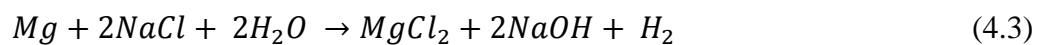
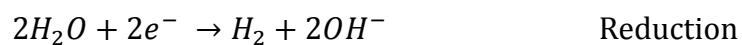
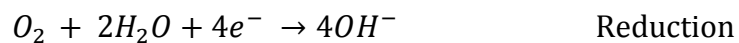
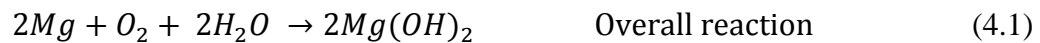
Figure 4.18: Average weight loss versus the number of tested cycles for bare AZ31B coupons



Figure 4.19: Corrosion products accumulated on a bare coupon after 6 days of testing

Since the testing environment in this test was in salt-water environment, the standard oxidation/reduction reactions can't be considered as the only explanation for the corrosion of Mg. And this is because Mg corrosion in aqueous environments will proceed due to the presence of water and sodium chloride by an electrochemical reaction.

Three oxidation/reduction reactions can be expected in this testing, as shown below [93]:



The general and pitting corrosion morphology and severe weight loss shown in Figure 4.2 and Figure 4.17 can be directly contributed to the oxidation/reduction reactions described in equations 4.1-4.3. However, the following factors were also playing important roles in this corrosion mechanism:

- The formed magnesium chloride salt from (Eq. 4.3) react with the naturally formed $\text{Mg}(\text{OH})_2$ film and weakens it [93]. This explains the fact that the corrosion morphology of the CanmetMATERIALS testing coupons (Figure 4.17) was more severe than those tested at UW (Figure 4.2). The reason for this is that the cyclic corrosion testing used in the UW which includes the chloride-free humidity phase, allows the formation and rebuilding of the $\text{Mg}(\text{OH})_2$ film that was damaged during the salt exposure phase and this will reduce the corrosion attack on the surface [93]. On the other hand, the CanmetMATERIALS testing coupons were exposed to a continuous salt spray with a concentration of 5% NaCl. This will not allow the Mg substrate to form the $\text{Mg}(\text{OH})_2$ film as it will be continually dissolved due to the reaction with magnesium chloride salt [93],[94].
- The presence of the chloride ions in the tested environment accelerates the corrosion rate. Once pits initiated on the surface, the pit debris and the trapped chloride ions will cause pitting growth deeper and wider but with increasing the exposure time, they will affect in slowing the reaction rate [94].
- The other very important factor is the role of the microstructure, grain size, secondary phases and their distribution. The grain boundaries and secondary phases have micro-galvanic cathode effect on the Mg matrix in the alloy [27].

To have a better understanding of these effects, multiple cross sections from the coated and uncoated coupons before and after the corrosion were prepared for metallographic examination. Figure 4.20 shows the microstructure in the as-etched condition (etched in a solution of 10 ml acetic acid, 4.2 g picric acid, 10 ml H_2O , and 70 ml ethanol [95]). Figure 4.20a shows the general microstructure, grains distributions and volume distribution of the secondary phases near the α -Mg grain boundaries. Deformation twins were observed in Figure 4.20b. Several big shiny particles were observed in Figure 4.20b, c and d in addition to numerous small grey/black spherical particles distributed along the surface.

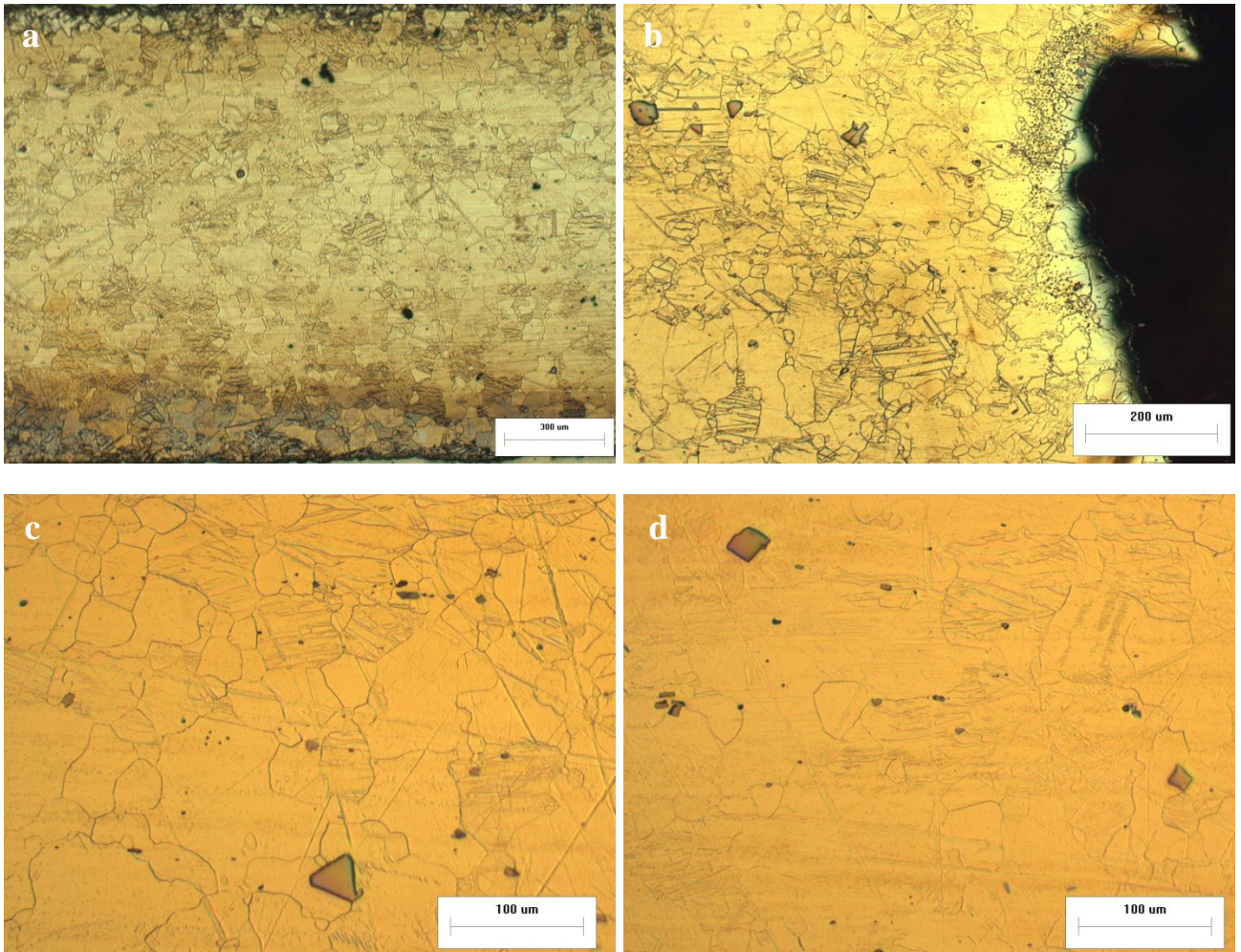


Figure 4.20: Optical cross section micrographs showing the microstructure of AZ31B as (a) coated coupon after 11 cycles of corrosion testing, (b) uncoated coupon after 8 cycles of corrosion testing, (c) coated alloy before corrosion testing, and (d) uncoated alloy

Scanning Electron Microscope and Energy Dispersive X-ray (SEM/EDX) analysis for these secondary phases were performed. Figure 4.21 is a low magnification SEM image shows the distributions of these particles on the surface from which it can be seen that volume fraction of the secondary phases is considered as low when comparing with typical secondary phases distribution graphs [95]. EDX analysis for these particles (Figure 4.22) revealed the presence of Mg-Al-Mn compounds (Figure 4.22a) and Al-Mn compound (Figure 4.22b). The β -phase $Mg_{17}Al_{12}$ was not recognized by EDX analysis and this could be attributed to the low content of Al in the AZ31B alloy or due to its small size which make it hard to see under SEM and EDX analysis.

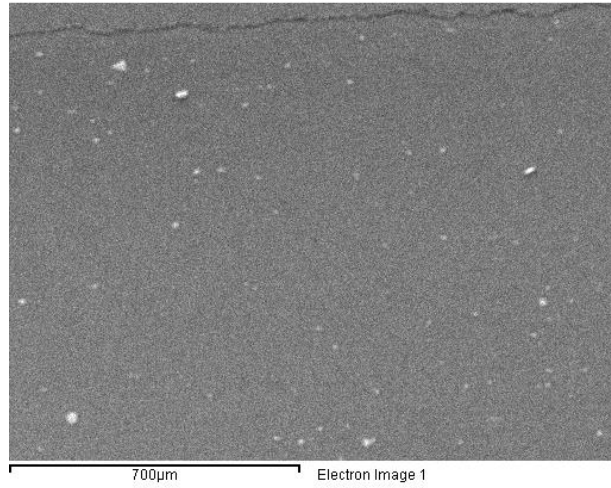
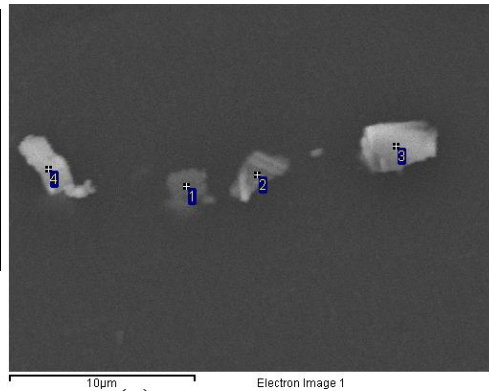


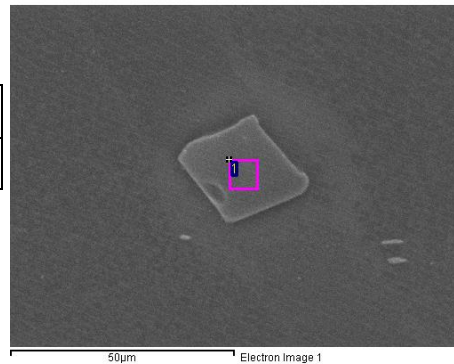
Figure 4.21: SEM image showing the distributions of particles

Spectrum	Mg	Al	Mn
1	69.90	13.03	17.07
2	63.25	20.31	16.44
3	40.71	34.49	24.80
4	49.73	32.26	18.01



(a)

Spectrum	Al	Mn
1	22.6	77.4



(b)

Figure 4.22: Energy dispersive X-ray analysis of the detected particles as (a) Mg-Al-Mn secondary phase, and (b) Al-Mn secondary phase

The presence of the second phases in the microstructure of Mg-Al alloys could have two effects on the corrosion behavior of the alloy in an NaCl environment depending on the Al content in the alloy, the volume fraction and the distribution of the second phases in the microstructure [27],[94]. The second phase could act as a barrier, or as a galvanic cathode in which the α -Mg is the galvanic anode. AZ91, for example, contains a large volume of β -phase ($Mg_{17}Al_{12}$) precipitate along the grain boundaries due to the high amount of Al in the alloy. In an NaCl environment, the β -phase will coalesce and work as a barrier and inhibit the corrosion of the AZ91 alloy surface as explained in the schematic presentation in Figure 4.23 [27],[94].

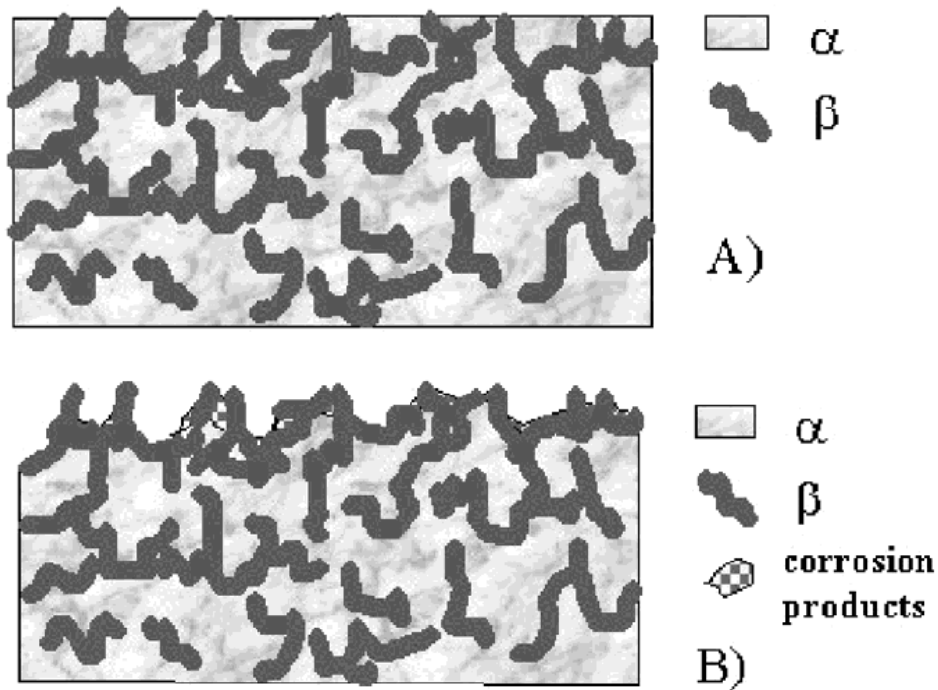
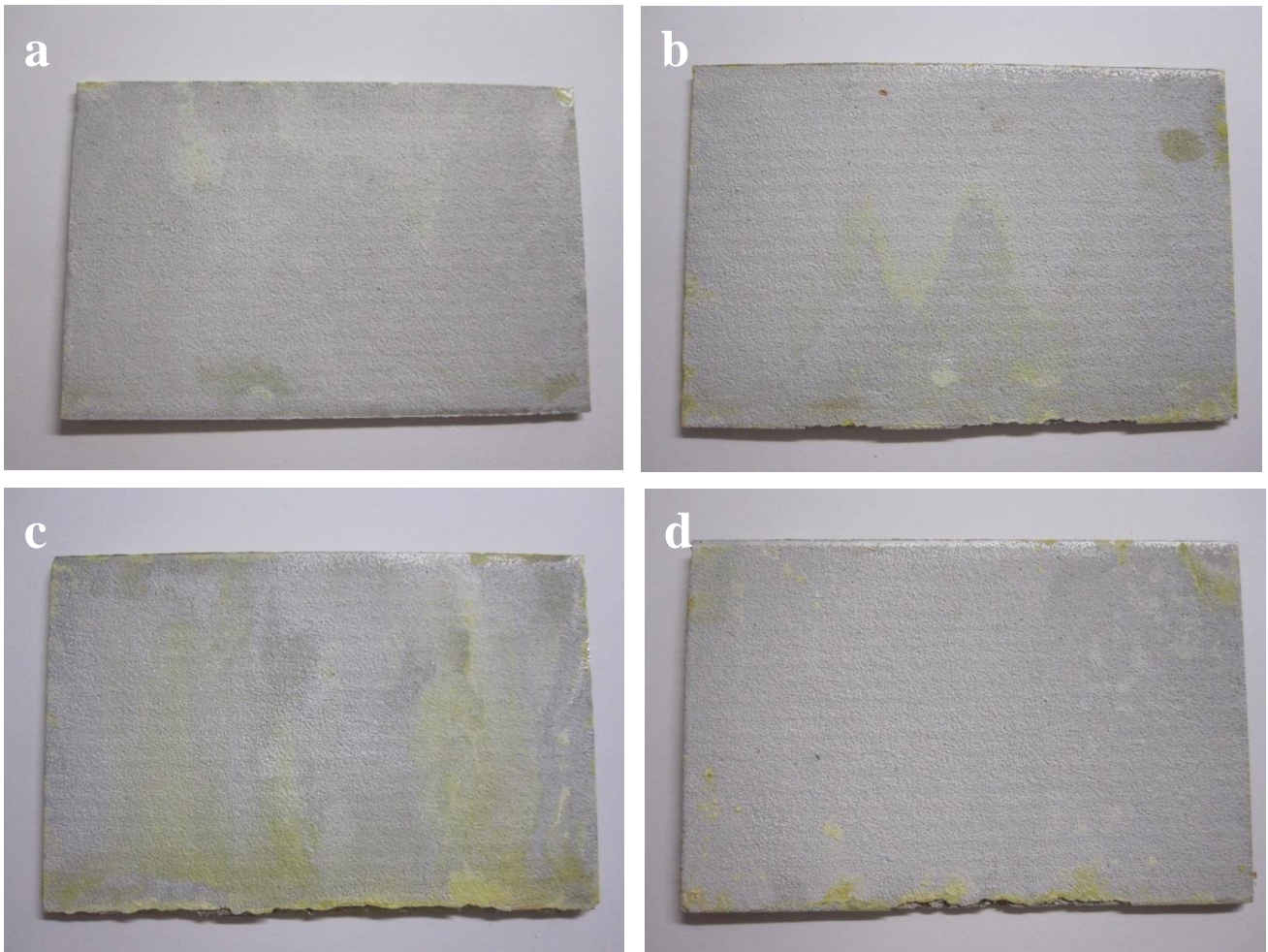


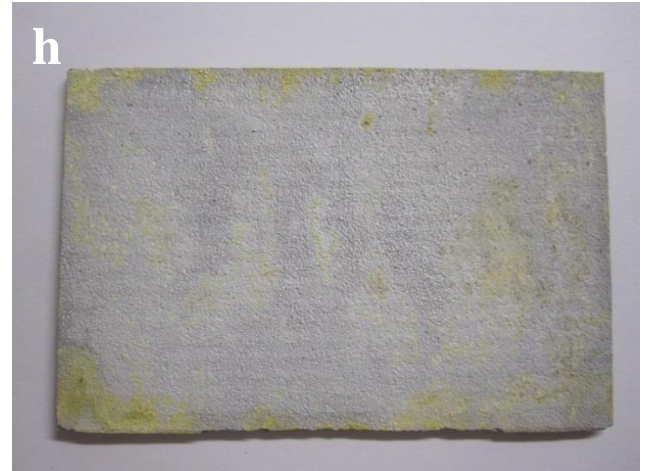
Figure 4.23: Schematic of the role of the β -phase on corrosion: (a) initial surface and (b) surface after corrosion [27]

The secondary phases and the grains boundary also act as galvanic cathodes to the α -Mg matrix; this tends to occur in Mg-Al alloys with lower amounts of Al. In our case study, AZ31B alloy is a typical example of this. Because the alloy contains less Al than AZ91, it has a small volume fraction of second phases (shown in Figure 4.22) and these second phases acted as galvanic cathodes to the α -Mg matrix and increased the corrosion rate. This fact also explains the general and pitting corrosion morphology of the tested bare AZ31B coupons in both corrosion testings Figure 4.2 and Figure 4.17.

4.2.2 Al Cold Spray AZ31B Coupons Corrosion Testing

A total of 20 coupons coated with cold sprayed Al powder were tested in the CanmetMATERIALS corrosion chamber under the parameters used for the bare coupons. Originally the full testing period was set to be 33 cycles (days) with the same removal frequency and analysis as the uncoated. However, at the first evaluation after 4 cycles it was observed that the coating was providing a very good corrosion protection and the Mg substrate is totally isolated except from minor areas at the edges where no Al coating could be applied. So it was decided to lower the number of coupons removed for testing and to increase the testing duration up to 90 cycles (days) in order to get a better idea about the corrosion behavior of the coated coupons and the effect of the Al cold spray coating on corrosion protection over a long exposure time. Figure 4.24 shows the macrographs of the coated coupon surfaces after 5% salt spray exposure for 90 cycles.





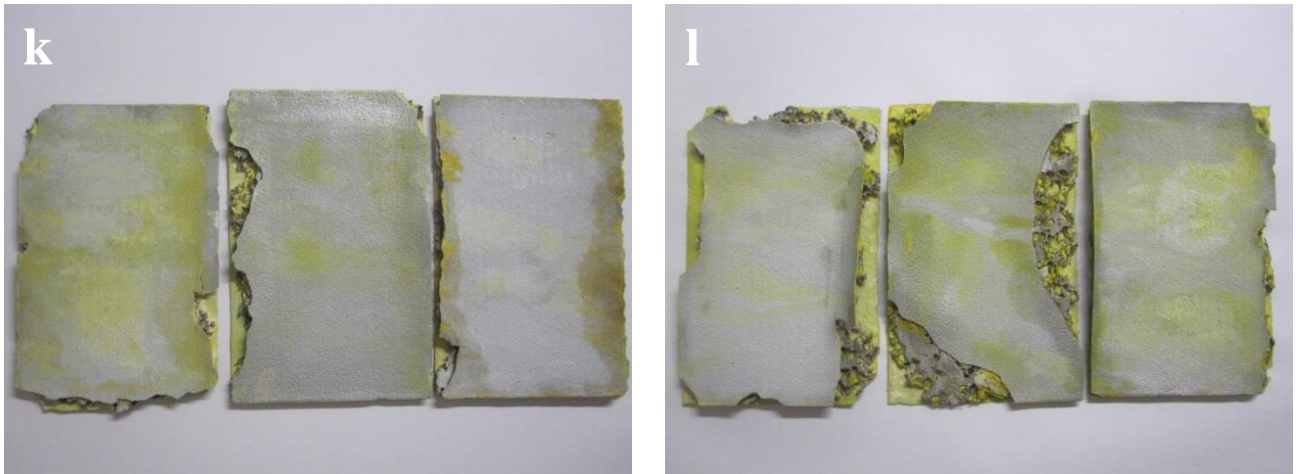


Figure 4.24: Coated coupons exposed to 5% salt spray after: (a) 4 cycles, (b) 8 cycles, (c) 11 cycles, (d) 14 cycles, (e) 17 cycles, (f) 20 cycles, (g) 23 cycles, (h) 26 cycles, (i) 33 cycles, (j) 40 cycles, (k) 60 cycles, (l) 90 cycles

Visual examination of the tested coupons revealed that the Al cold spray coating has provided considerable corrosion protection for the AZ31B substrate as compared to the bare coupons. No corrosion pits were noticed on the surface of any of the tested coupons after chemical cleaning. The corrosion attack on the coupons took place only from the edges that were not cold spray coated. Although the edges were protected (by the lacquer mask explained earlier), swelling and peeling of this mask coating was observed as shown in Figure 4.25. This may have occurred because the applied mask coating was not sufficient for such a harsh environment. The peeling off of the mask coating allowed the salt to penetrate to areas of uncoated substrate and corrosion proceeded from these areas. This edge corrosion attack grew as the number of cycles increased and once the Mg substrate was corroded, the thin Al coating layer broke due to the arrangement of the coupons in the chamber rack, handling and cleaning (Figure 4.26). At the 40, 60 and 90 cycle testing points, the corrosion behavior of the three replicates was not the same; some coupons experienced less corrosion attack than others which may have been due to inconsistent application of the edging mask (some had received greater coverage).

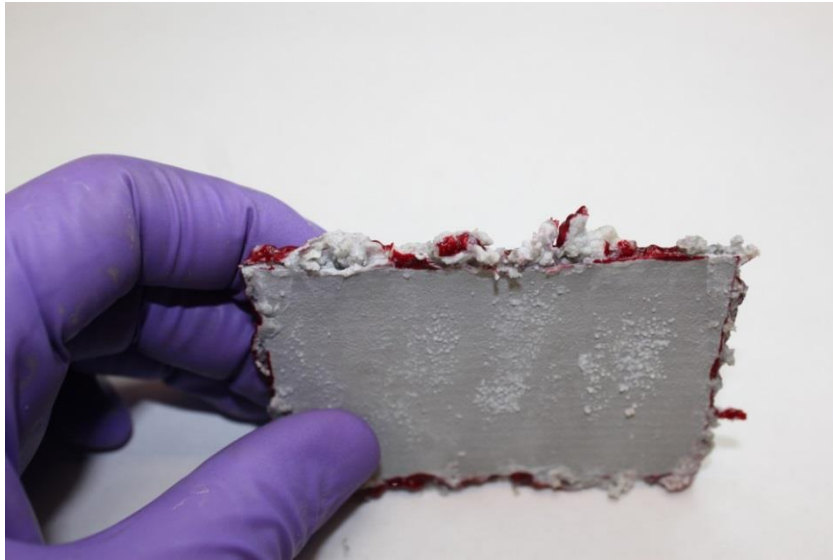


Figure 4.25: Corrosion products accumulated on a coated coupon after 8 days of testing

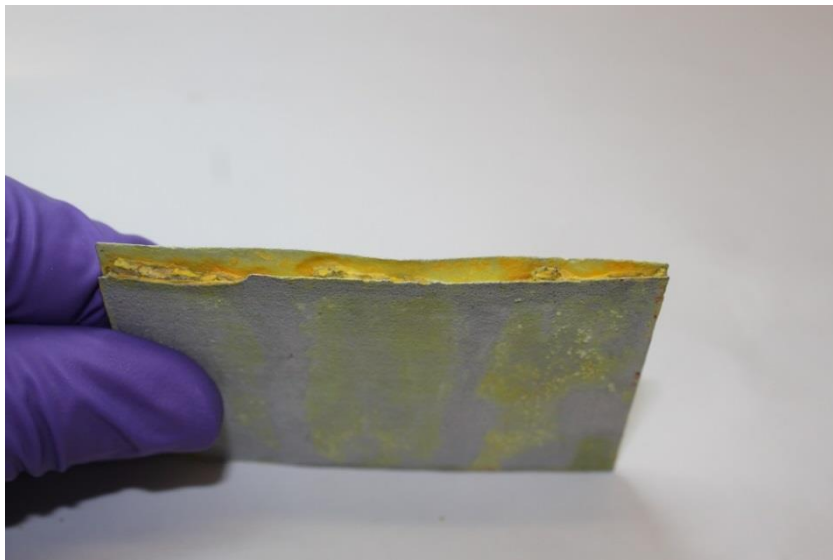


Figure 4.26: Coated coupon after cleaning/removing edges corrosion products, 40 days of testing

Table 4.2 outlines the weight measurement results and shows the average weight loss of the coated coupons. The average weight loss of the coupons in grams versus the number of testing cycles is graphed in Figure 4.27. There is no clear pattern in the corrosion results due to the variation in the corrosion attack at the edges from coupon to another. This can be clearly seen by reviewing Figure 4.24 k and l, showing the different levels of corrosion attack for the three replicate coupons. This also explains the large variability in the chart at cycles 60 and 90.

Table 4.2: Coated coupons corrosion testing results

Cycle # (days)	# of coupons	Average weight before testing (g)	Average weight after testing (g)	Average weight after cleaning (g)	Average % weight loss	Average weight loss (g)
4	3	16.0963	21.3093	16.0855	0.0670	0.0108
8	1	15.3591	19.8841	15.3411	0.1172	0.0180
11	1	16.6767	21.9138	16.6120	0.3880	0.0647
14	1	16.2688	22.3497	16.1093	0.9804	0.1595
17	1	15.5550	19.4187	15.4110	0.9257	0.1440
20	1	15.2438	20.1474	15.1367	0.7026	0.1071
23	1	16.4659	22.8461	16.3351	0.7944	0.1308
26	1	15.0811	20.7144	14.9443	0.9071	0.1368
33	3	15.29735	19.1666	15.1233	1.1378	0.1741
40	3	15.7930	19.9679	15.5761	1.3736	0.2169
60	3	15.6458	20.8080	14.7507	5.7439	0.8951
90	3	16.0138	21.1169	14.5946	8.9304	1.4192

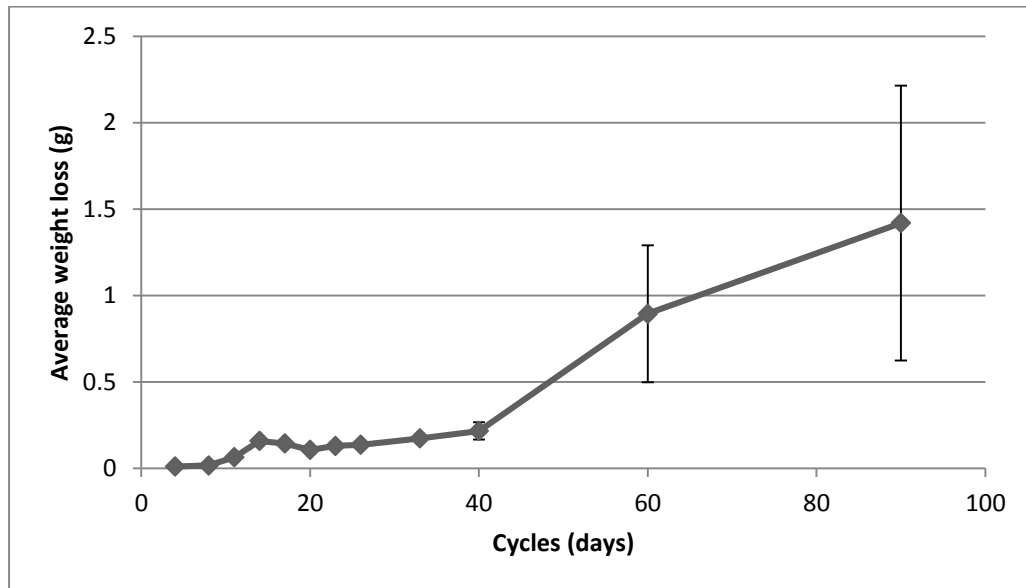


Figure 4.27: Average weight loss versus the number of tested cycles for coated coupons

When comparing Figure 4.18 and Figure 4.26 which represents the average weight loss for the bare and Al cold spray coated AZ31B (Figure 4.28), one can see that obviously the Al cold spray coating improved the corrosion protection for the bare AZ31B.

The salt spray chamber test environment in some sense mimics the automotive service condition. The corrosion testing results showed that under such environment, the Al cold spray coating was able to provide enough corrosion protection of the Mg alloy, if the coating integrity is not damaged.

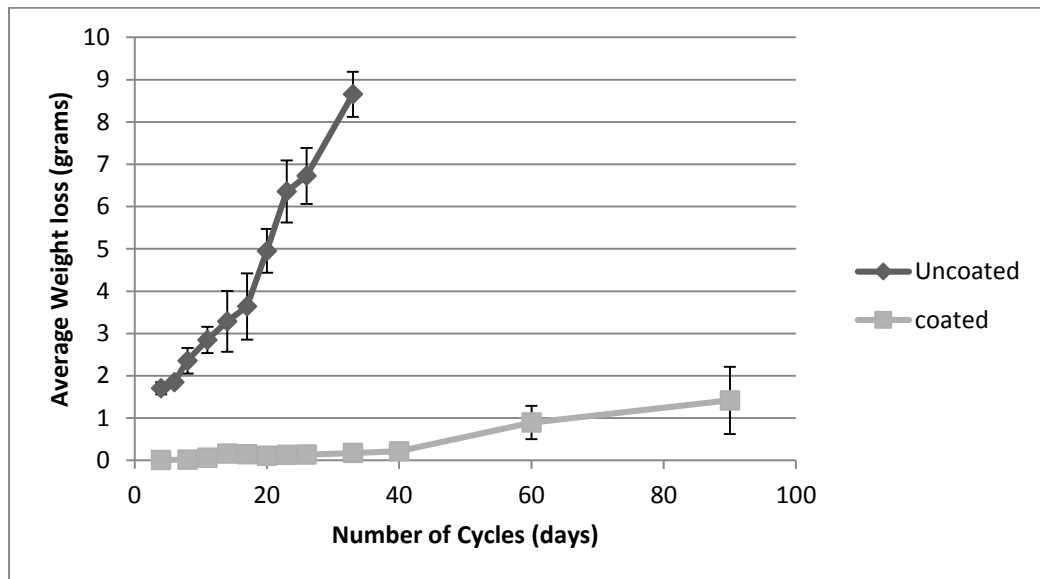


Figure 4.28: Average weight loss versus the number of tested cycles for bare and coated coupons

Surface characterization and topographic analysis for the coated coupons was performed with AltiSurf® 500, but such measurements could not be performed on the uncoated coupons as the corrosion was so severe. Figure 4.29 represents an example of the scanning surface result in which an area of 70 mm x 45 mm was scanned and the root mean square shown in the table (Figure 4.29a) is represents the surface average roughness. 3D image for the scanned surface also given in Figure 4.29b. The surface roughness of each coated coupon was measured before and after the corrosion testing in order to examine the surface roughness behavior. All of the coupons' roughness measurement results are given in Appendix A. The average roughness measurements for the coated coupons before and after the salt spray exposure are summarized in Table 4.3.

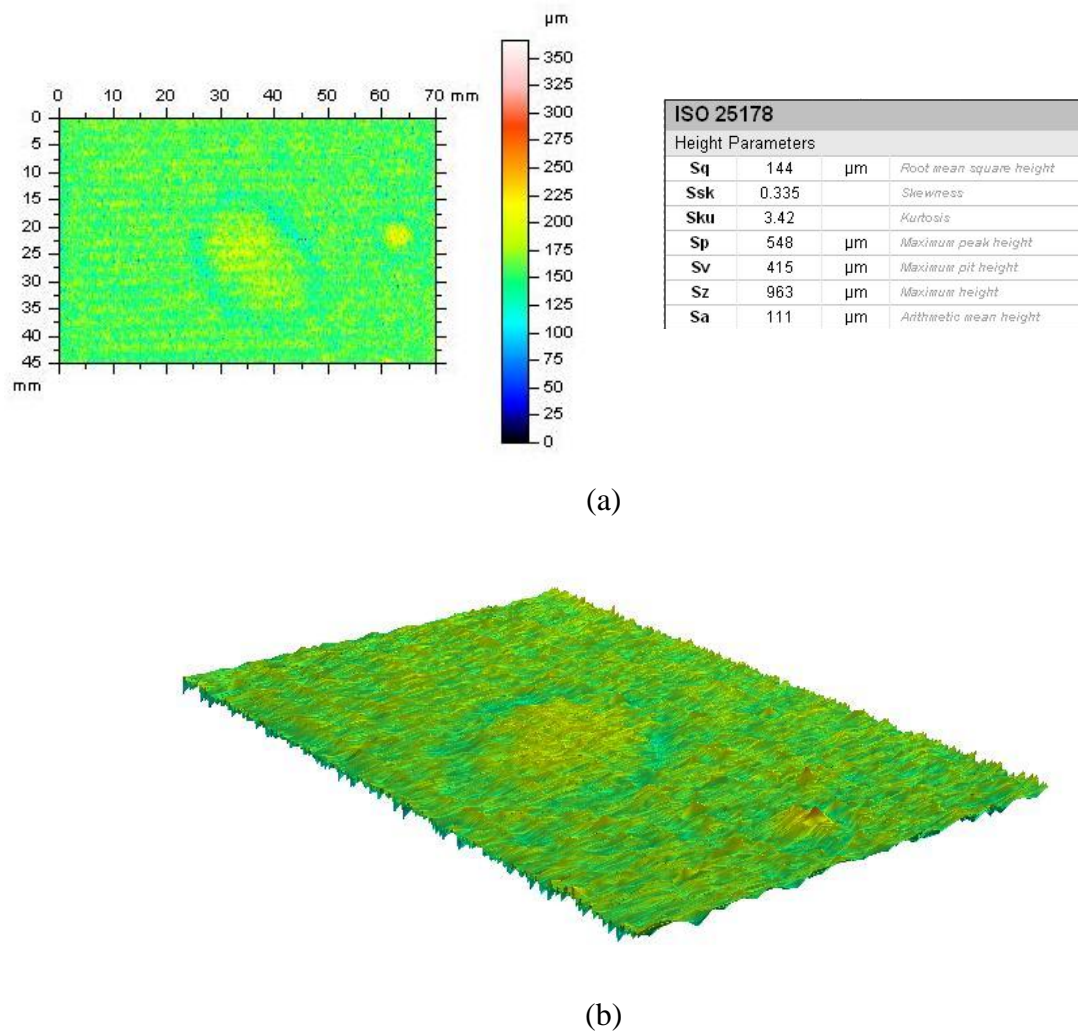


Figure 4.29: Surface roughness analysis of coated AZ31B coupons performed by AltiSurf® 500 showing (a) roughness parameters and (b) surface 3D image

Table 4.3: Coated coupons' surface roughness analysis

Cycle # (days)	# of tested coupons	Surface Roughness Average before testing (μm)	Surface Roughness Average after testing (μm)	Percentage change in surface roughness (%)
4	1	150	215	43
8	1	183	288	57
11	1	146	259	77
14	1	165	300	82
17	1	133	221	66
20	1	187	250	33
23	1	176	269	52
26	1	144	204	42
33	3	172	351	104
40	3	170	398	134
60	3	154	462	200
90	3	163	702	331

As shown in the table, the surface roughness for the Al cold spray coating before the corrosion testing was ranged between 133-187 μm and this variation is most likely attributed to the cold spray coating process with stepover, stand off distance and variation of Al powder size. The change in the surface roughness before and after the corrosion testing is better explained at Figure 4.30 from which one can see that the percentage change in the surface roughness up to cycle 26 was not steady and this was due to the variation in the edges protection quality. From cycle 33 up to the end of the test at cycle 90, the percentage change follows linear trend due to the continuous falling off the Al coating and corrosion of Mg substrate.

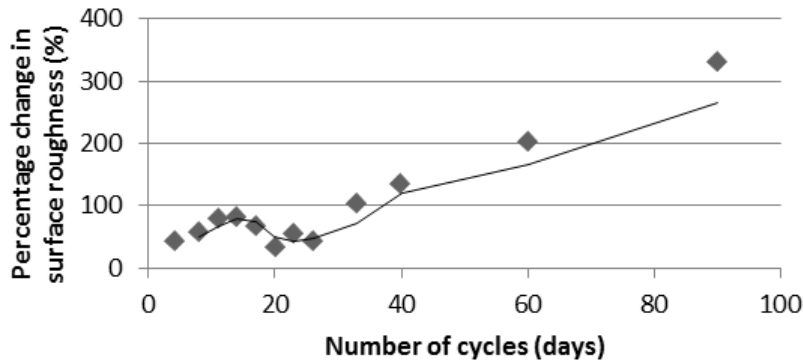


Figure 4.30: Percentage change of coated coupons surface roughness after corrosion testing

4.3 Corrosion Fatigue Testing

Corrosion fatigue experiments were performed on the extruded Mg alloy AZ31B on an RBM at room temperature and at a frequency of 30Hz. The composition of the electrolyte was 3.5% NaCl solution at room temperature. The cylindrical hourglass specimens (Figure 3.8) were used to identify the corrosion fatigue life at different stress levels. Two groups of stress-relieved specimens were tested: Al cold spray coated and uncoated AZ31B. The experiment was carried out while dripping the 3.5% NaCl solution onto the specimen gauge surface. The flow rate of the salt solution was adjusted to be 40 ml/min and was controlled through two valves. This flow rate was enough to cover the tested specimens' gauge surface with a film of NaCl solution during the testing period. The used salt solution was drained and discarded and the salt solution tank was filled with fresh sodium chloride solution regularly.

The predetermined stress in this test can be achieved by adding a calculated load to the machine weight pan. The required weight was calculated through the following formula [89]:

$$S = \frac{16WL}{\pi D^3}$$

Where S = tested stress (PSI), W = total load on specimen (pounds), L = moment arm (distance from end support to load point) which was always kept = 0.157 mm, and D = minimum diameter of specimen (mm) [89].

During the test, some of the specimens did not fracture in the gauge neck as expected but fractured at the end edges of grip area due to corrosion of the Mg alloy occurring between the specimen and the RBM bearing housing collets followed by failure from that area. These data were not counted in the study. To prevent such a corrosion reaction in subsequent tests, a silicon resin was applied to the specimen's surface edges outside the gauge area.

Table 4.4 below provides the data obtained from the fatigue tests, and Figure 4.31 shows the S-N curve for the two groups of specimens. For comparison purposes, and to provide a better understanding of the effect of the corrosive environment on the fatigue life of the AZ31B, results from fatigue testing of AZ31B in air collected by a colleague in our group [96] were reported in Table 4.5 and Figure 4.32.

Table 4.4: RBM corrosion fatigue testing results in 3.5% NaCl solution

Uncoated			Coated		
Load (Kg)	Stress (MPa)	N (Cycles)	Load (Kg)	Stress (MPa)	N (Cycles)
8.109	120	83,479	8.109	120	10,319
6.757	100	112,048	6.7579	100	28,280
6.081	90	97,505	6.0819	90	69,847
5.744	85	372,669	5.406	80	82,981
5.406	80	251,539	5.406	80	87,516
5.406	80	494,127	5.00	74	383,025
5.00	74	714,467	5.00	74	440,764
4.730	70	791,473	4.054	60	775,105
4.392	65	1,184,517	4.054	60	801,348
4.054	60	1,844,358	3.379	50	1,537,604
4.054	60	2,016,489	3.379	50	1,768,670
3.379	50	3,267,460	2.703	40	3,659,473
3.041	45	6,016,367	2.500	37	3,418,749
2.703	40	13,408,273	1.784	26.4	3,917,485

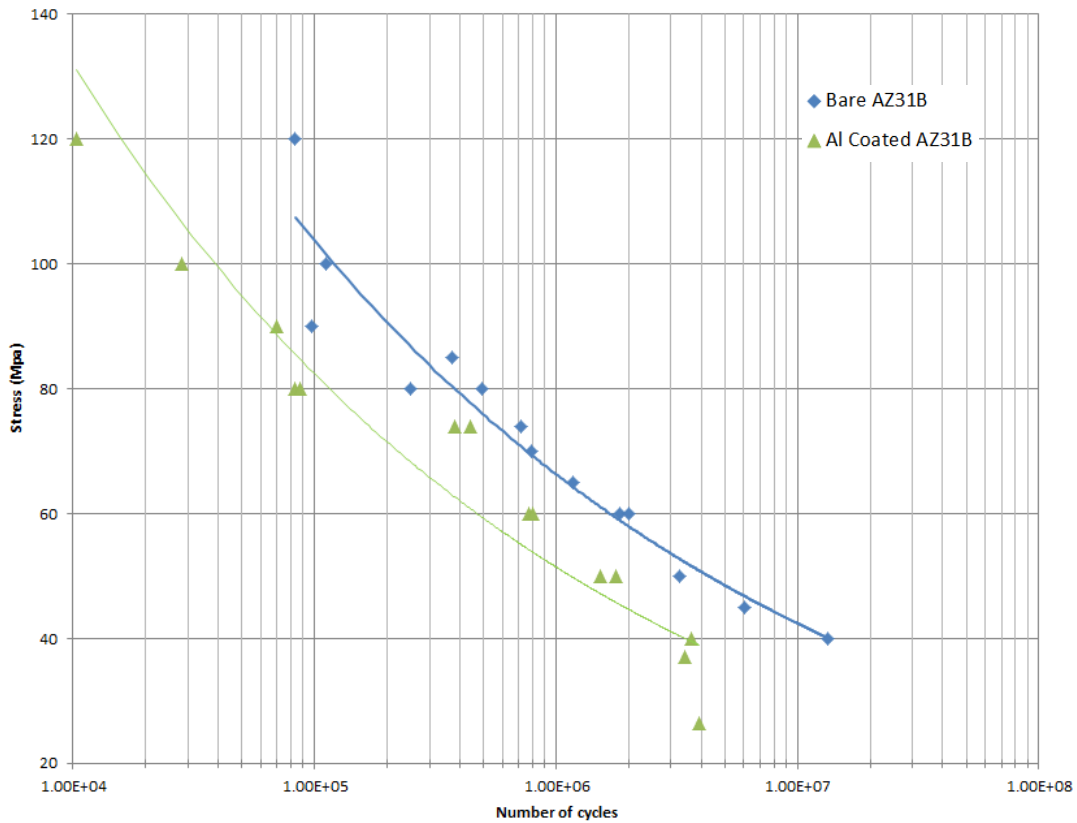


Figure 4.31: S-N curves of RBM testing for coated and uncoated specimens under NaCl environment

Table 4.5: RBM fatigue testing results for AZ31B in air [96]

Uncoated		Coated	
Stress (Mpa)	N (Cycles)	Stress (Mpa)	N (Cycles)
188	9,400	188	7,300
165	26,000	165	35,000
150	48,500	165	31,200
135	63,400	150	54,500
120	139,000	135	75,000
113	192,800	128	142,800
105	314,000	120	207,000
101	356,000	113	203,000
100	237,000	110	245,000
100	697,000	109	312,000
99	>10,000,000	108	>10,000,000

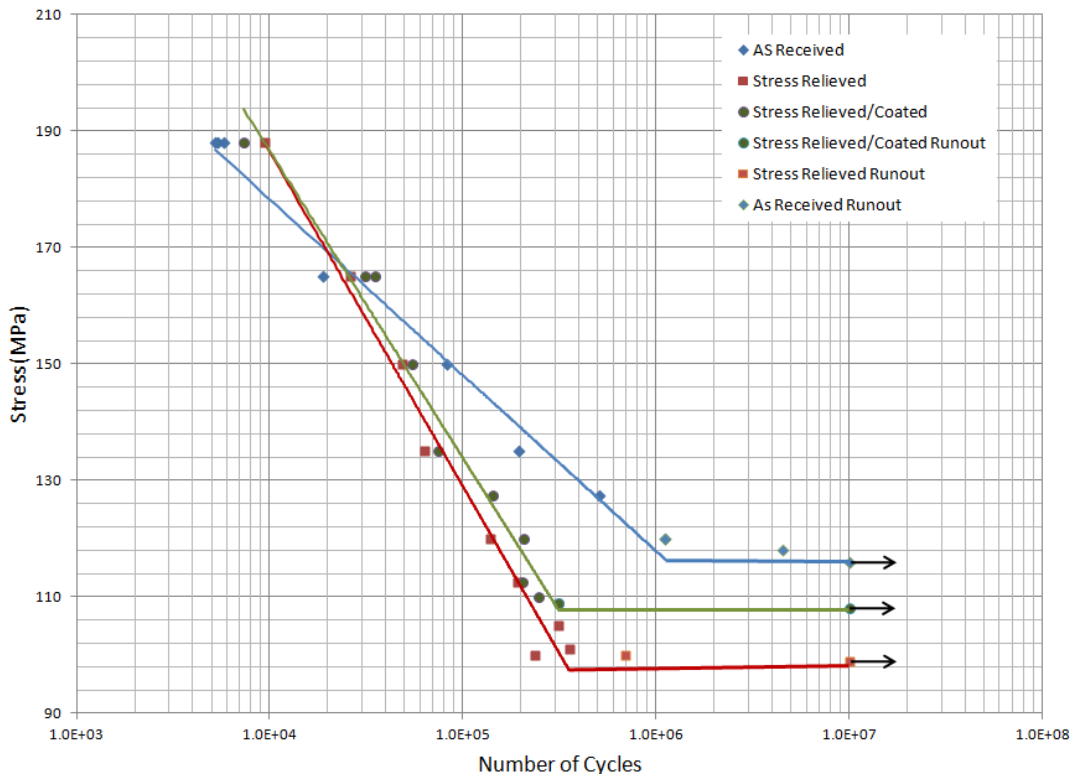


Figure 4.32: S-N curves of RBM testing for coated and uncoated specimens in air [96]

After comparing the two S-N curves (Figure 4.31 and Figure 4.32) for the fatigue behavior of AZ31B coated and uncoated samples, it can be observed that the corrosive environment (3.5 % NaCl) significantly decreased the fatigue life compared to an air environment and no endurance limit can be seen for both uncoated and coated coupons in the corrosive environment.

The fatigue life of AZ31B in air was related to the surface residual stress of the tested samples. Table 4.6 shows the values of the surface residual stress measured by X-ray diffraction (XRD) in addition to the endurance limit for the three types of specimens. It can be seen that there is a drop in fatigue life resulting from a loss of compressive residual stress after the stress relief. On the other hand, the fatigue life increased due to the residual stress induced by the cold spraying process due to peening effect.

Table 4.6: X-ray diffraction results on cylindrical specimens in air [96]

Group	Residual Stress on Surface (MPa)	Tolerance (MPa)	Endurance Limit (MPa)	Remarks
As Received	-43	+/-1	116	Measured on hourglass area
Stress Relieved	+11	+/-1	99	Measured on hourglass area
Stress Relieved/Coated	-22	+/-1	108	Measured on coated flat sample

Under the corrosive environment (3.5 % NaCl), the surface residual stress was not the main determinant of the fatigue life of the tested specimens as the cold spray coated specimens showed a drop in the fatigue life as compared with the uncoated specimens. The reason behind this drop is that the pure Al powder used in the cold spray process (SST A05011 with purity of 99.93%) has a much lower ultimate tensile strength (<100 MPa) than AZ31B (260 MPa), in addition to the fact that Young's modulus for pure Al (69 GPa) is higher than that for AZ31B (44.8 GPa). This mismatch in the mechanical properties between the applied Al powder and the AZ31B will result in the failure, in the form of cracking, of the Al coating at early stage of cyclic loading earlier than the AZ31B substrate during the fatigue testing. Once cracks have appeared at the surface of the Al coating, the corrosive media penetrated and reached the substrate causing localized corrosion due to the stagnancy of the solution at the substrate/coating interface. Figure 4.33 and Figure 4.34 supports the suggested failure scenario in which the cracking of the Al coating formed a path for the electrolyte to penetrate and reach the substrate AZ31B causing a concentrated corrosion cell that led to the fast failure of the AZ31B.

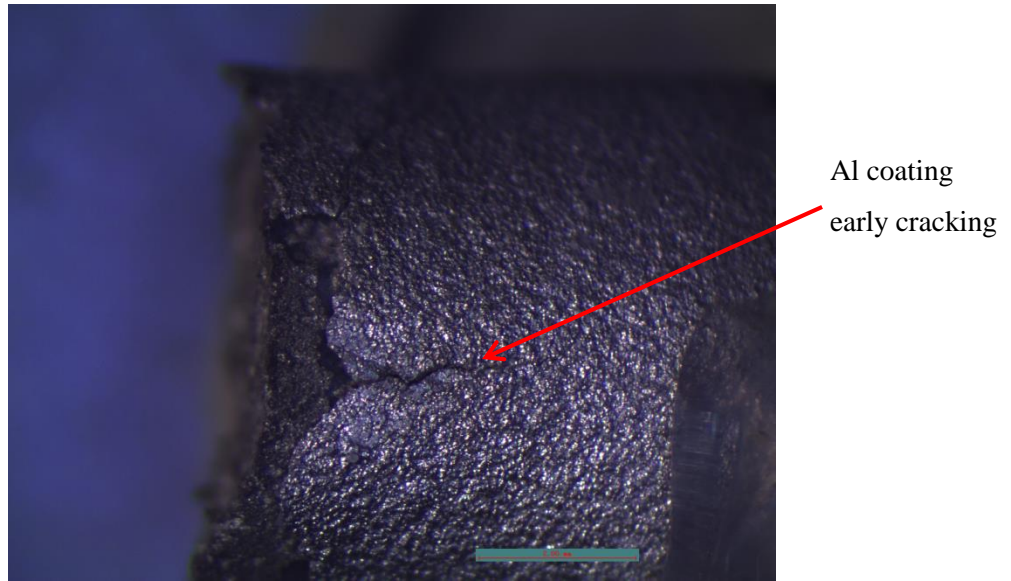


Figure 4.33: Cracking of Al cold spray coating on the surface at a stress of 60 MPa

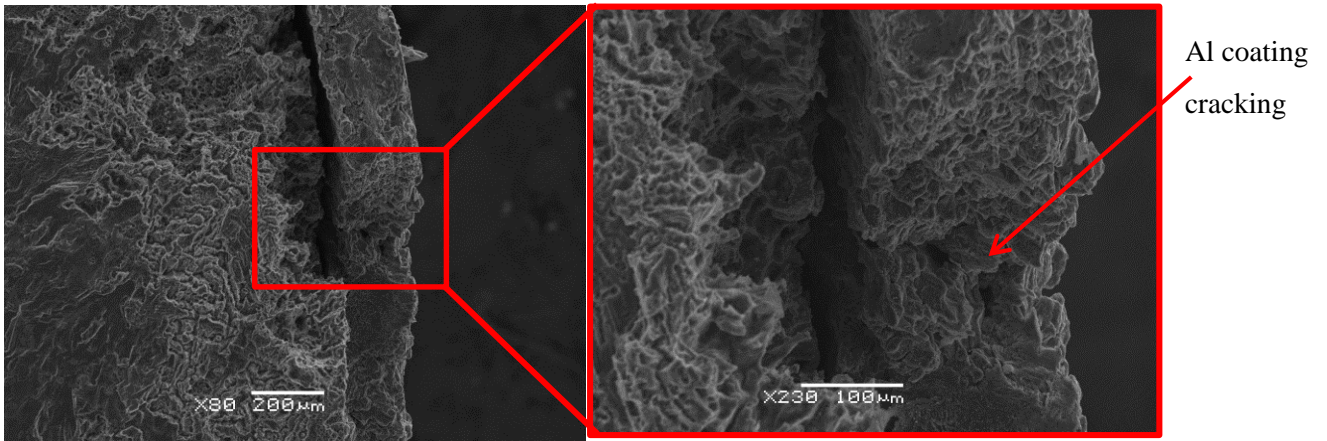


Figure 4.34: Cracking of Al cold spray coating at a stress of 80 MPa in the corrosion fatigue test

Table 4.7 compares the fatigue life of coated and uncoated specimens under equal stress and provides the percentage of fatigue life deterioration after applying Al cold spray coating. The table shows that the fatigue life at the same stress level for all tested specimens deteriorated after cold spray coating with a maximum percentage of 87.6% at 80 MPa stress.

Table 4.7: Percentage decrease in the corrosion fatigue life after cold spray

Stress level (MPa)	Fatigue life for uncoated specimens	Fatigue life for coated specimens	Fatigue life change (%)
120	83,479	10,319	87.6
90	97,505	69,847	28.4
80	494,127	87,516	82.3
60	1,844,358	801,348	56.6
40	13,408,273	3,659,473	72.7

4.3.1 Fracture Surface

Figure 4.35 shows the ideal fracture surfaces of round specimens under different types of loading [40]. The light areas represent the crack growth regions and the dashed areas represent final fracture regions. In the present study, the loading was rotating bending under low nominal stress and while the fracture surfaces of all of the failed specimens from the corrosion fatigue testing were examined, only select ones are reported as shown in Figure 4.36-Figure 4.39.

Plane Bending, Reversed Bending, and Rotational Bending Fatigue Failures

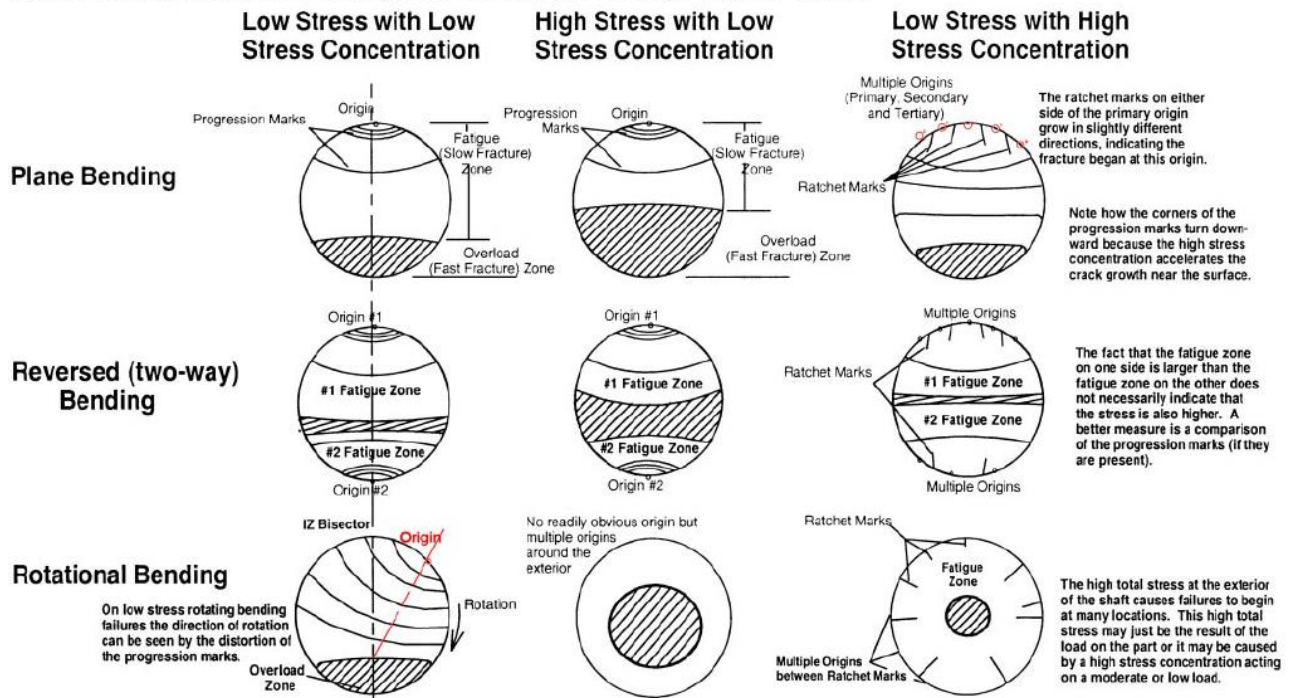
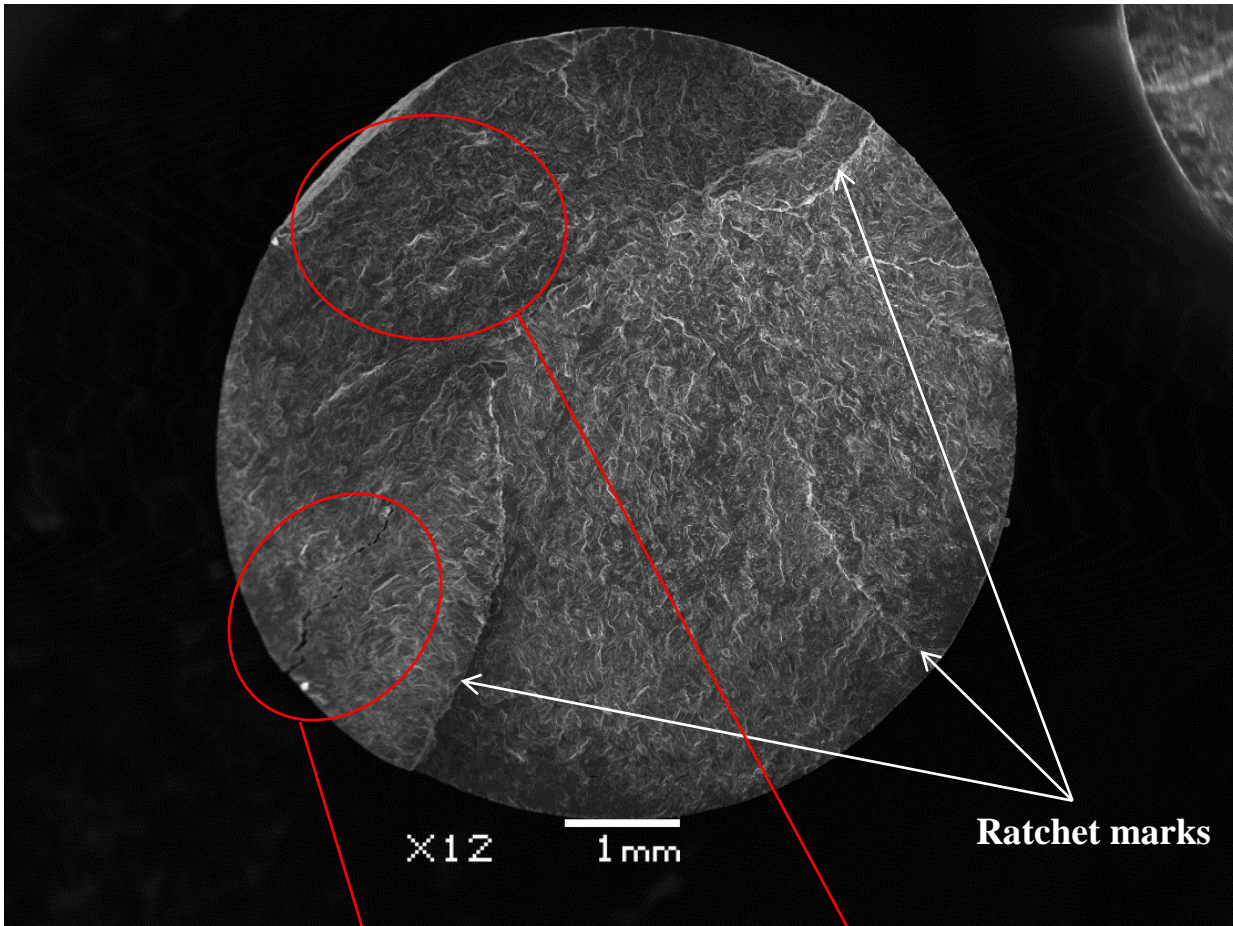
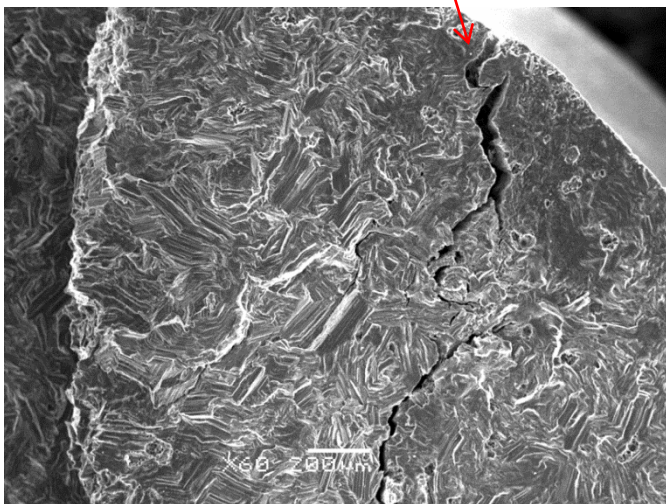


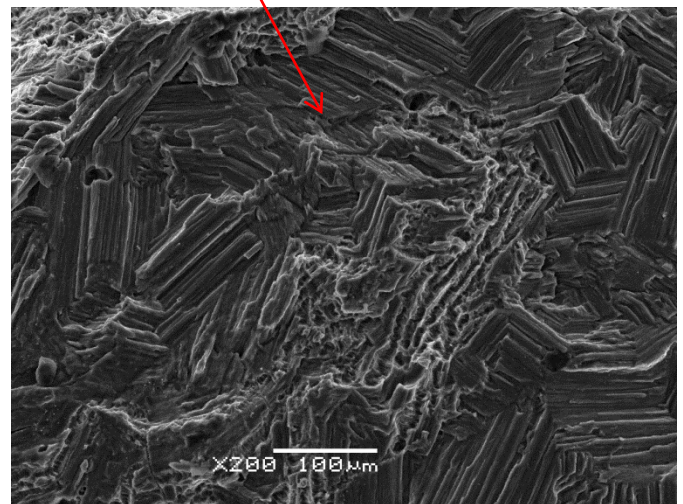
Figure 4.35: Fracture surfaces of round specimens under different types of loading [40]



a



b



c

Figure 4.36: Fracture surfaces of bare sample at a stress of 74 MPa showing: (a) overall fracture surface, (b) initiation with crack, and (c) brittle final fracture

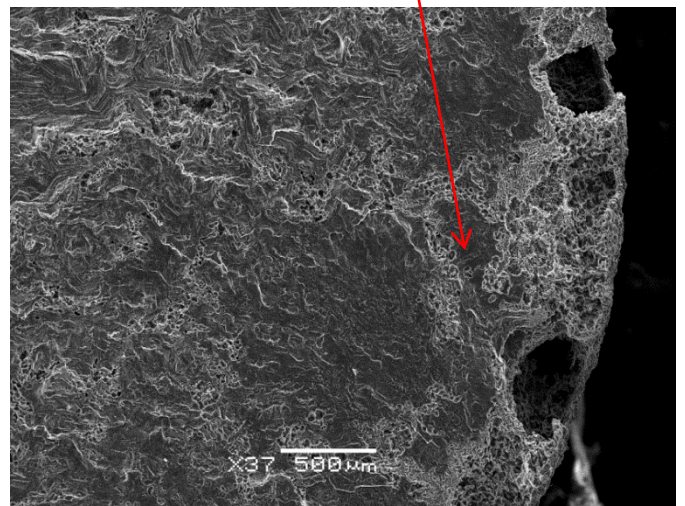
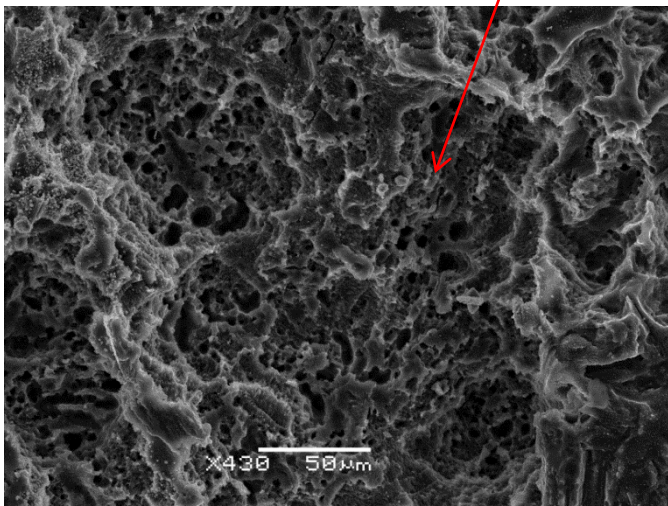
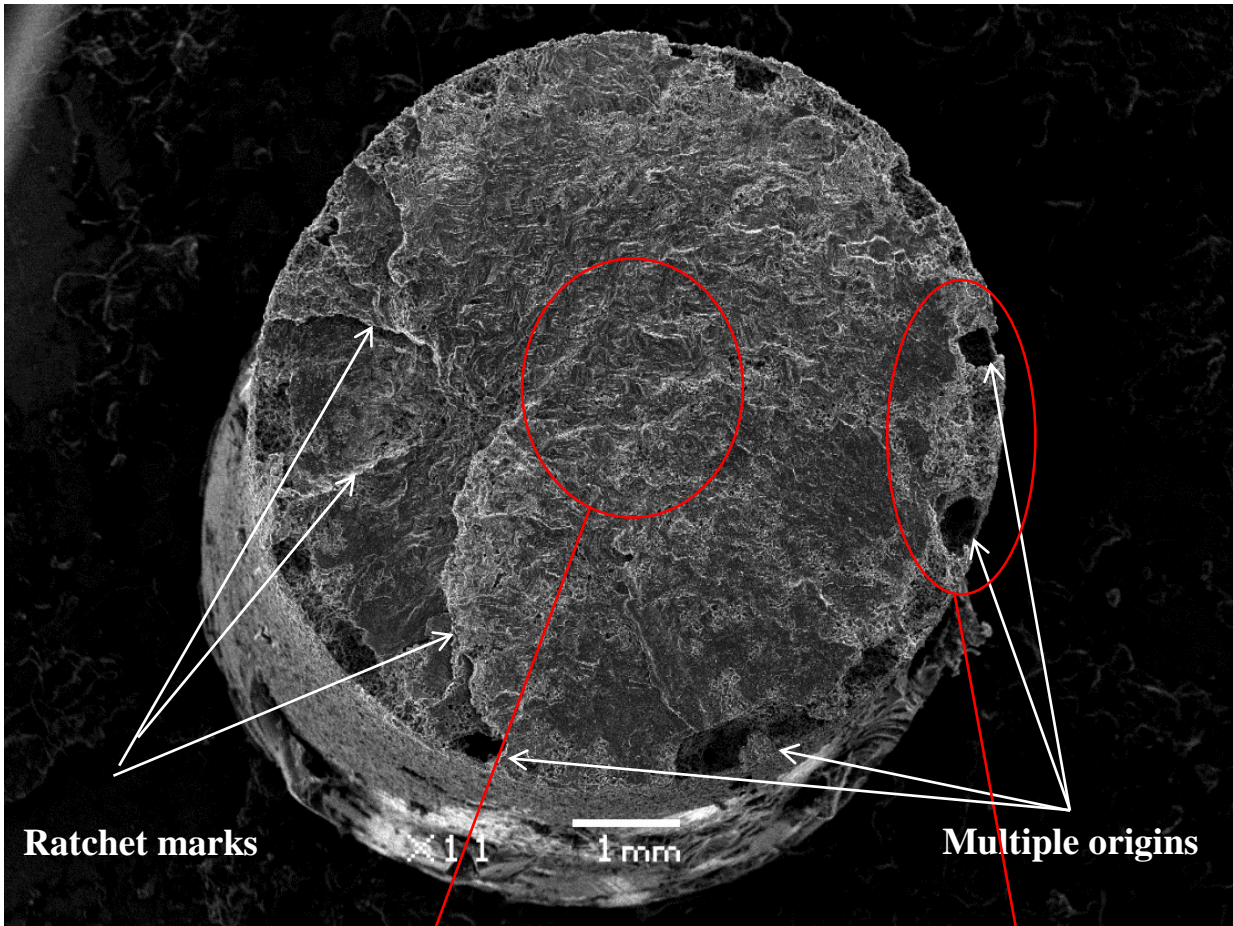
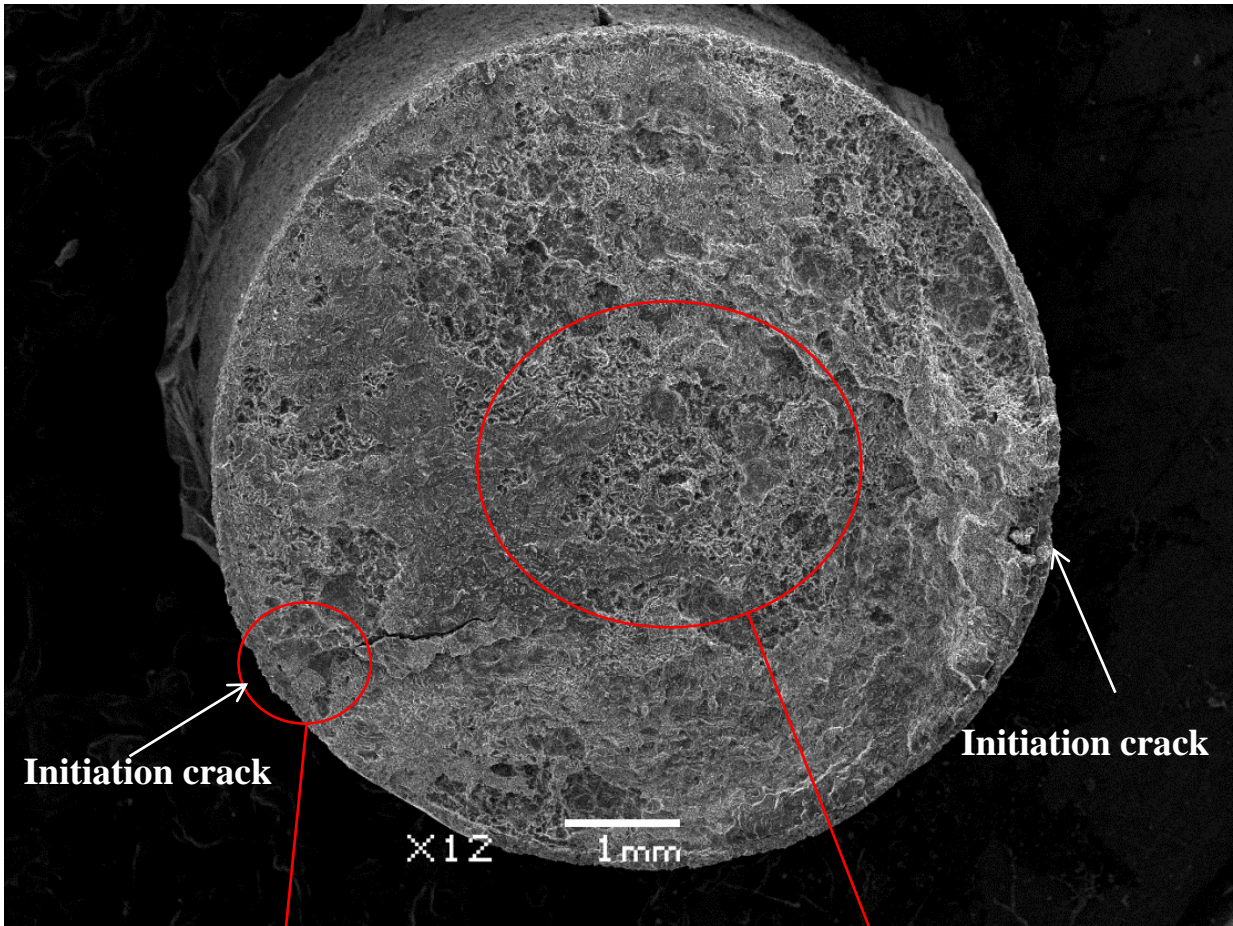
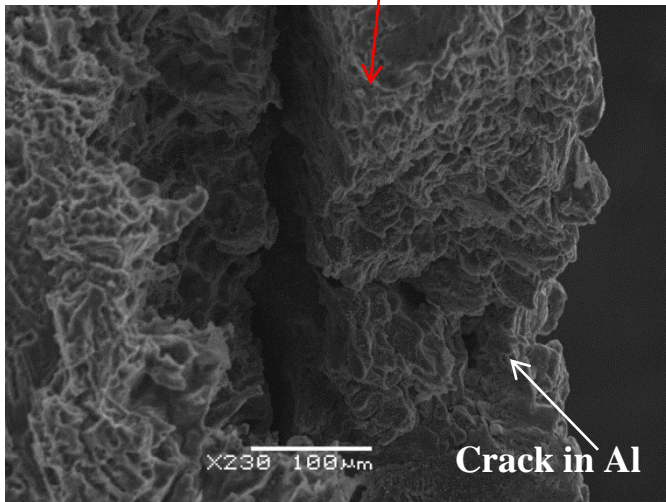


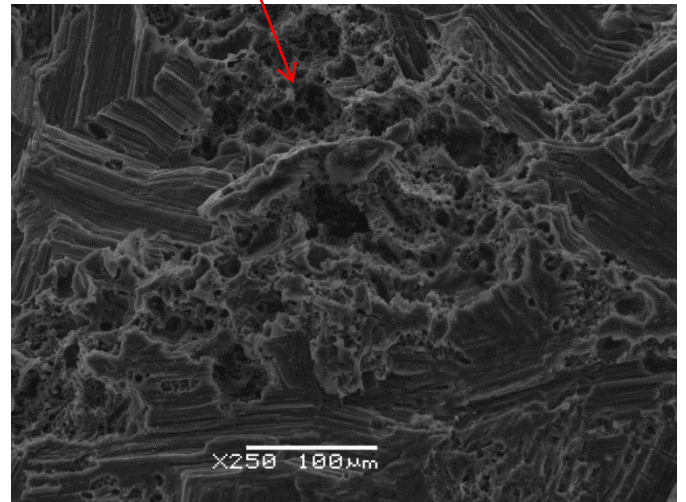
Figure 4.37: Fracture surfaces of bare sample at a stress of 40 MPa showing: (a) overall fracture surface, (b) mixed mode final fracture, and (c) initiation areas



a

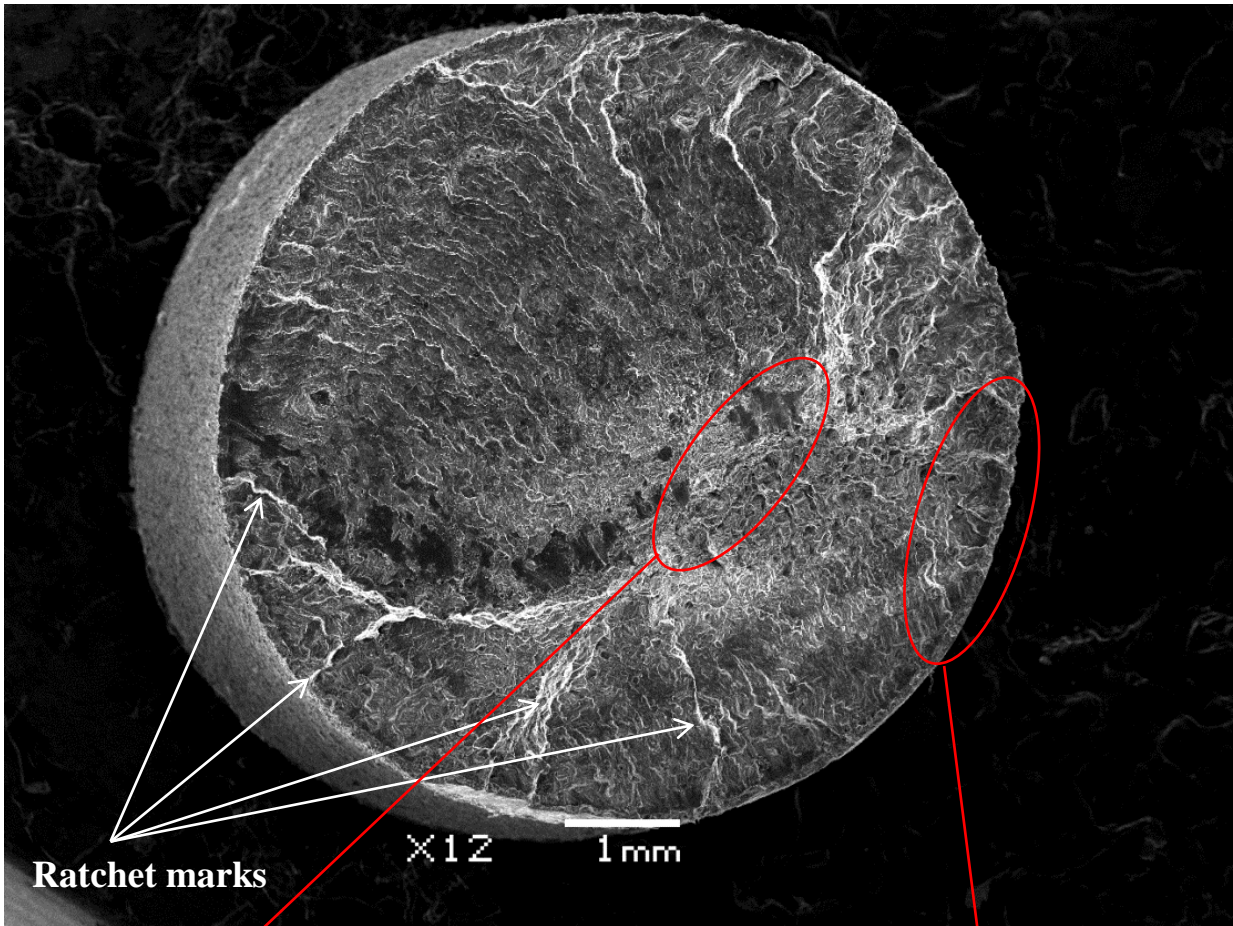


b

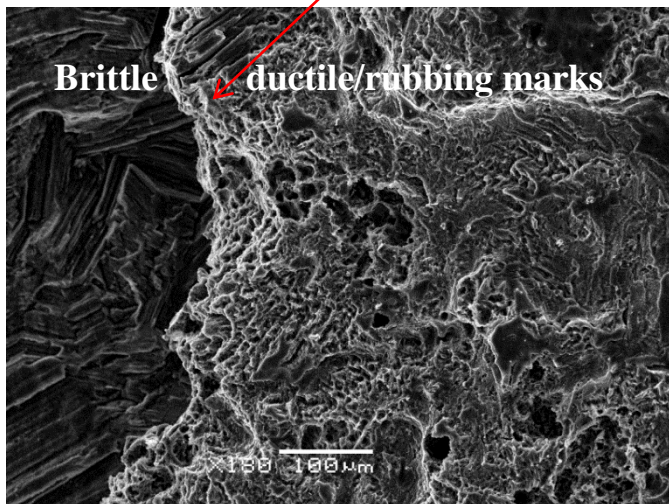


c

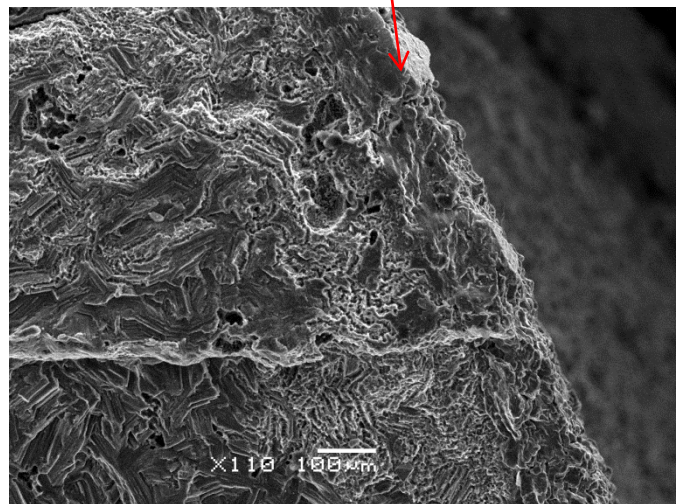
Figure 4.38: Fracture surfaces of a coated sample after the corrosion fatigue test at a stress of 80 MPa showing: (a) overall fracture surface, (b) initiation with coating crack, and (c) mixed mode final fracture



a



b



c

Figure 4.39: Fracture surfaces of a coated sample at a stress of 50 MPa showing: (a) overall fracture surface, (b) brittle final fracture, and (c) initiation area

- Figure 4.36 presents the fracture surfaces of bare failed specimen at a stress of 74 MPa. The ratchet marks revealed at the fracture surface indicate that the failure was initiated from multiple origins since ratchet mark separate two fracture origins from each other. No crack progression marks such as beach marks or striations were revealed. The crack growth region is the bright region at the bottom of the fracture surface and the final fracture took place in the dark smooth region at the top portion of the fracture surface. The final fracture is characterized by brittle features and this was likely attributed to the diffusion of hydrogen resulted from the corrosion reactions explained earlier to the Mg substrate. This phenomenon is known as hydrogen embrittlement [24].
- Figure 4.37 presents the fracture surfaces of bare failed specimen at a stress of 40 MPa. Multiple origins around the edges were clearly shown with the presence of ratchet marks that support the multiple crack origins. The crack growth seems to have occurred from the edges toward the middle, where a mixed mode final fracture took place.
- Figure 4.38 shows the fracture surfaces of a coated failed specimen at a stress of 50 MPa. Multiple origins were clearly shown with the presence of ratchet marks. Two cracks at the edges were identified as two fracture origins. These cracks initiated at the Al coating due to cyclic load and led to a penetration of the salt solution toward AZ31B substrate. The penetrated solution will cause stagnancy at the interface between Mg substrate and Al coating and this will cause a localized corrosion at the Mg substrate. A crack on Mg substrate will initiate then from that area until the final fracture of the specimen. The final fracture in this case seems to occur at the middle of the surface where a mixed mode failure appeared after cleavages and dimple features appeared.
- Figure 4.39 shows the fracture surfaces of a coated failed specimen at a stress of 80 MPa. Ratchet marks were present that indicate a multiple origins failure. The crack growth region is the rough area between the ratchet marks, and the final fracture is the smooth brittle area at the top/left portion of the surface. Figure 4:35b shows the line separating the crack growth region (right), where some ductility and rubbing marks due to cyclic load are revealed, from the final fracture (left) where a smooth brittle surface is clearly displayed. The appearances of the cleavages also support the possibility of occurrence the hydrogen embrittlement phenomena here.

Chapter 5

Conclusion and Recommendations for Future Work

5.1 Conclusion

Based on the experimental observations from the performed corrosion and corrosion fatigue tests, the following conclusions can be drawn:

- The 5% NaCl continuous fog environment had a significant impact on the bare Mg alloy AZ31B, resulting in a great amount of material loss.
- The observed corrosion mechanisms for the bare AZ31B are general and pitting corrosion.
- The presence of the chloride ions in the tested environment accelerates the corrosion rate, by weakening the Mg(OH)₂ film/preventing it from the reforming and contributing in pitting growth.
- Low volume fractions of secondary phases were identified as Mg-Al-Mn and Al-Mn compounds. The β-phase, Mg₁₇Al₁₂ was not recognized.
- Secondary phases and grains boundary act as galvanic cathodes to the α-Mg matrix and increased the corrosion rate. This fact explains the general and pitting corrosion morphology of the tested bare AZ31B coupons.
- The cold sprayed Al powder coating (SST-A05011 with a purity of >99.93%) deposited on AZ31B alloy, provided a considerable amount of protection from the corrosion attack as compared to the bare Mg AZ31B.
- No corrosion pits were noticed on the surface of Al coated specimens and the corrosion attack took place only from the edges that were not cold spray coated.
- The corrosion testing results showed that under 5% NaCl continuous fog environment, the Al cold spray coating was able to provide enough corrosion protection of the Mg alloy, if the coating integrity is not damaged.
- Exposure to a corrosive environment (3.5 % NaCl), significantly decreased the fatigue life of both the extruded AZ31B bare and coated samples as compared to their performance in air.
- The fatigue life of AZ31B in air was influenced by the surface residual stress of the tested samples, in which the fatigue life increased due to the compressive residual stress induced by the cold spraying process due to peening effect.

- The fatigue life of the cold sprayed specimens in a 3.5% NaCl environment was considerably inferior to that of the bare specimens, with a maximum deterioration of 82.3% at 80 MPa stress. This was attributed to the fact that the pure Al powder has much lower ultimate tensile strength than Mg alloy AZ31B which will lead to an earlier crack on the Al coating surface during the fatigue cycles, from which the electrolyte will penetrate to the Mg substrate and cause a localized corrosion and failure.
- Fracture surfaces of bare AZ31B failed specimen revealed the some ratchet marks which gives an indication of a multiple origins failure. Brittle final fractures were also revealed which are attributed to the diffusion of hydrogen resulted from the corrosion reactions of Mg substrate with a phenomenon that known as hydrogen embrittlement.
- Fracture surfaces of Al cold spray coated failed specimens revealed also the presence of ratchet marks and cleavages at final fracture as evidence of occurrence of hydrogen embrittlement. The detected crack in the Al coating lead to a penetration of the electrolyte toward AZ31B substrate and causing a localized corrosion and failure.

5.2 Recommendations for Future Work

As a continuation of this work, the following future research directions are recommended:

- Given that the ability now exists for Al cold spray coating to be carried out at the University of Waterloo, it is recommended that future coupons or specimens be fully deposited with Al powder – particularly including edges or thin areas – and corrosion tests be conducted to investigate how that impacts the corrosion results for coated specimens.
- The fatigue life of the AZ31B alloy in this work was poorer for samples coated with cold sprayed pure Al powders. It has been reported that the cold spraying of Al alloys results in a better fatigue life versus samples sprayed with pure Al [97]. Therefore, it is recommended that samples of AZ31B be cold sprayed with Al alloy powders having UTSs comparable to AZ31B (e.g., commercially available AA6064 or AA7075 powders), and then their corrosion and corrosion fatigue behavior investigated.
- Consideration of anodizing the samples before coating may lead into creation of a protective layer between Al powder and Mg substrate that breaks the circuit between the two in case of possibility of localized galvanic corrosion

Appendix A

Coated Coupons' Surface Roughness Measurements

Coupon 1, cycle 4 before testing

ISO 25178			
Height Parameters			
Sq	150	µm	Root mean square height
Ssk	-0.174		Skewness
Sku	2.96		Kurtosis
Sp	399	µm	Maximum peak height
Sv	475	µm	Maximum pit height
Sz	873	µm	Maximum height
Sa	116	µm	Arithmetic mean height

After testing

ISO 25178			
Height Parameters			
Sq	215	µm	Root mean square height
Ssk	0.953		Skewness
Sku	4.68		Kurtosis
Sp	851	µm	Maximum peak height
Sv	596	µm	Maximum pit height
Sz	1448	µm	Maximum height
Sa	152	µm	Arithmetic mean height

Coupon 2, cycle 8 before testing

ISO 25178			
Height Parameters			
Sq	183	µm	Root mean square height
Ssk	0.621		Skewness
Sku	4.2		Kurtosis
Sp	732	µm	Maximum peak height
Sv	502	µm	Maximum pit height
Sz	1234	µm	Maximum height
Sa	133	µm	Arithmetic mean height

After testing

ISO 25178			
Height Parameters			
Sq	288	µm	Root mean square height
Ssk	1.01		Skewness
Sku	2.86		Kurtosis
Sp	850	µm	Maximum peak height
Sv	395	µm	Maximum pit height
Sz	1245	µm	Maximum height
Sa	238	µm	Arithmetic mean height

Coupon 3, cycle 11 before testing

ISO 25178			
Height Parameters			
Sq	146	µm	Root mean square height
Ssk	0.0338		Skewness
Sku	2.62		Kurtosis
Sp	371	µm	Maximum peak height
Sv	391	µm	Maximum pit height
Sz	761	µm	Maximum height
Sa	117	µm	Arithmetic mean height

After testing

ISO 25178			
Height Parameters			
Sq	259	µm	Root mean square height
Ssk	0.965		Skewness
Sku	2.93		Kurtosis
Sp	759	µm	Maximum peak height
Sv	431	µm	Maximum pit height
Sz	1190	µm	Maximum height
Sa	212	µm	Arithmetic mean height

Coupon 4, cycle 14 before testing

ISO 25178			
Height Parameters			
Sq	165	µm	Root mean square height
Ssk	1.03		Skewness
Sku	3.17		Kurtosis
Sp	514	µm	Maximum peak height
Sv	172	µm	Maximum pit height
Sz	686	µm	Maximum height
Sa	137	µm	Arithmetic mean height

After testing

ISO 25178			
Height Parameters			
Sq	300	µm	Root mean square height
Ssk	0.986		Skewness
Sku	2.74		Kurtosis
Sp	871	µm	Maximum peak height
Sv	434	µm	Maximum pit height
Sz	1305	µm	Maximum height
Sa	250	µm	Arithmetic mean height

Coupon 5, cycle 17 before testing

ISO 25178			
Height Parameters			
Sq	133	µm	Root mean square height
Ssk	1.39		Skewness
Sku	3.98		Kurtosis
Sp	414	µm	Maximum peak height
Sv	132	µm	Maximum pit height
Sz	546	µm	Maximum height
Sa	104	µm	Arithmetic mean height

After testing

ISO 25178			
Height Parameters			
Sq	221	µm	Root mean square height
Ssk	-4.21		Skewness
Sku	42		Kurtosis
Sp	370	µm	Maximum peak height
Sv	2269	µm	Maximum pit height
Sz	2639	µm	Maximum height
Sa	155	µm	Arithmetic mean height

Coupon 6, cycle 20 before testing

ISO 25178			
Height Parameters			
Sq	187	µm	Root mean square height
Ssk	-0.425		Skewness
Sku	1.89		Kurtosis
Sp	359	µm	Maximum peak height
Sv	420	µm	Maximum pit height
Sz	780	µm	Maximum height
Sa	162	µm	Arithmetic mean height

After testing

ISO 25178			
Height Parameters			
Sq	250	µm	Root mean square height
Ssk	0.847		Skewness
Sku	3.02		Kurtosis
Sp	803	µm	Maximum peak height
Sv	460	µm	Maximum pit height
Sz	1263	µm	Maximum height
Sa	201	µm	Arithmetic mean height

Coupon 7, cycle 23 before testing

ISO 25178			
Height Parameters			
Sq	176	µm	Root mean square height
Ssk	0.462		Skewness
Sku	2.5		Kurtosis
Sp	723	µm	Maximum peak height
Sv	372	µm	Maximum pit height
Sz	1095	µm	Maximum height
Sa	151	µm	Arithmetic mean height

After testing

ISO 25178			
Height Parameters			
Sq	269	µm	Root mean square height
Ssk	0.524		Skewness
Sku	2.18		Kurtosis
Sp	729	µm	Maximum peak height
Sv	440	µm	Maximum pit height
Sz	1169	µm	Maximum height
Sa	232	µm	Arithmetic mean height

Coupon 8, cycle 26 before testing

ISO 25178			
Height Parameters			
Sq	144	µm	Root mean square height
Ssk	0.335		Skewness
Sku	3.42		Kurtosis
Sp	548	µm	Maximum peak height
Sv	415	µm	Maximum pit height
Sz	963	µm	Maximum height
Sa	111	µm	Arithmetic mean height

After testing

ISO 25178			
Height Parameters			
Sq	204	µm	Root mean square height
Ssk	0.0836		Skewness
Sku	3.1		Kurtosis
Sp	678	µm	Maximum peak height
Sv	577	µm	Maximum pit height
Sz	1255	µm	Maximum height
Sa	161	µm	Arithmetic mean height

Coupon 9, cycle 33 before testing

ISO 25178			
Height Parameters			
Sq	176	µm	Root mean square height
Ssk	0.462		Skewness
Sku	2.5		Kurtosis
Sp	723	µm	Maximum peak height
Sv	372	µm	Maximum pit height
Sz	1095	µm	Maximum height
Sa	151	µm	Arithmetic mean height

After testing

ISO 25178			
Height Parameters			
Sq	337	µm	Root mean square height
Ssk	0.88		Skewness
Sku	4.94		Kurtosis
Sp	1313	µm	Maximum peak height
Sv	1736	µm	Maximum pit height
Sz	3049	µm	Maximum height
Sa	264	µm	Arithmetic mean height

Coupon 10, cycle 33 after testing

ISO 25178			
Height Parameters			
Sq	356	µm	Root mean square height
Ssk	-0.791		Skewness
Sku	2.57		Kurtosis
Sp	510	µm	Maximum peak height
Sv	1099	µm	Maximum pit height
Sz	1610	µm	Maximum height
Sa	300	µm	Arithmetic mean height

Coupon 11, cycle 33 after testing

ISO 25178			
Height Parameters			
Sq	360	µm	Root mean square height
Ssk	0.502		Skewness
Sku	2.2		Kurtosis
Sp	1116	µm	Maximum peak height
Sv	576	µm	Maximum pit height
Sz	1692	µm	Maximum height
Sa	307	µm	Arithmetic mean height

Coupon 12, cycle 40 before testing

ISO 25178			
Height Parameters			
Sq	153	µm	Root mean square height
Ssk	1.82		Skewness
Sku	7.34		Kurtosis
Sp	829	µm	Maximum peak height
Sv	296	µm	Maximum pit height
Sz	1125	µm	Maximum height
Sa	108	µm	Arithmetic mean height

After testing

ISO 25178			
Height Parameters			
Sq	384	µm	Root mean square height
Ssk	-0.661		Skewness
Sku	2.26		Kurtosis
Sp	452	µm	Maximum peak height
Sv	878	µm	Maximum pit height
Sz	1330	µm	Maximum height
Sa	331	µm	Arithmetic mean height

Coupon 13, cycle 40 after testing

ISO 25178			
Height Parameters			
Sq	398	µm	Root mean square height
Ssk	-0.395		Skewness
Sku	2.09		Kurtosis
Sp	706	µm	Maximum peak height
Sv	1025	µm	Maximum pit height
Sz	1731	µm	Maximum height
Sa	340	µm	Arithmetic mean height

Coupon 14, cycle 40 after testing

ISO 25178			
Height Parameters			
Sq	413	µm	Root mean square height
Ssk	-0.311		Skewness
Sku	1.87		Kurtosis
Sp	772	µm	Maximum peak height
Sv	935	µm	Maximum pit height
Sz	1707	µm	Maximum height
Sa	359	µm	Arithmetic mean height

Coupon 15, cycle 60 before testing

ISO 25178			
Height Parameters			
Sq	145	µm	Root mean square height
Ssk	1.15		Skewness
Sku	4.82		Kurtosis
Sp	634	µm	Maximum peak height
Sv	425	µm	Maximum pit height
Sz	1059	µm	Maximum height
Sa	107	µm	Arithmetic mean height

After testing

ISO 25178			
Height Parameters			
Sq	416	µm	Root mean square height
Ssk	-0.334		Skewness
Sku	1.88		Kurtosis
Sp	739	µm	Maximum peak height
Sv	889	µm	Maximum pit height
Sz	1628	µm	Maximum height
Sa	363	µm	Arithmetic mean height

Coupon 16, cycle 60 after testing

ISO 25178			
Height Parameters			
Sq	431	µm	Root mean square height
Ssk	0.191		Skewness
Sku	8.6		Kurtosis
Sp	1953	µm	Maximum peak height
Sv	2305	µm	Maximum pit height
Sz	4257	µm	Maximum height
Sa	296	µm	Arithmetic mean height

Coupon 17, cycle 60 after testing

ISO 25178			
Height Parameters			
Sq	540	µm	Root mean square height
Ssk	-0.873		Skewness
Sku	2.69		Kurtosis
Sp	966	µm	Maximum peak height
Sv	1561	µm	Maximum pit height
Sz	2527	µm	Maximum height
Sa	455	µm	Arithmetic mean height

Coupon 18, cycle 90 before testing

ISO 25178			
Height Parameters			
Sq	178	µm	Root mean square height
Ssk	0.337		Skewness
Sku	2.45		Kurtosis
Sp	602	µm	Maximum peak height
Sv	389	µm	Maximum pit height
Sz	991	µm	Maximum height
Sa	146	µm	Arithmetic mean height

After testing

ISO 25178			
Height Parameters			
Sq	562	µm	Root mean square height
Ssk	-1.35		Skewness
Sku	8.55		Kurtosis
Sp	1741	µm	Maximum peak height
Sv	2333	µm	Maximum pit height
Sz	4074	µm	Maximum height
Sa	329	µm	Arithmetic mean height

Coupon 19, cycle 90 after testing

ISO 25178			
Height Parameters			
Sq	772	µm	Root mean square height
Ssk	0.0688		Skewness
Sku	3.77		Kurtosis
Sp	2222	µm	Maximum peak height
Sv	3516	µm	Maximum pit height
Sz	5739	µm	Maximum height
Sa	601	µm	Arithmetic mean height

Coupon 20, cycle 90 after testing

ISO 25178			
Height Parameters			
Sq	822	µm	Root mean square height
Ssk	-2.4		Skewness
Sku	8.08		Kurtosis
Sp	932	µm	Maximum peak height
Sv	4437	µm	Maximum pit height
Sz	5369	µm	Maximum height
Sa	532	µm	Arithmetic mean height

Bibliography

- [1] J.E. Gray, B. Luan, "Protective coatings on magnesium and its alloys a critical review", *Journal of Alloys and Compounds*, Vol. 336, (2002), pp. 88–113.
- [2] Global and China Automotive Magnesium Alloy Industry Report 2012-2015, retrieved May (2013), <http://www.researchinchina.com/htmls/report/2013/6680.html>
- [3] Md. Shahnewaz Bhuiyan, Yoshiharu Mutoh, Tsutomu Murai, Shinpei Iwakami, "Corrosion fatigue behavior of extruded magnesium alloy AZ80-T5 in a 5% NaCl environment", *Engineering Fracture Mechanics*, Vol. 77, (2010), pp. 1567–1576.
- [4] CHENG Ying-liang, QIN Ting-wei, WANG Hui-min, ZHANG Zhao, "Comparison of corrosion behaviors of AZ31, AZ91, AM60 and ZK60 magnesium alloys", *Trans. Nonferrous Met. Soc. China* Vol. 19, (2009), pp. 517-524.
- [5] Qing Qu, Jie Ma, Lin Wang, Lei Li, Wei Bai, Zhongtao Ding, "Corrosion behaviour of AZ31B magnesium alloy in NaCl solutions saturated with CO₂", *Corrosion Science* Vol. 53, (2011), pp. 1186–1193.
- [6] Jinsun Liao, Makoto Hotta, Naotsugu Yamamoto, "Corrosion behavior of fine-grained AZ31B magnesium alloy", *Corrosion Science* Vol. 61, (2012), pp. 208–214.
- [7] B.-A. Behrens, I. Schmidt, "Improving the properties of forged magnesium parts by optimized process parameters", *Journal of Materials Processing Technology* Vol. 187–188, (2007), pp. 761–765.
- [8] X.B. Chen, N. Birbilis, and T.B. Abbott, "Review of Corrosion-Resistant Conversion Coatings for Magnesium and Its Alloys", *Corrosion Science Section, NACE International*, (2011).
- [9] Ping Zhu Liang You Wang Guang Ren Qian Tie Hua Cao Ming Zhou, "Copper coating electrodeposited directly onto AZ31 magnesium alloy", *Anti-Corrosion Methods and Materials*, Vol. 60, Iss 3, (2013), pp. 127 – 133.
- [10] Fei Chen, Hai Zhou, Bin Yao, Zhen Qin, Qingfeng Zhang, "Corrosion resistance property of the ceramic coating obtained through microarc oxidation on the AZ31 magnesium alloy surfaces", *Surface & Coatings Technology*, Vol. 201, (2007), pp. 4905–4908.
- [11] A. Eliezer, E.M. Gutman, E. Abramov, Ya. Unigoveski, "Corrosion fatigue of die-cast and extruded magnesium alloys", *Journal of light metals*, Vol. 1, (2001), pp. 169-186.
- [12] ASTM B117-09, Standard Practice for Operating Salt Spray (Fog) Apparatus, ASTM International, West Conshohocken, PA, (2009), <http://www.astm.org/>
- [13] Mark A. Shand, "The Chemistry and Technology of Magnesia", Wiley, (2006).

- [14] I. J. Polmear, "Overview Magnesium alloys and applications", Mater. Sci. Tech., Vol. 10, (1995), pp. 1-16.
- [15] D. Sameer Kumar, C. Tara Sasanka, K. Ravindra, K.N.S. Suman, "Magnesium and Its Alloys in Automotive Applications – A Review", Columbia International Publishing American Journal of Materials Science and Technology Vol. 4, Issue. 1, (2015), pp. 12-30.
- [16] Edward Ghali, Wolfgang Dietzel, and Karl-Ulrich Kainer, "General and Localized Corrosion of Magnesium Alloys: A Critical Review", ASM International, Journal of Materials Engineering and Performance Vol. 13, (2004), pp. 7-23.
- [17] D. Eliezer, E. Aghion, F.H. (SAM) Froes, "Magnesium Science, Technology and Applications", Advanced Performance Materials Vol. 5, (1998), pp. 201–212.
- [18] Mustafa Kemal Kulekci, "Magnesium and its alloys applications in automotive industry", Int J Adv Manuf Technol, Vol. 39, (2008), pp. 851–865.
- [19] B.L. Mordike, T. Ebert, "Magnesium Properties, applications, potential", Materials Science and Engineering, Vol. 302, (2001), pp. 37–45.
- [20] Mark Easton, Mark Gibson, Aiden Beer, Matthew Barnett, Chris Davies, Yvonne Durandet, Stuart Blacket, Xiaobo Chen, Nick Birbilis, and Trevor Abbott, "The Application of Magnesium Alloys to the Lightweighting of Automotive Structures", CAST Co-operative Research Centre, (2000).
- [21] Alan A. Luo, "Magnesium: Current and Potential Automotive Applications", JOM, (2002).
- [22] C. Blawert, N. Hort and K.U. Kainer, "Automotive Applications of Magnesium and its Alloys", Trans. Indian Inst. Met. Vol.57, No. 4, (2004), pp. 397-408.
- [23] Martyn Alderman, "Magnesium: The Lightest Structural Metal in Automotive, Proceedings of Global Automotive Lightweight Materials, Magnesium Elektron, <http://www.global-automotive-lightweight-materials.com/media/downloads/109-1620-martyn-alderman-magnesium-elektron.pdf>, retrieved Aug 4, (2014).
- [24] William D. Callister, Jr., "Materials Science and Engineering", John Wiley & Sons, Inc., (2007).
- [25] W.A. Ferrando, "Review of Corrosion and Corrosion Control of Magnesium Alloys and Composites", Journal of Materials Engineering, Vol. 11, Issue 4, (1989), pp 299-313.
- [26] G. L. Makar and J. Kruger, "Corrosion of magnesium and its alloys, International Materials Reviews", Vol. 38, Issue 3, (1993), pp. 138-153.

- [27] Guang Ling Song and Andrej Atrens, "Corrosion Mechanisms of Magnesium Alloys", *Advanced Engineering Materials*, Vol. 1, Issue 1, (1999), pp. 11-33.
- [28] Guang Ling Song and Andrej Atrens, "Understanding Magnesium Corrosion", *Advanced Engineering Materials*, Vol. 5, Issue 12, (2003), pp. 837-858.
- [29] Barbara A. Shaw, "Corrosion Resistance of Magnesium Alloys", *ASM Handbook, Volume 13A Corrosion: Fundamentals, Testing, and Protection*, (2003), pp. 692-696.
- [30] Guang Ling Song and Andrej Atrens, "Recent Progress in Corrosion of Magnesium Alloys", *Advanced Engineering Materials*, Vol. 7, Issue 7, (2005), pp. 563-586.
- [31] Zeng Rong-chang, H ANG Jin, Huang Wei-jiu, W. Dietzel, K. U. Kainer, C. Blawert, KE Wei, "Review of studies on corrosion of magnesium alloys", *Transactions of Nonferrous Metals Society of China*, Vol. 16, (2006), pp.763-771.
- [32] Guang Song, "Corrosion of magnesium alloys", Woodhead Publishing, (2011).
- [33] Kelvii Wei Guo, "A Review of Magnesium/Magnesium Alloys Corrosion and its Protection", *Recent Patents on Corrosion Science*, Vol. 2, (2010), pp. 13-21.
- [34] S. Mathieu, C. Rapin, J. Hazan, P. Steinmetz, "Corrosion behaviour of high pressure die-cast and semi-solid cast AZ91D alloys", *Corrosion Science*, Vol. 44, (2002), pp. 2737–2756.
- [35] Ming-Chun Zhao, Ming Liu, Guangling Song, Andrej Atrens, "Influence of the b-phase morphology on the corrosion of the Mg alloy AZ91", *Corrosion Science*, Vol. 50, (2008), pp. 1939–1953.
- [36] Naing Naing Aung, Wei Zhou, "Effect of grain size and twins on corrosion behaviour of AZ31B magnesium alloy", *Corrosion Science*, Vol. 52, (2010), pp. 589–594.
- [37] Nicholas Winzer, Andrej Atrens, Guangling Song, "A Critical Review of the Stress Corrosion Cracking of Magnesium Alloys", *Advanced Engineering Materials*, Vol. 7, Issue, 8, (2005), pp. 659-693.
- [38] ASTM G46 – 94 Standard Guide for Examination and Evaluation of Pitting Corrosion¹, ASTM International, West Conshohocken, PA, (2013), <http://www.astm.org/>
- [39] Robert T. Ruggeri and Theodore R. Brck, "An Analysis of Mass Transfer in Filiform Corrosion", *NACE*, 1983. Vol. 39, Issue, 11, (1983), pp. 452-465.
- [40] *ASM International Handbook, "Fatigue and Fracture"*, United State of America, ASM International, Vol. 19, (1986).
- [41] Claude Bathias, André Pineau, "Fatigue of Materials and Structures", John Wiley, (2011).

- [42] William T. Becker, "Principles of Failure Analysis "Fatigue Failure" ", United State of America, ASM International, (2002).
- [43] N.W. Sachs, P.E, "Understanding the Surface Features of Fatigue Fractures: How They Describe the Failure Cause and the Failure History", Journal of Failure Analysis and Prevention, Vol. 5(2), (2005), pp. 11-15.
- [44] Cynthia L. Meade, "Accelerated Corrosion Testing, National Exposure Testing", Sylvania, Ohio, pp.540-545.
- [45] Q-Panel Lab, "Introduction to Cyclic Corrosion Testing, Technical Bulletin LF-8144, (1994).
- [46] Ford Corporate Engineering Test Procedure, Global Laboratory Accelerated Cyclic Corrosion Test, Engineering Standards & Systems Engineering (ESSE), pp. 1-14, (2013).
- [47] General Motors Engineering Standards, GM 9540P Cyclic Corrosion Laboratory Test, (2010).
- [48] SAE International, the Engineering Society for Advancing Mobility Land Sea Air and Space, SAE J2334 cosmetic corrosion lab test, (1998).
- [49] Quantifying Paint System Performance, Article From: Products Finishing, George Shaw, Materials Engineering Team (AMSTA-TR-E/MEPS) from U.S. Army-Tank Automotive and Armaments Command, (2001).
- [50] Yuan-Yuan Yue, Zhong-Xia Liua, Ting-Ting Wan, Pei-Chung Wang, "Effect of phosphate-silane pretreatment on the corrosion resistance and adhesive-bonded performance of the AZ31 magnesium alloys", Progress in Organic Coatings, Vol. 76, (2013), pp. 835- 843.
- [51] Nguyen Van Phuong, Kyuhwan Lee, Doyon Chang, Man Kim, Sangyeoul Lee, and Sungmo Moon, "Zinc Phosphate Conversion Coatings on Magnesium Alloys: A Review", Met. Mater. Int., Vol. 19, No. 2 (2013), pp. 273-281.
- [52] X.B. Chen, H.Y. Yang, T.B. Abbott, M.A. Easton and N. Birbilis, "Corrosion-Resistant Electrochemical Platings on Magnesium Alloys: A State-of-the-Art Review", NACE International, Corrosion, Vol. 68, No. 6, (2012), pp. 518-535.
- [53] H. M. Wang, Z. H. Chen and L. L. Li, "Corrosion resistance and microstructure characteristics of plasma electrolytic oxidation coatings formed on AZ31 magnesium alloy", Maney, Vol. 26, No. 5, (2010), pp. 385-391.
- [54] Salih Durdu, Selin Bayramoglu, Aysun Demirtas, Metin Usta, A. Hikmet Üçisk, "Characterization of AZ31 Mg Alloy coated by plasma electrolytic oxidation", Elsevier, Vacuum 88, (2013), pp. 130-133.

- [55] Huan Chen, GuoHua Lv, GuLing Zhang, Hua Pang, XingQuan Wang, HeonJu Lee, SiZe Yang, (2005), "Corrosion performance of plasma electrolytic oxidized AZ31 magnesium alloy in silicate solutions with different additives", Elsevier, Surface & Coatings Technology Vol. 205, (2010), pp. 32–35.
- [56] Hyun Sam Ryu, Dong-Soo Park, Seong-Hyeon Hong, "Improved corrosion protection of AZ31 magnesium alloy through plasma electrolytic oxidation and aerosol deposition duplex treatment", Elsevier, Surface & Coatings Technology, Vol. 219, (2013), pp. 82–87.
- [57] Tae Seop Lim, Hyun Sam Ryu, and Seong-Hyeon Hong, "Plasma Electrolytic Oxidation/Cerium Conversion Composite Coatings for the Improved Corrosion Protection of AZ31 Mg Alloys", The Electrochemical Society, Journal of The Electrochemical Society, Vol. 160 (2), (2013), pp. 77-82.
- [58] Harminder Singh, T.S. Sidhu and S.B.S., "Cold spray technology: future of coating deposition processes", H. Singh et alii, Frattura ed Integrità Strutturale, Vol. 22, (2012), pp. 69-84.
- [59] Frank Gärtner, Thorsten Stoltenhoff, Tobias Schmidt, and Heinrich Kreye, "The Cold Spray Process and Its Potential for Industrial Applications", ASM International, Journal of Thermal Spray Technology, Vol. 15(2), (2006), pp. 223-232.
- [60] Brian S. DeForce, Timothy J. Eden, and John K. Potter, "Cold Spray Al-5% Mg Coatings for the Corrosion Protection of Magnesium Alloys", ASM International, Journal of Thermal Spray Technology, Vol. 20(6), (2011), pp. 1352-1358.
- [61] Hamid Assadi, Frank Gärtner, Thorsten Stoltenhoff, Heinrich Kreye, "Bonding mechanism in cold gas spraying", Acta Materialia, Vol. 51, (2003), pp. 4379–4394.
- [62] O. Lunder, T. KR. Aune, and K. Nisancioglu, "Effect of Mn Additions on the Corrosion Behavior of Mould-Cast Magnesium ASTM AZ91", NACE, Vol. 43, No. 5. (1987), pp. 291-295.
- [63] O. Lunder, J. E. Lein, T. KR. Aune, and K. Nisancioglu, "The Role of Mg 17Al 12 Phase in the Corrosion of Mg Alloy AZ91", NACE, Vol. 45, No. 9, (1989), pp. 741-748.
- [64] T. Beldjoudi, C. Fiaud, and L. Robbiola, (2005), "Influence of Homogenization and Artificial Aging Heat Treatments on Corrosion Behavior of Mg-Al Alloys", NACE, Corrosion, Vol. 49, No. 9, (1993), pp. 738-745.
- [65] Guangling Song, Andrej Atrens, Xianliang WU and BO Zhang, "Corrosion Behaviour of AZ21, AZ501 and AZ91 in Sodium Chloride", Corrosion Science, Vol. 40, No. 10, (1998), pp. 1769-1791.

- [66] Ming-Chun Zhao, Patrik Schmutz, "An exploratory study of the corrosion of Mg alloys during interrupted salt spray testing", *Corrosion Science*, Vol. 51, (2009), pp. 1277–1292.
- [67] Cheng Ying-liang, Qin Ting-wei, "Comparison of corrosion behaviors of AZ31, AZ91, AM60 and ZK60 magnesium alloys", *Trans. Nonferrous Met. Soc. China*, Vol. 19, (2009), pp. 517-524.
- [68] Wenjuan Liu, Fahe Cao, Linrong Chang, Zhao Zhang, Jianqing Zhang, "Effect of rare earth element Ce and La on corrosion behavior of AM60 magnesium alloy", *Corrosion Science*, Vol. 51, (2009), pp. 1334–1343.
- [69] Wenjuan Liu, Fahe Cao, Linrong Chang, Zhao Zhang, Jianqing Zhang, "Effect of rare earth element Ce and La on corrosion behavior of AM60 magnesium alloy Part 2", *Corrosion Science*, Vol. 52, (2010), pp. 639–650.
- [70] Tao Zhang, Yawei Shao, Guozhe Meng, Zhongyu Cui, Fuhui Wang, "Corrosion of hot extrusion AZ91 magnesium alloy: I-relation between the microstructure and corrosion behavior", *Corrosion Science*, Vol. 53, (2011), pp. 1960–1968.
- [71] R. Arrabal, A. Pardo, M.C. Merino, M. Mohedano, P. Casajus, K. Paucar, G. Garces, "Effect of Nd on the corrosion behaviour of AM50 and AZ91D magnesium alloys in 3.5 wt.% NaCl solution", *Corrosion Science*, Vol. 55, (2012), pp. 301–312.
- [72] Hiroshi Matsubara, Yasuhiro Ichige, Kazuaki Fujita, Hiroshi Nishiyama, Kazunori Hodouchi, "Effect of impurity Fe on corrosion behavior of AM50 and AM60 magnesium alloys", *Corrosion Science*, Vol. 66, (2013), pp. 203–210.
- [73] Weiwei Song, Holly J. Martin, Ayesha Hicks, Denver Seely, Christopher A. Walton, "Corrosion behaviour of extruded AM30 magnesium alloy under salt-spray and immersion environments", *Corrosion Science*, Vol. 78, (2014), pp. 353–368.
- [74] R. Matthew Asmussen, W. Jeffrey Binns, Pellumb Jakupi, and David Shoesmith, "The Influence of Microstructure on the Corrosion of Magnesium Alloy ZEK100", *NACE International, Corrosion*, Vol. 71, No. 2, (2015), pp. 242-254.
- [75] Tielei Zhang, Zesheng Ji, Shuyan Wu, "Effect of extrusion ratio on mechanical and corrosion properties of AZ31B alloys prepared by a solid recycling process", *Materials and Design*, Vol. 32, (2011), pp. 2742–2748.
- [76] Z. Pu, G.-L. Song, S. Yang, J.C. Outeiro, O.W. Dillon Jr., D.A. Puleo, I.S. Jawahir, "Grain refined and basal textured surface produced by burnishing for improved corrosion performance of AZ31B Mg alloy", *Corrosion Science*, Vol. 57, (2012), pp. 192–201.

- [77] Jinsun Liao, Makoto Hotta, Shin-ichi Motoda, Tadashi Shinohara, "Atmospheric corrosion of two field-exposed AZ31B magnesium alloys with different grain size", *Corrosion Science*, Vol. 71, (2013), pp. 53–61.
- [78] D. Thirumalaikumarasamy, K. Shanmugam, V. Balasubramanian, (2005), "Comparison of the corrosion behaviour of AZ31B magnesium alloy under immersion test and potentiodynamic polarization test in NaCl solution", *Journal of Magnesium and Alloys* 2, (2014), pp. 36-49.
- [79] Z.Y. Nan, S. Ishihara, T. Goshima, "Corrosion fatigue behavior of extruded magnesium alloy AZ31 in sodium chloride solution", *International Journal of Fatigue*, Vol. 30, (2008), pp. 1181–1188.
- [80] Ya. Unigovski, A. Eliezer, E. Abramov, Y. Snir, E.M. Gutman, "Corrosion fatigue of extruded magnesium alloys", *Materials and Engineering*, Vol. A360, (2003), pp. 132- 139.
- [81] A.N. Chamos, Sp.G. Pantelakis, V. Spiliadis, "Fatigue behaviour of bare and pre-corroded magnesium alloy AZ31", *Materials and Design*, Vol. 31, (2010), pp. 4130–4137.
- [82] Eric Irissou, Jean-Gabriel Legoux, Bernard Arsenault, and Christian Moreau, "Investigation of Al-Al₂O₃ Cold Spray Coating Formation and Properties", *ASM International, Journal of Thermal Spray Technology* Volume 16(5-6), (2007), pp. 661–668.
- [83] K.Spencer, D.M. Fabijanic, M.-X. Zhang, "The use of Al–Al₂O₃ cold spray coatings to improve the surface properties of magnesium alloys", *Elsevier, Surface & Coatings Technology*, Vol. 204, (2009), pp. 336–344.
- [84] Yongshan Tao, Tianying Xiong, Chao Sun, Huazi Jin, Hao Du, Tiefan Li, "Effect of a-Al₂O₃ on the properties of cold sprayed Al/a-Al₂O₃ composite coatings on AZ91D magnesium alloy", *Applied Surface Science*, Vol. 256, (2009), pp. 261–266.
- [85] Yongshan Tao, Tianying Xiong, Chao Sun, Lingyan Kong, Xinyu Cui, Tiefan Li, Guang-Ling Song, "Microstructure and corrosion performance of a cold sprayed aluminium coating on AZ91D magnesium alloy", *Corrosion Science*, Vol. 52, (2010), pp. 3191–3197.
- [86] Hengyong Bu, Mohammed Yandouzi, Chen Lu, Daniel MacDonald, Bertrand Jodoin, "Cold spray blended Al+Mg₁₇Al₁₂ coating for corrosion protection of AZ91D magnesium alloy", *Surface & Coatings Technology*, Vol 207, (2012), pp. 155–162.
- [87] Albinmoussa J., Jahed H., and Lambert S., "Cyclic Behaviour of Wrought Magnesium Alloy under Multiaxial Load". *International Journal of Fatigue*, Vol. 33 (8), (2011), pp. 1127-1139.
- [88] Microindentation, "Hardness Testing of Materials Using ASTM E384", *ASTM International*, West Conshohocken, PA, 2011, <http://www.astm.org/>

- [89] Instron Model R.R. Moore High Speed Rotating Beam Fatigue Testing Machine, Operating Instructions.
- [90] Supersonic Spray Technologies Practical Cold Spray Coatings, <http://www.cntrl.com/en/>
- [91] ASTM G1 – 03, Standard Practice for Preparing, Cleaning, and Evaluating Corrosion Test Specimens, ASTM International, West Conshohocken, PA, 2011, <http://www.astm.org/>
- [92] Md. Shahnewaz Bhuiyan, Yuichi Ostuka, Yoshiharu Mutoh, Tsutomu Murai, Shinpei Iwakami, "Corrosion fatigue behavior of conversion coated AZ61 magnesium alloy", *Materials Science and Engineering*, Vol. A 527, (2010), pp. 4978–4984.
- [93] Roxanna B. Alvarez, "Corrosion relationships as a function of time and surface roughness on a structural AE44 magnesium alloy", *Corrosion Science*, Vol. 52, (2010), pp. 1635–1648.
- [94] Holly J. Martin, "Comparison of corrosion pitting under immersion and salt-spray environments on an as-cast AE44 magnesium alloy", *Corrosion Science*, Vol. 52, (2010), pp. 3624–3638.
- [95] ASM Specialty Handbook: "Magnesium and Magnesium Alloys", Asm International, (1999).
- [96] Hassan Mahmoudi-Asl, "The Effect of Residual Stress Induced by Cold Spray Coating on Fatigue Life of Magnesium Alloy AZ31B", Master thesis, University of Waterloo, (2011).
- [97] R. Ghelichi, D. MacDonald, S. Bagherifard, H. Jahed, M. Guagliano, B. Jodoin, "Microstructure and fatigue behavior of cold spray coated Al5052", *Acta Materialia*, Vol. 60, (2012), pp. 6555–6561.